Université catholique de Louvain

Faculté des Sciences
Département de Physique
Institut d'Astronomie et de Géophysique
Georges Lemaître

Reconstruction of the 1979-2005 Greenland ice sheet surface mass balance using satellite data and the regional climate model MAR

Dissertation doctorale présentée en vue de
l'obtention du grade de docteur en sciences par

Xavier Fettweis

Jury :
Prof. J.-P. van Ypersele (UCL-ASTR, promoteur)
Prof. H. Gallée (LGGE, Grenoble, France, co-promoteur)
Dr. F. Lefebre (VITO, Mol, Belgique)
Prof. N. van Lipzig (KUL, Leuven, Belgique)
Prof. G. Schayes (UCL-ASTR)
Prof. T. Fichefet (UCL-ASTR)
Prof. A. Nauts (UCL-PAMO)
Prof. R. Prieels (UCL-FYNU, Président du Jury)

28 Août 2006

Remerciements

J'aimerais tout d'abord remercier mes promoteurs Jean-Pascal van Ypersele et Hubert Gallée sans qui je n'aurais jamais pu réaliser ce travail. Jean-Pascal van Ypersele a toujours trouvé du temps pour m'écouter, m'encourager, me conseiller et surtout me "coacher" avant une conférence internationale. Merci aussi pour la confiance et la liberté qu'il m'a accordées tout au long de cette thèse. Hubert Gallée est à la base du modèle MAR avec lequel j'ai travaillé. Outre son aide technique – très précieuse – liée à l'utilisation de son modèle, il m'a aidé, grâce à sa grande disponibilité, à mieux comprendre et à résoudre certaines sorties inattendues du modèle, à orienter ma recherche et à m'initier aux particularités du climat polaire. Son enthousiasme fut communicatif, son accueil au sein de son équipe de Grenoble, chaleureux et son hospitalité, spontanée.

Je voudrais aussi exprimer toute ma gratitude à Filip Lefebre qui est le véritable initiateur de ce travail. Ayant étudié le Groenland avec MAR avant moi, il a pris le temps de me transmettre son expérience. J'ai ainsi pu démarer sur des bases scientifiquement établies, en reprenant le flambeau là où il l'avait laissé. Par après, il a été plus que présent pour m'aider, me conseiller et participer de près à mes recherches comme coauteur de mes articles. Je lui suis profondément reconnaissant d'avoir accepté d'être membre de mon jury.

Je remercie également Guy Schayes, Nicole van Lipzig et René Prieels pour les commentaires judicieux et constructifs qu'ils ont apportés à la première version de ce texte. J'aimerais aussi citer Thierry Fichefet et André

Nauts, membres de mon jury, qui ont accepté de relire mon texte dans une optique linguistique.

Si j'ai pu mener ce travail à terme, c'est aussi grâce à l'ambiance, l'entraide et le dynamisme qui règne dans notre Institut. Merci à vous tous qui avez, de près ou de loin, contribué à l'achèvement de ce travail. Je pense particulièrement aux autres doctorants (Aurore, Emilie, Emmanuel, Emmanuelle, Martin, Rafiq, Sébastien, Valérie, Wouter) pour leurs coups de main, leur conseils et les nombreuses activités extra-thèse réalisées ensemble. Merci à Wouter Lefebvre pour son aide précieuse en statistique et pour nos échanges scientifiques concernant l'évolution de nos recherches respectives et la météorologie, ainsi que pour avoir relu ce texte avec attention.

Enfin merci à tous ceux qui, dans mon entourage proche, m'ont permis de mener à terme cette recherche par leur soutien et leurs encouragements.

Content

List of abbreviations

APP	AVHRR Polar Pathfinder
AS1997	Abdalati and Steffen (1997)
AS2001	Abdalati and Steffen (2001)
AVHRR	Advanced Very High Resolution Radiometer
AWS	Automatic Weather Station
Bro2001	Bromwich et al. (2001)
CASPR	Cloud and Surface Parameter Retrieval
CROCUS	Name of the snow model developed by Brun et al. (1992)
CRU	Climate Research Unit
DMI	Danish Meteorological Institute
ECMWF	European Centre for Medium-Range Weather Forecasts
ELA	Equilibrium Line Altitude
ERA-15	Reanalysis of the ECMWF (1979-1994)
ERA-40	Reanalysis of the ECMWF (1957-2002)
Fet2005	Fettweis et al. (2005)
Fet2006	Fettweis et al. (2006)
GC-Net	Greenland Climate Network
GCM	General Circulation Model
GHG	GreenHouse Gas
GIMEX	Greenland Ice Margin EXperiment
ImpXPGR	Improved Cross-Polarized Gradient Ratio
IPCC	Intergovernmental Panel on Climate Change
IMB	Ice sheet Mass Balance
ImpXPGR	Improved XPGR (Cross-Polarized Gradient Ratio)

IR	infra red
LHF	Latent Heat Flux
LWC	Liquid Water Content
LWD	Long Wave Downward flux
MAR	Modèle Atmosphérique Régional
MM5	The Fifth-Generation NCAR / Penn State Mesoscale Model
NAO	North Atlantic Oscillation
NCAR	National Center for Atmospheric Research (US)
NCEP	National Centers for Environmental Prediction (US)
NOAA	National Oceanic and Atmospheric Administration
NSIDC	National Snow Ice Data Center
PARCA	ProgrAm for Regional Climate Assessment
PDD	Positive Degree Day
THC	ThermoHaline Circulation
RCM	Regional Climate Model
RDM	Rain (and snow) Disaggregator Model
RH	Relative Humidity
RMSE	Root Mean Square Error
SBL	Surface Boundary Layer
SEB	Surface Energy Balance
SISVAT	Soil Ice Snow Vegetation Atmosphere Transfer
SHF	Sensible Heat Flux
SMB	Surface Mass Balance
SMMR	Scanning Multichannel Microwave Radiometer
SSM/I	Special Sensor Microwave/Imager
SST	Sea Surface Temperature
SVAT	Surface Vegetation Atmosphere Transfer
SWD	Short Wave Downward flux

SWDn	Net Short Wave Downward flux
su	Summer
Sv	Sverdrup = 10^6 m^3 s^{-1}
T19H	19-GHz horizontal polarized brightness temperature
T37V	37-GHz vertical polarized brightness temperature
VDEL	Name of the precipitation disaggregator model developed by Sinclair (1994)
we (WE)	Water Equivalent
wi	Winter
XPGR	Cross-Polarized Gradient Ratio
yr	Year

Chapter 1

Introduction

1.1 The Greenland ice sheet mass balance

1.1.1 Global warming

Greenland ice sheet mass balance[1] variations play an important role in global sea level and oceanic thermohaline circulation (THC[2]) changes. On the one hand, the Greenland ice sheet mass balance changes appear to have contributed several metres to some of the sea level fluctuations since the last interglacial period known as the Eemian, 125000 years ago (Cuffey and Marshall, 2000) and are expected to contribute to sea level rise under projected future global warming throughout this century (Church et al., 2001). Countries like Bangladesh, Belgium, The Netherlands, Egypt, United

1 The *Greenland mass balance* is defined as the difference between the total grounded mass at the beginning and the end of the mass balance year which is composed of a winter accumulation season and a summer ablation season, characterized by a gain and loss of mass, respectively. Accumulation can take place through snowfall, refreezing of rainfall and water deposition while the ice sheet loses mass by run-off of melted snow/ice at the surface, water evaporation and sublimation, iceberg calving, basal melting as well as the flux of drifting snow across the ice sheet margin. Ice shelves connected to the ice sheet are not included since their melting does not contribute to sea level change (Paterson, 1994).

2 The *THC*, also named the *ocean conveyor belt*, is a global-scale overturning in the ocean driven by density differences arising from temperature and salinity effects. In the Atlantic, heat is transported by warm surface waters flowing northward as far as the Nordic Sea and Labrador Sea. These surface saline waters are cooled in winter, become denser and sink to a great depth flowing southwards (see Rahmstorf (1995) for more details).

States (Louisiana, Florida), ... would be the first under the threat of a sea level rise. On the other hand, increases in the freshwater flux from the Greenland ice sheet (the run-off[3] of the surface melt water, the basal[4] melting and the glacier discharge[5]) could perturb the THC by reducing the density contrast driving the thermohaline circulation (Rahmstorf, 1995). During the last glaciation, palaeoclimatological studies show that abrupt climate changes originated through transitions of the THC between different modes in response to small changes in the hydrological cycle (Clark et al., 2002). Any weakening of the THC in response to a surface warming and an increasing freshwater flux induced by the global warming (Manabe and Stouffer, 1994; Rahmstorf and Ganopolski, 1999; Voss and Mikolajewicz, 2001; Gregory et al., 2005; Swingedouw et al., 2006) would reduce the heat input in the North Atlantic ocean and subsequently reduce the warming in regions like Europe. Indeed, the upper branch of the THC in the Atlantic (The North Atlantic Drift) transports a large amount of heat, which tempers presently the winter in the regions close to its path (Europe, ...).

There is almost no more doubt now that human activities are responsible for a large part of the global temperature rise observed since the beginning of the industrial era. This is due mainly to our increasing greenhouse gas (GHG) emissions (Houghton et al., 2001). In the future, according to the 2001 Intergovernmental Panel on Climate Change (IPCC) report (Houghton et al., 2001), the anthropogenic forcings (without mitigation) could warm up the Earth by 1.4 to 5.8°C over the period 1990 to 2100 depending on the

3 *Runoff* is water from rain, snow/ice melt that is not absorbed by the snow and that flows over the ice sheet surface into the ocean. It can travels downward through the ice, reaches the bottom and lubricates the ice/bedrock interface, facilitating glacier sliding (Zwally et al., 2002).

4 *Basal melting* occurs at the base of the ice sheet at the ice/bedrock interface due to the ground heat flux and at the base of the floating ice tongues at the ice/ocean interface due to the ocean heat flux.

5 *Glacier discharge* or *iceberg calving* is the formation of an iceberg as ice breaks off a glacier or ice shelf.

emission scenario and model used. The consequences of a climate warming on the Earth system would be multiple: a decrease of the seasonal snow cover and sea ice extent, a retreat of continental glaciers and a warming of the ocean inducing a sea level rise, a weakening of the THC, an intensification of the hydrological cycle, a possible modification of some modes of variability (like El Niño, the Indian monsoon, ...) that impact on regional droughts and floods, a probable increase in extreme events, ... (Houghton et al., 2001). This will affect ecosystems as well as human activities (agriculture, health, tourism, ...).

Contrary to the Antarctic ice sheet which is supposed to gain mass because of heavier precipitation during the 21th century (Houghton et al., 2001), the Greenland ice sheet is likely to lose mass since the increase in run-off is expected to exceed the precipitation increase (Houghton et al., 2001; Alley et al., 2005). Indeed, a temperature increase will induce a larger melt of the snow/ice in summer, but also a higher evaporation above the ocean which will send more moisture inland and therefore the precipitation will be stronger. Increasing precipitation suggests more snowfall in winter and a simultaneous competing increase in summer rains, which accelerates the snow/ice melting. With warmer temperatures, more of the precipitation at low elevations will be rain instead of snow and the wetting of the snow leads to reduced surface albedo, which can contribute to an earlier than normal onset of melt. The run-off of the melt water represents about half of the annual mass loss of the Greenland ice sheet (Zwally and Giovinetto, 2001). The remainder of the ablation results mainly from iceberg discharge and subglacial melting (Reeh et al., 1999). The surface water vapour fluxes are generally small in comparison with precipitation rates (Box and Steffen, 2001; Box et al., 2004). Recent observations (Rignot and Kanagaratnam, 2006) show an acceleration of the glacier discharge which also contributes to

the global sea level rise and to the freshwater flux increase into the North Atlantic. Zwally et al. (2002) suggest that this observed increase of the glacier velocity would be induced by the increasing surface melt. Indeed, the melt water reaching the glacier bed lubricates the ice/bedrock interface, facilitating glacier sliding. This will also thin the margin and cause the ice sheet retreat from the coast as pointed out by Krabill et al. (1999). Due to albedo[6] and elevation[7] feedbacks which are both positive, a progressive depletion of the Greenland ice sheet will amplify the deglaciation and change the local atmospheric circulation (Dethloff et al., 2004; Ridley et al., 2005). For year 3000, some models simulate even a complete disappearance of the Greenland ice sheet in a high CO_2 climate (Gregory et al., 2004; Ridley et al., 2005; Driesschaert, 2005). If the ice sheet would melt completely, the mean sea level would be higher by 7.4 m (Bamber et al., 2001). The removal of the Greenland ice sheet due to a prolonged climatic warming could be irreversible (Toniazzo et al., 2004). The resulting freshwater increase could severely weaken the THC (Ridley et al., 2005; Driesschaert, 2005) or even completely shut it down (Houghton et al., 2001; Fichefet et al., 2003; Rahmstorf et al., 2005).

Despite the importance of the Greenland ice sheet in global climate/change area, uncertainties in both the current mass balance of the ice sheet and its probable response to future climatic changes remain high (Van der Veen, 2002). Not everybody agrees whether the ice sheet is in balance or not in the current climate. The generally accepted negative sign of the Greenland ice sheet mass balance since the 1990's (Alley et al., 2005; Hanna et al., 2005;

6 If the climate warms up, the snow/ice cover decreases to the benefit of the tundra (with a lower albedo), more solar power is absorbed by the surface, the surface temperature increases which in turn warms up the climate.

7 If the climate warms up, the altitude of the ice sheet summit decreases, the summit temperature increases due to lower elevation which in turn increases the melt and the amount of liquid precipitation against solid precipitation (accumulation).

Box et al., 2006) has even been recently called in question by satellite laser altimetry observations (Johannessen et al., 2005).

1.1.2 The mass balance zones (definitions)

As mentioned above, the *Greenland Ice sheet Mass Balance* (IMB) is the difference between the total grounded ice/snow/water mass at the beginning and the end of the mass balance year .i.e. roughly the difference between the mass gained in surface by snow accumulation and that lost by ice ablation (at the surface and at the base of the ice sheet) and calving. The mass balance of the ensemble of processes that take place at the surface of the ice sheet (i.e. snowfall, surface melt, sublimation, snow erosion by the katabatic[8] winds, ...) determine the so-called *Surface Mass Balance* (SMB). The *equilibrium line* divided the ice sheet surface into the *ablation zone* (net mass loss over one mass balance year) and the *accumulation zone* (net mass gain). The Figure 1.1 illustrates these SMB areas by showing the 1991-2000 annual mean SMB modelled by the Polar MM5 model (Box et al., 2004). The SMB is governed by the interactions between the snow and ice surface with the atmosphere above. In this thesis, we will be exclusively focused on the SMB of the Greenland ice sheet because we do not have an ice sheet model.

One usually spots six surface mass balance zones of equal physical characteristics of the snow/ice (i.e. *facies*) at the surface of the Greenland ice sheet (Benson, 1962; Janssens and Huybrechts, 2000). See Figures 1.2.

The largest zone in accumulation area where melt never takes place is the *dry snow zone* bordered at its lowest elevations by the dry snow line. An almost equally large area is formed by the *percolation zone* between the dry snow line and the wet snow line. This facies is characterised by summer

8 A katabatic wind is a gravity wind caused by the downward motion of cold, dense air that blows down a topographic incline such as a hill, mountain, or glacier.

melt11 which refreezes immediately and no capillary water occurs because the firn[9] temperature does not reach the melting point. It contains therefore numerous ice layers and ice glands[10]. At elevation below the wet snow line, capillary water is upheld in the liquid phase. The run-off line delineates the *slush[11] zone*, where the firn is saturated and run-off can take place, from the *wet snow zone* where the snow is not entirely saturated at the end of the melt season. The lower separation of the slush zone is the snow line, which represents the lowest elevation where winter snow survives during the summer. Further down slope is the *superimposed ice[12] zone* where not all of the refrozen melt water remelts during the next summer. The slush zone and the superimposed ice zone are very narrow. In general, the run-off line is 100-200 m higher than the equilibrium line which separates the *ablation zone*, where the annual mass balance is negative, from the accumulation area (net mass grain over mass balance year). Blue melt ponds[13] can liberally dot the surface below the run-off zone as shown in Figure 2.6. These ponds serve as reservoirs of water that can speed up the ice's journey to the sea. Melt water travels downwards through the ice and once it reaches the bottom, it can loosen the bond between the ice and the underlying rock, accelerating the ice flow (Zwally et al., 2002).

The altitude where accumulation and ablation balance equals zero i.e. where the snowfall equals roughly the surface melt, called the *Equilibrium*

9 *Firn*, partially-compacted névé, is old snow that has become granular and compacted (dense) as the result of various surface metamorphoses, mainly melting and refreezing but also including sublimation. The resulting particles are generally spherical and rather uniform. Firnification, the process of firn formation, is the first step in the transformation of snow into land ice. Firn generally has a density higher than 550 kg/m³.

10 *Ice glands* is the technical name for the vertical channels in the percolation zone through which the water once drained, but which are frozen now.

11 *Slush* is partly melted snow and ice.

12 *Superimposed ice* is ice exposed at the surface of a glacier that was formed by the freezing of melted snow after deposition. It usually located below the snow line and above the equilibrium line. Although it is ice, it is part of the accumulation area.

13 Melt ponds are temporary melt water lakes above the ice.

Line Altitude (ELA), decreases with the latitude and increases in precipitation shadow regions (i.e. with low precipitation). It ranges from 1500 m in the south to 500 m along the north coast (Zwally and Giovinetto, 2001; Box et al., 2004). Interannual accumulation and ablation variability cause ELA fluctuations. Therefore, ELA provides an useful indicator of the combined influence of thermal and precipitation forcing on the surface mass balance. Figure 1.2 shows the ELA variability between 2001 and 2005.

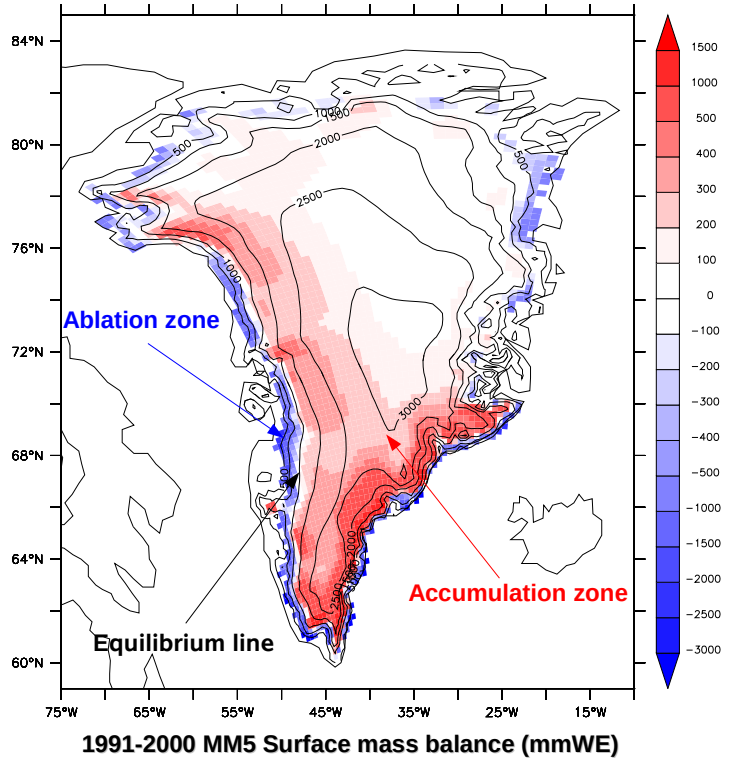

Figure 1.1 : The 1991-2001 annual mean SMB simulated by Polar MM5 (Box et al., 2004). The equilibrium line divides the Greenland ice sheet surface into the ablation zone (in blue) and the accumulation zone (in red). The Polar MM5 SMB is calibrated with in situ observations (snow pits, ablation stakes, ice cores) to remove systematic biases via statistical regression (Box et al., 2004 and 2006). The Polar MM5 data comes from [http://polarmet.mps.ohio-state.edu/jbox/data/.](http://polarmet.mps.ohio-state.edu/jbox/data/)

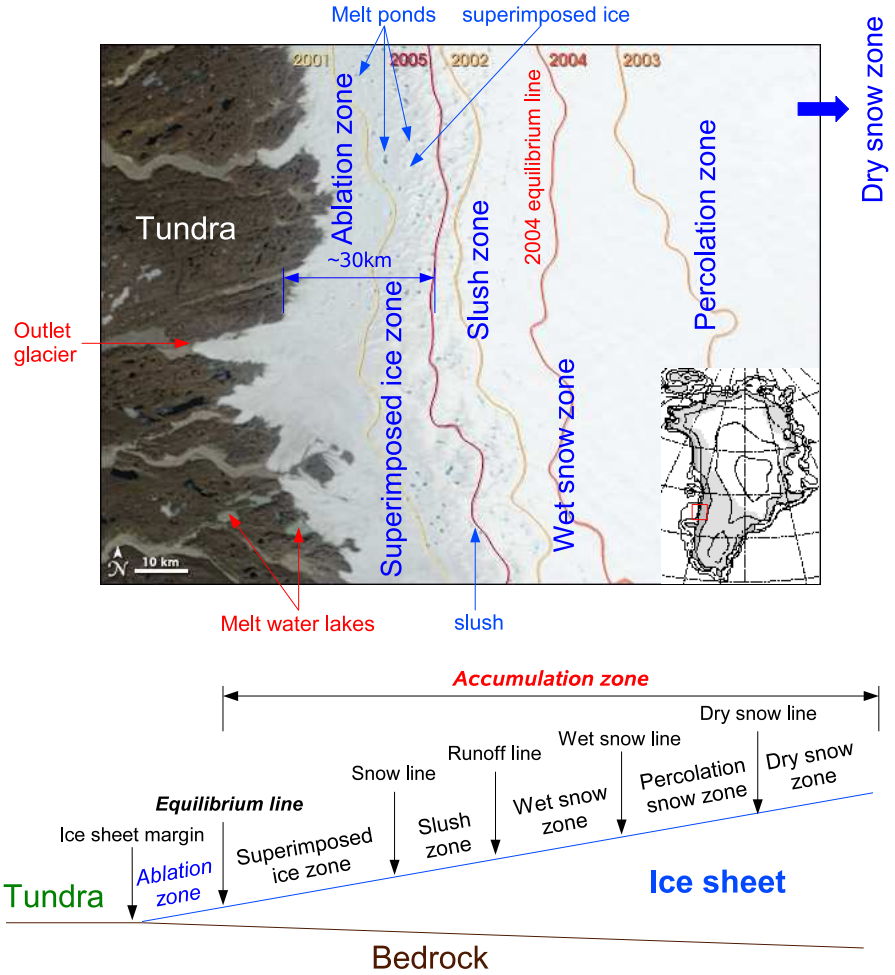

Figure 1.2 : Top: the south western Greenland ice sheet mass balance zones (the location is shown in red on the Greenland map attached to the photo) photographed by a MODIS (for Moderate Resolution Imaging Spectroradiometer) satellite of the National Aeronautic and Space Administration (NASA). The photo comes from http://earthobservatory.nasa.gov/ and shows the Greenland ice sheet midway through the seasonal melt. The ELAs for 2001-2005 years are plotted. Below: a conceptual 1D transversal section of the western ice sheet. The scales are not respected.

1.1.3 The measurements over the Greenland ice sheet

Since 1871, measurements along the Greenland coast have been made by the Danish Meteorological Institute (DMI). While these synoptic weather stations are not really representative for the Greenland ice sheet conditions, they are the longest known continuous series of climate records in Greenland. The temperature observations (Cappelen, 2004) exhibit sharp increases over the past two decades after having reached a maximum in the 1930s followed by a cooling that prevailed until the early 1980s (Box, 2002; Chylek et al., 2006). Warming since the mid-1980s has brought the once anomalously cold Greenland regional temperatures into synchronicity with the global warming pattern (Chylek et al., 2004; Chylek and Lohmann, 2005). The DMI measurements have been intensively used in evaluating the accuracy of models (e.g. Hanna and Valdes, 2001; Dethloff et al., 2002; Fettweis et al., 2005; Hanna et al., 2005) or in compiling Greenland accumulation maps (e.g. Ohmura et al., 1999; Bales et al., 2001).

Since 1995, about twenty Automatic Weather Stations (AWS) have collected hourly climatological and glaciological parameters at various locations on the Greenland ice sheet (Steffen and Box, 2001). This network, called Greenland Climate Network (GC-Net), of very needed inland stations has been installed with a distributed coverage over the ice sheet as part of the NASA ProgrAm for Regional Climate Assessment (PARCA), an initiative to understand the Greenland ice sheet mass balance (Thomas and PARCA Investigators, 2001). Precise station locations are given by Steffen and Box (2001). It provides an unique data set to assess errors over the ice sheet in models (Cassano et al., 2001; Box and Rinke, 2003; Box et al., 2004; Hanna et al., 2005) and to calibrate satellite data (Abdalati and Steffen, 1997; Stroeve et al., 2001). The GC-Net data set has also been notably used by Box

and Steffen (2001) to compile a map of the Greenland ice sheet surface net water vapour flux.

Some networks of stakes have been set up on the Greenland ice sheet along elevation profiles to measure directly the surface ablation/accumulation. Transects perpendicular to the ice sheet margin[14] have been chosen because surface ablation exhibits a strong variation with increasing altitude. Most of these measurements have been collected in the Jakobshavn region (shown on the satellite photo in Figure 1.1) near Kangerlussuaq along the K-Transect in west Greenland (Greuell et al., 2001). The measurements in this region have begun in 1990 during the Greenland Ice Margin EXperiment campaign (GIMEX, Oerlemans and Vugts, 1993). Snow pit density measurements at 10 cm intervals have also been made during GC-Net AWS maintenance visits since 1995 (Steffen and Box, 2001). Unfortunately, these measurements are limited in space and in time although they are one of the most reliable sources to evaluate and correct modelled surface mass balances (e.g. Zuo and Oerlemans, 1996; Gallée and Duynkerke, 1997; Lefebre et al., 2003; Box et al., 2006).

Snow-firn-ice core records are used to study the large climate variations in the past (GRIP members, 1993) or to estimate the present accumulation (Ohmura et al., 1999; Dethloff et al., 2003). Shallow snow-ice cores do not measure exactly the precipitated snow in the dry snow zone because evaporation makes accumulation slightly smaller than precipitation (Box and Steffen, 2001). As part of the PARCA research program, Bales et al. (2001) compiled a detailed accumulation map of the Greenland ice sheet using historical records, recent shallow ice core measurements from PARCA and precipitation measurements from stations around Greenland. However, these estimates are highly uncertain because i) they are produced on the basis of

14 i.e. the boundary line between the tundra and the ice sheet where the melt is maximum.

temporally non-uniform sets of observations, ii) there are few data below the dry snow zone on the ice sheet, iii) there are few coastal data that are representative of ice sheet versus ocean precipitation and iv) there is undersampling at all elevations in some parts of the ice sheet (Bales et al., 2001).

Since the late seventies, remote sensing of the polar regions provides researchers with a continuous temporal and spatial data set to investigate the physical characteristics of the poorly accessible ice sheet surface. Recent observational satellite-derived studies exhibit :

- an overall albedo decrease (Stroeve et al., 2001; Box et al., 2006),
- an increase of the melt area and the duration of the melt period (Abdelati and Steffen, 2001; Steffen et al., 2004; Steffen, 2005; Fettweis et al., 2006),
- a dramatic peripheral thinning rate of the Greenland ice sheet (Krabil et al.; 1999, 2000, 2004; Zwally et al., 2005) at low elevations,
- a thinning, retreat and acceleration of the outlet glaciers due to melt increase and the induced Zwally et al. (2002) effect[15] (Rignot et al., 2004; Luckman and Murray, 2005; Howat et al., 2005; Luckman et al., 2006; Joughin, 2006; Rignot and Kanagaratnam, 2006),
- a thickening at higher elevations due to heavier snowfall (Krabil et al., 2000; Thomas et al., 2001; Johannessen et al., 2005; Zwally et al., 2005) as announced by the IPCC.

Except Johannessen et al. (2005) estimates, satellite laser altimetry and airborne laser surveys based studies suggest rather an overall negative balance (Rignot and Thomas, 2002; Krabil et al., 2004; Velicogna and Wahr, 2005). Nevertheless, these estimates of the mass balance are all computed on

15 i.e. the acceleration of the glacier outlets due to the increasing melt water which by reaching the glacier bed, lubricates the ice/bedrock interface and facilitates the glacier sliding.

very small periods beginning at best at the earliest in 1990s. They are not always representative for long-term values given the important year to year variations observed in the annual mass balance (Greuell et al., 2001).

As mentioned above, large uncertainties remain in observation-based studies that estimate the mass balance and detect significant changes over the Greenland ice sheet, due to the sparse resolution of measurements in time and space. Numerical models offer a further possibility to determine efficiently the mass balance for past, present and future climatic conditions as well as to help interpreting and calibrating satellite-derived measurements.

1.1.4 The modelling of the Greenland ice sheet

1.1.4.1 Mass balance positive degree-day models

The popular positive degree-day (PDD) models are a first approach to simulate the Greenland surface mass balance. They parametrize the surface melt as a function of the surface air temperature. This approach is entirely based on the observed robust correlation between melt rates and the sum of positive[16] air temperatures (Ohmura, 2001). Given their simplicity, this kind of models need low computational power and long-term simulations can been performed at very fine resolution. They are often coupled with thermodynamic ice sheet model to assess the past, present and future evolution of the Greenland ice sheet volume and its contribution to sea level rise (Ritz et al., 1997; Greve, 2000; Huybrechts et al., 2002; Huybrechts et al., 2004; Ridley et al., 2005).

16 i.e. above zero degree Celsius.

The melt *M (*mm WE[17] day^{-1}) is calculated as being

$$M = \beta\, PDD$$

where *PDD* equals the sum of the positive, mean daily temperatures over the time period for which one wants to calculate the amount of melt. β is the proportionality factor in mm WE $°C^{-1}$ day^{-1} (called PDD factor). The PDD factor is empirically derived from observations and applied elsewhere but unfortunately varies considerably with the air temperature, the cloudiness, the albedo, the kind of snow/ice (Braithwaite, 1995; Braithwaite and Yu, 2000; Lefebre et al., 2002). The generally accepted values ranges from 0.01 mm WE $°C^{-1}$ day^{-1} to 30 WE $°C^{-1}$ mm day^{-1}. So the choice of different PDD factor values for snow and ice is the great weakness of PDD models (Ohmura, 2001).

A SMB model based on the PDD approach has the advantage over a more complex energy balance model of requiring relatively few and simpler input data: temperature and precipitation. The precipitation fraction that falls as rain is determined by the surface air temperature and the rest contributes to the accumulation. The PDD model inputs come from climatologies (Janssens and Huybrechts, 2000), from reanalyses[18] (Hanna et al., 2005), from General Circulation Model (GCMs) fields (Huybrechts et al., 2004; Ridley et al., 2005; Zweck and Huybrechts, 2005) or from satellite-derived observations (Mote et al., 2003) and are often resampled/downscaled to a finer grid.

Given i) its simplicity, ii) the fact that temperature data are more easily available than obtaining energy balance fluxes and iii) its friendly computer time use, the PDD method is still largely used by the research community (Hanna et al., 2005). Nonetheless, it does not account for the influence of

17 Millimetres of water equivalent per day. See also the abbreviation section at the beginning of this book.

18 Reanalysis is model compilations and assimilations of available satellite, station and weather balloon observations.

wind speed, albedo and cloud cover and excludes the modelling of the interactions between the ice sheet surface and the atmosphere (Ohmura, 2001). In addition, the model results are found to be very sensitive to some model parameters such as the standard temperature deviation and the snow and ice positive degree-day factors. Finally, the parametrizations used (e.g. PDD factor value) are based upon present-day climatic conditions which compromises their use in modelling for different past and future climates. As concluded by Greve (2000), a more sophisticated approach should be used for a more accurate modelling of the processes that determine surface melting. Therefore energy-balance models have been developed.

1.1.4.2 Mass balance energy balance-based models

As already mentioned above, a second, more complex, alternative is to simulate the SMB by means of an energy balance model in which melt water production is calculated from the residual of the surface energy budget. When the melting point has been reached during a period of energy surplus, the excess energy goes into conversion of solid ice/snow into liquid water. The model is based on physical laws (conservation of energy and mass), which guarantees its applicability in different climatic conditions. Both radiative (solar and infra-red) and turbulent (sensible and latent) heat fluxes are needed to force this kind of models and the surface can interact with the atmosphere via changes in albedo, roughness length, water vapour fluxes[19], ... The refreezing of melt water, the heat supply from rain as well as the firn/ice conductive heat flux are taken into account in most of the models to compute the surface energy budget. Although the first developed ones were driven by empirical energy fluxes parametrisations (van de Wel and

19 The water vapour fluxes include the condensation, the deposition, the evaporation and the sublimation.

Oerlemans, 1994), energy balance models are nowadays generally coupled to atmospheric models to allow interactions with the atmosphere.

GCMs coupled with (simplified) energy balance models have been used in experiments to simulate Greenland ice sheet mass balance under current and future climate conditions (Church et al., 2001; van de Wald et al., 2001; Murphy et al., 2002; Bugnion et Stone, 2002; Wild et al., 2003). Global models are suited for climate change experiments since shifts in the large-scale circulation and associated precipitation are accounted for.

However, major limitations of GCMs are their coarse horizontal resolution (currently 100-250km) and their simplified physics for surface processes. At this spatial scale, the steep ice sheet margin and the ablation zone are not adequately resolved. The latter, where substantial seasonal melting occurs, is not wider than 100 km in Greenland. Furthermore, a terrain smoothing along the steep ice margins can produce net elevation changes of the margin ice sheet grid points and therefore induces systematic over/underestimation of the ablation rate (Hanna and Vades, 2001). Increasing resolution is also found to improve the simulation of precipitation (Christensen et al. (1998), Bromwich et al. (2001), Murphy et al. (2002)). Snow and ice melt modelling requires elaborated physics (Xue et al. (2003)). Cassano et al. (2001) mention that the use of a fixed albedo leads to large errors in the simulated net radiation budget over melting ice surfaces. Neglecting to take into account the night-time refreezing of retained meltwater overestimates melt (Pfeffer et al., 1991; Gallée and Duynkerke, 1997). Katabatic winds play an important role in the surface energy balance and consequently require to be modelled in details (Duynkerke and van den Broeke, 1994; van den Broeke et al., 1994). A high resolution limited-area Regional Climate Model (RCM) nested in a GCM or observation-based reanalysis (Giorgi and Mearns, 1999), answers some of these issues, i.e. higher spatial resolution (improved

orography), more sophisticated atmospheric physics and surface parametrizations designed for polar regions. All RCMs are coupled with an energy balance-based model. Satellite-derived albedos are sometimes even used to improve the accuracy of the modelled absorbed solar irradiance in surface energy budget calculations (Box et al., 2004). RCMs are nevertheless computationally expensive.

RCMs, operating on horizontal scales of tens of kilometres, offer an attractive alternative to GCMs, to statistical climatologies and to complete automatic weather station networks. RCMs nested in reanalysis can be thought of as being physically-based interpolators of the assimilated observations (from surface weather stations, atmospheric sounding and satellite remote sensing). They provide information for regions that do not benefit from direct observations and for explicit time periods, as opposed to temporally non-uniform climatologies. RCMs driven by a GCM are rather useful to refine and correct GCM predictions in future greenhouse warming scenarios (Kiilsholm et al., 2003). Greenland is ideally suited for atmospheric circulation modelling, with prevailing large-scale flow across the domain, unlike Antarctica, where the flow is quasi-concentric and where less benefit comes from lateral constraints imposed by the atmospheric analyses. That is why the Greenland ice sheet SMB is more and more studied with RCMs (Cassano et al., 2001; Dethloff et al., 2002; Hanna et al., 2002; Box and Rink, 2003; Mote, 2003; Fettweis et al., 2005; Box et al., 2006; Fettweis et al., 2006).

1.2 Motivation and structure of this thesis

In order to improve predictions of future behaviour of the Greenland ice sheet in the global warming context, it is necessary to better know and assess its current state and variability. That is the reason why we have chosen in this thesis to simulate the Greenland ice surface mass balance of the last thirty years with a coupled atmosphere-snow RCM having an horizontal resolution of 25 km. The motivation to use a RCM for this work is discussed above. The simulation starts in 1979 together with the beginning of remote sensing observations and lasts till the end of 2005. RCM applications to the observed past rather than the future benefit from the observations to drive the model (via the reanalysis) and to evaluate the model results. Furthermore, warming since the mid-1980s has brought the once anomalously cold Greenland regional temperatures into synchronicity with the global warming pattern. Therefore, put in context, our results should somewhat represent the Greenland ice sheet response to rapid warming. In addition, this 27-year simulation starting with the beginning of satellite observations, is the longest simulation of the Greenland climate made with a coupled snow atmospheric regional climate model until now (Box et al., 2006; Fettweis et al., 2006).

Benefiting from the UCL-ASTR's expertise (Gallée and Schayes, 1994; De Ridder and Gallée (1998); Brasseur et al., 2001; Lefebre et al., 2002; Marbaix et al., 2003), the RCM chosen here is the regional model MAR (Modèle Atmosphérique Régional) developed by Hubert Gallée. This thesis is in the continuity of works of Filip Lefebre (2001, 2002, 2003, 2005) and Hubert Gallée (1995, 1997, 2001, 2005) in which MAR is used to study the Greenland and Antarctic ice sheets. The model was originally developed for process studies in the polar regions, but it has been adapted since in order to

simulate long time periods in Europe (Marbaix et al., 2003). It has been coupled with a sophisticated physically-based (sub-)surface soil-snow-ice-vegetation model (Gallée et al. (2001); Lefebre et al. (2003)). The MAR model is described in more details in Chapter 2 as well as the simulation setup.

The MAR model was adapted by Lefebre (2002) in order to make it more appropriate for the modelling and study of the Greenland surface mass balance. The improved snow model was validated at ETH-Camp (Lefebre et al., 2003) and a 3D version of the coupled snow-atmosphere model was successfully compared with in-situ observations over South Greenland during the 1991 ablation season (Lefebre et al., 2005). This study notably highlighted a significantly better treatment of the near surface state variables in MAR than in the relatively coarse European Centre for Medium-Range Weather Forecasts (ECMWF) 15-year reanalysis (ERA-15). Since the Lefebre et al. (2003, 2005) validations, we decreased the spatial resolution from 20km to 25km to encompass the whole Greenland in the integration domain, we ran MAR on several years to reduce the sensitivity to the initialization of the snow pack, we changed the lateral boundary conditions by forcing MAR with the ERA-40 instead of the ERA-15, and we adapted/improved the snow model incorporated by Hubert Gallée in the one-dimensional (1D) Surface Vegetation Atmosphere Transfer (SVAT) scheme to be able to use this scheme over the Greenland ice sheet instead of the force-restore model from Deardoff (1978). We also made many improvements in the computation of initial/lateral boundary conditions from the ERA-40. I am currently the main maintainer and lead developer of this code (called NESTOR) for the MAR team. In addition, a new radiative scheme was inserted by Hubert Gallée, the advection scheme was improved, the water conservation in MAR hydrological scheme was corrected and

various improvements were made by continuous model refinements. Therefore, a new brief evaluation of this improved MAR version with in-situ data is needed to validate our results. It is the aim of Chapter 3 in which temperature, humidity, wind, surface pressure, snow height and surface radiations simulated by MAR are compared with 13 GC-Net AWSs in 1998, one of the warmest years since the beginning of the industrial era.

Precipitation is the main provision of mass in the SMB equation by adding snow or liquid water to the ice sheet. Winter accumulation of snow also conditions the appearance of low albedo zones in summer, which has an impact on the melt intensity. Indeed, low snow pack depth at the end of the winter leads to more rapid losses of winter snow mass and to higher degree day factors for bare ice (with a lower albedo) in the ablation zone. Mote (2003) further concludes that low ablation years are more likely associated with high winter accumulation. Therefore, it is necessary to model precipitation as accurately as possible to be able to assess the SMB. The MAR precipitation in 1990 is evaluated in Chapter 4 with coastal weather station observations, climatologies, results from other models as well as with reanalysis. The accuracy of precipitation derived from climatologies over the Greenland ice sheet is also discussed and finally, 8km-disaggregated MAR fields are presented. Following Funk and Michaelsen (2004), we improved the Rain Disaggregator Model (RDM), originally developed by Olivier Brasseur (Brasseur et al., 2001). Part of this chapter is published in Fettweis et al. (2005).

As the surface albedo depends on the nature of the snow, its grain size, its water content and its thickness, it is an excellent indicator of the snow pack properties. In addition, it is one of the most critical parameters of the surface energy equation since part of the energy needed for melting is supplied by solar radiation. So far, only the surface albedo from some weather stations

on the ice sheet has been used to validate a model (Bugnion and Stone, 2002, Lefebre et al., 2005)). In Chapter 5, we compare the modelled surface albedo with the surface albedo derived from the AVHRR Polar Pathfinder (APP) data set (Fowler et al., 2000). This is based on the Advanced Very High Resolution Radiometer (AVHRR) flown on the National Oceanic and Atmospheric Administration (NOAA) operational meteorological satellites. Part of this chapter is also published in Fettweis et al. (2005).

The melt extent can also easily be retrieved from satellite microwave brightness temperature and is an excellent indicator to evaluate the SMB simulated by MAR (Chapter 6). Nevertheless, measurements from ETH-Camp and JAR-1 AWS (West Greenland) and comparisons with MAR fields have highlighted flaws in the cross-polarized gradient ratio (XPGR) technique used to identify melt from passive microwave satellite data. It was found that dense clouds (causing notably rainfall) on the ice sheet severely perturb the XPGR melt signal. We have adapted the original XPGR melt detection algorithm to better incorporate atmospheric variability over the ice sheet and an updated (significant) melt trend for the 1979-2004 period has been calculated. Finally, a robust correlation is found between the total ice sheet run-off and the melt extent area detected by satellites. Part of this chapter is published in Fettweis et al. (2005, 2006).

Once the precipitation, albedo and melt extent have been validated, Chapter 7 analyses in details the results of a 27-year simulation (1979-2005) with a particular attention to the SMB interannual fluctuations. The model shows significant changes in the variability of the Greenland ice sheet mass balance components since 1979. The atmospheric part of the MAR model helps us to better understand these changes. Links with the North Atlantic

Oscillation[20] (NAO) are also explored. The recent global warming due to greenhouse gas concentration increases lies very likely at the root of these changes. These results are important to understand the effect of the Greenland ice sheet melting on the stability of the THC and on the mean sea level rise.

20 The North Atlantic Oscillation is a complex climatic phenomenon in the North Atlantic Ocean associated with fluctuations of climate between Iceland and the Azores (Source: http://www.wikipedia.org). It will be detailed in Section 7.4.

Chapter 2

The regional climate model MAR

This chapter is dedicated to the description of the coupled atmosphere-snow regional climate model MAR and the simulations setup. Special attention is given to the snow-ice model.

2.1 Model overview

The model used here is the regional climate model MAR (Modèle Atmosphérique Régional) coupled to the 1D Surface Vegetation Atmosphere Transfer scheme SISVAT (Soil Ice Snow Vegetation Atmosphere Transfer). The atmospheric part of MAR is fully described in Gallée and Schayes (1994) and Gallée (1995), while the surface SISVAT scheme is detailed in De Ridder and Gallée (1998) and Gallée et al. (2001).

This model was originally developed for process studies in polar regions (Greenland and Antarctica), but it has been adapted since in order to simulate long time periods (Marbaix et al., 2003). It has been recently applied to study of the monsoon in West Africa (Gallée et al., 2004; Messager et al., 2004), to estimate wind gust, to simulate high resolution precipitation in Europe (Brasseur, 2001; Brasseur et al., 2001) and in South America, to forecast weather in the Ross Sea, ...

2.1.1 Description of MAR

MAR is a hydrostatic primitive equation model in which the vertical coordinate is the normalized pressure

$$\sigma = (p-p_t)/(p_s-p_t)$$

where p, p_t and p_s are the pressure, the constant model top pressure and the surface pressure, respectively.

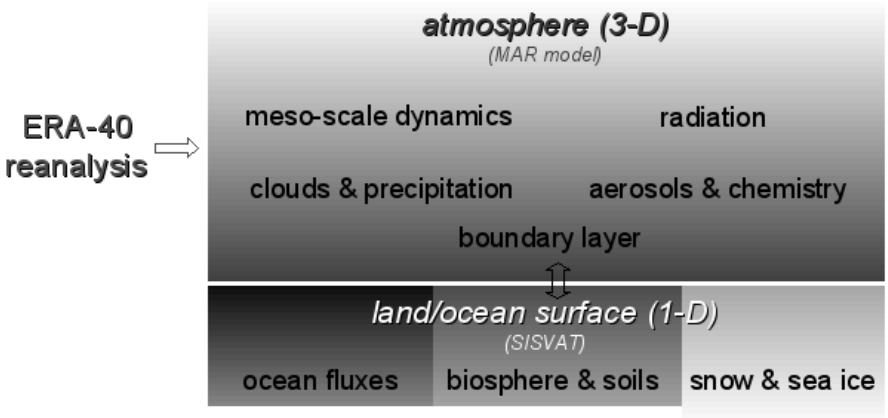

Figure 2.1 : General description of MAR (Source: Emilie Vanvyve).

The radiative scheme is the one used in the ERA-40 reanalysis. The solar radiation scheme is the one of Fouquart and Bonnel (1980). The original MAR long-wave radiation scheme followed a wide-band formulation of the radiative transfer equation according to Morcrette (1984). But recently, this scheme has been improved following Morcrette (2002) by including the Mlawer et al. (1997) parametrisations to correct an underestimation of the downward infra-red radiation at the surface, also detected in previous MAR versions (Lefebre et al., 2005). The representation of the hydrological cycle includes a cloud microphysical model, with conservation equations for cloud droplet, raindrop, cloud ice crystal, and snow flake concentrations (Gallee, 1995). It is based on Kessler (1969) and Lin et al. (1983) parametrizations.

The boundaries are treated according to a dynamic relaxation that includes a Newtonian term and a diffusion term (Davies, 1983; Marbaix et al., 2003). The parameterization scheme for the surface layer is based on Businger (1973) and Duynkerke (1991) formulations. In view of the complex structure of the katabatic layer, the E-ϵ order turbulence closure scheme from Duynkerke (1988) is used. Finally, the convective parametrization is the one of Bechtold et al. (2001) from the regional model MESO-NH (Météo France).

2.1.2 Description of SISVAT

SISVAT is a vertical 1-D model. The surface scheme includes soil-vegetation (De Ridder and Schayes, 1997), snow (Gallee et al., 2001), and an ice module (Lefebre et al., 2003).

The soil-vegetation module of SISVAT has been used over tundra and simulates the heat and moisture exchanges over land in the case of a snow-free surface. The snow-ice module of SISVAT is used in the case of snow deposition on the tundra, the sea ice, or the ice sheet. Sea Surface Temperatures (SST) and sea-ice distribution are based on the ECMWF analysis by linearly interpolating these fields on the regular MAR grid. The ECMWF analysis sea-ice coverage is derived from the satellite passive microwave data (SMMR and SSM/I data set).

The SISVAT snow-ice model is an one-dimensional multi-layered energy balance model that determines the exchanges between the sea ice, the ice sheet surface, the snow-covered tundra, and the atmosphere. It consists of a thermodynamic module, a water balance module, a turbulence module, a snow metamorphism module, a snow/ice discretization module, a blowing snow module, and an integrated surface albedo module. It is based on the CEN (Centre d'Etudes de la Neige) snow model called CROCUS (Brun et

al., 1992) and its physics and validation are described in details in Gallée and Duynkerke (1997), Gallée et al. (2001), and Lefebre et al. (2003).

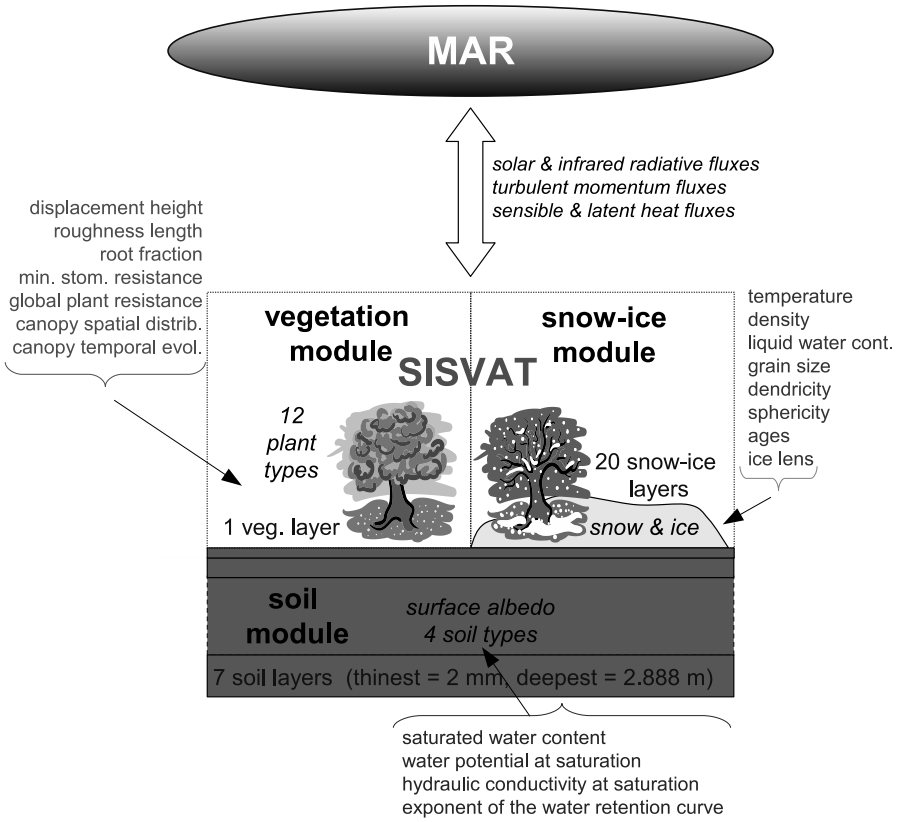

Figure 2.2 : General description of SISVAT (Source: Emilie Vanvyve).

The thermodynamic module computes the soil/snow energy balance. The energy equation takes into account :

- the absorbed short-wave flux,
- the downward and upward long-wave fluxes,
- the sensible and latent heat fluxes at the surface,
- the heat fluxes due to the snow/ice melt and sublimation,
- the heat fluxes due to the meltwater evaporation and refreezing,

- the heat flux due to rainfall, snowfall, condensation and deposition,
- the ground (soil) heat flux.

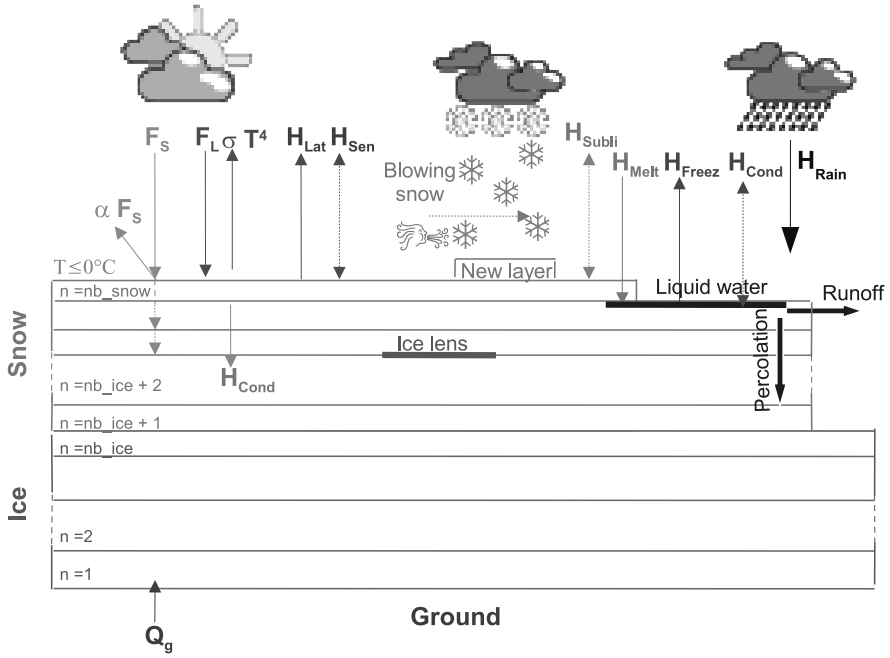

Figure 2.3 : Description of the SISVAT snow-ice model. The heat fluxes taken into account are the incoming solar radiation (F_s), the reflected solar radiation (αF_s where α is the albedo), the incoming infra-red radiation (F_l), the reemitted infra-red radiation following the Stefan-Bolzman law (σT^4), the latent (H_L) and sensible (H_S) heat fluxes, the heat fluxes from the sublimation/deposition (H_{subli}), from the melt (H_{melt}), from the refreezing (H_{freez}), from the evaporation/condensation (H_{cond}) and from the rainfall (H_{rain}), the ground heat flux (Q_g) and, finally, the heat conduction through the snow pack (H_{cond}). The geothermal heat flux is not taken into account. The liquid water can run-off, percolate or refreeze. Ice lenses can form. Snowfall forms new snow layers. Finally, the surface layer can be eroded by the wind.

The mass conservation equation in the presence of melting, meltwater flow and refreezing for a snow layer is resolved in the water balance module. The run-off of excessive internal and accumulated surface meltwater is based on the work of Zuo and Orlemans (1996). The run-off rate is a function of the

grid point slope (S) and three constants (c_1 = 0.33 day, c_2 = 25 days, c_3 = 140 days):

$$\frac{dW_r}{dt} = \frac{-W_r}{c_1 + c_2 * \exp(-c_3 * S)}$$

where W_r is the internal liquid water content in excess of the maximum water saturation. The choice of values of the constants c_1, c_2 and c_3 was discussed in Lefebre et al. (2003). The slope S takes into account the spatial variability. Therefore, in case of a flat surface, meltwater can accumulate which allows the albedo to reach very low values in summer. For example in the ablation zone, if all snow has melted away in the ablation zone, the meltwater accumulated upon the ice lowers the surface albedo to 0.3, while the ice albedo is fixed to 0.55 (Van de Wal and Oerlemans, 1994).

The SISVAT blowing snow module is currently in development by Hubert Gallée and has only been tested/validated on the Antarctic ice sheet and will not be used here. Nonetheless, it would be very interesting to test it on the Greenland ice sheet although Polar MM5 results (Box et al., 2004 and 2006) show a weak contribution of the blowing-snow sublimation to the Greenland ice sheet mass balance.

The snow metamorphism parametrizations are taken from the CROCUS model. The snow pack is described by its (gradient of) temperature, its liquid water content, its density, its age as well as the size and the form of the snow grains. Freshly fallen snow (called dendritic snow) is described by its dendricity and sphericity. Dendricity describes the part of the original crystal shapes which are still remaining in a snow layer and always decreases from 1 for fresh dendritic-shaped crystals to 0. Sphericity describes the ratio of rounded versus angular shapes. The dendritic snow grains evolve rapidly through disintegration and combined sublimation-deposition processes which also tend to dissipate the smaller particles in favour of bigger ones.

When dendricity becomes equal to 0, the snow grains arrive at the stage of rounded (sphericity = 1) crystals, faceted (sphericity = 0) crystals or at an intermediate state, depending on the temperature gradients that were present in the snow pack. The snow grains are now called non-dendritic snow grains and are characterized by their sphericity and their descriptive grain size. Sphericity again describes the ratio of rounded versus angular shapes while, the descriptive grain size indicates the average size of the snow crystals (Lefebre, 2002).

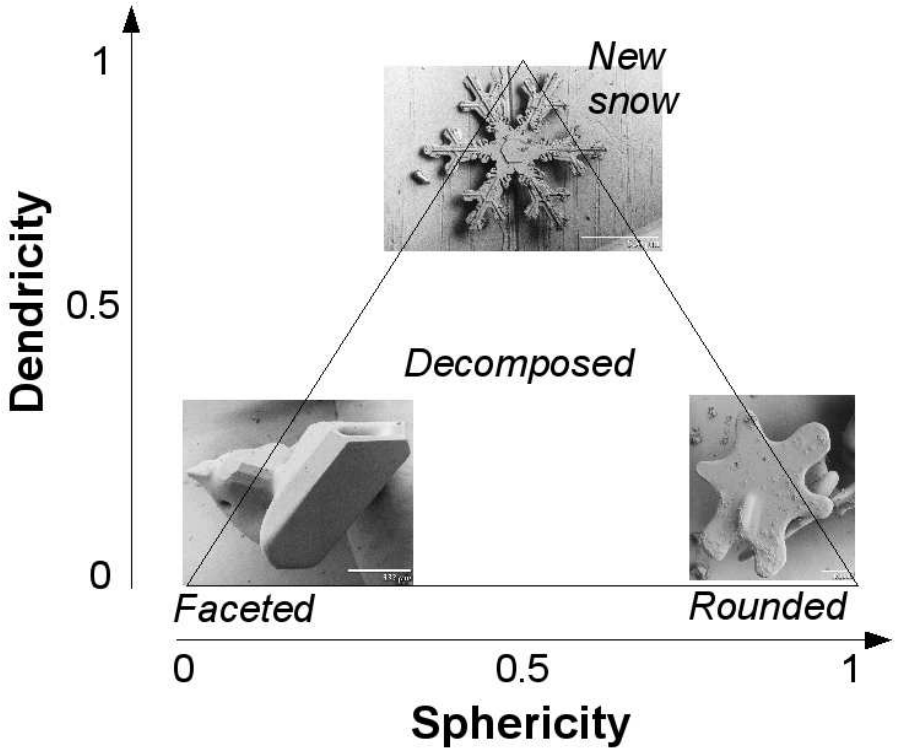

Figure 2.4 : Snow classification[21].

The snow/ice discretization module manages the snow pack vertical discretization. The total number of snow layers may change during the

21 The source of photos is http://emu.arsusda.gov/snowsite/

simulation. The snow grid has a maximum of 20 snow layers which have a variable thickness and the splitting or aggregation of snow layers is controlled by the CROCUS snow metamorphism laws. This is done in such a way that the natural stratigraphy of the snow pack is preserved.

A fresh snow layer is added to the snow pack when enough snow is available and the CROCUS parametrizations are used to determine the density, dendricity and sphericity of the fresh snow layer.

The surface albedo depends on :

- the simulated snow grain form and size (Brun et al., 1992):

$$\alpha = 0.606 \times \underbrace{(1 - 1.58\sqrt{d})}_{0.3-0.8\,\mu m} + 0.301 \times \underbrace{(1 - 15.4\sqrt{d})}_{0.8-1.5\,\mu m} + 0.093 \times \underbrace{(346.3\,d - 32.31\sqrt{d} + 0.88)}_{1.5-2.8\,\mu m}$$

  where α is the albedo of the snow pack and d is the optical grain size expressed in metre. The optical grain size is a function of the dendricity and sphericity of the snow pack (see Lefebre et al. (2003) for more details). Prescribed solar light fractions (0.606, 0.301, 0.093) are used for the spectral intervals of 0.3-0.8μm, 0.8-1.5μm and 1.5-2.8μm, respectively.
- the snow depth. If snow depth becomes less than 10 cm in melting conditions, a linear function is used to make a smooth transition between the snow and ice albedo ($\alpha = 0.55$) or tundra albedo ($\alpha = 0.15$);
- the cloudiness (Greuell and Konzelmann, 1994):

$$\alpha = \alpha + 0.05 \times (CC - 0.5)$$

  where CC is the cloudiness varying between 0 and 1;
- the accumulated surface water height. In case the snow depth is zero, surface ice sheet albedo varies exponentially between the ice (α = 0.55) and water (α = 0.15) albedo as a function of the accumulated surface

height. The melt water lakes (called melt ponds) upon the ice can lower the albedo until 0.30;

- the solar zenith angle (Segal et al., 1991):

$$\alpha = \alpha + max\left\{0\,;0.32\times\frac{1}{2}\left[\frac{3}{1+4\,max\{\cos(80°),\cos(\theta_0)\}}-1\right]\right\}$$

where θ_0 is the solar zenith angle.

We implemented these parametrized surface albedo into the snow/ice SISVAT module and validated it with satellite-derived observations in Chapter 5.

2.2 Model and simulation setup

2.2.1 Simulated domain

First of all, we will describe briefly the largest island of the word. Greenland is about 2.17 10^6 km^2 in which 1.76 10^6 km^2 is ice-covered (~81%). The highest mountain (the Gunnbjorn) culminates at 3700 m in the coastal south eastern mountainous chain. The ice sheet has the form of a dome with a maximum elevation at 3250m (the summit). If the ice sheet would melt, mean sea level would be by 7.4 m higher (Bamber et al., 2001). The population accounts for 56375 habitants (July 2005 estimate). Vikings reached the island in the 10th century from Iceland; Danish colonization began in the 18th century and Greenland was made an integral part of Denmark in 1953. Greenland was granted self-government in 1979 by the Danish parliament. The economy remains critically dependent on exports of fish and substantial support from the Danish Government[22].

22 Source: http://www.cia.gov/cia/publications/factbook/geos/gl.html

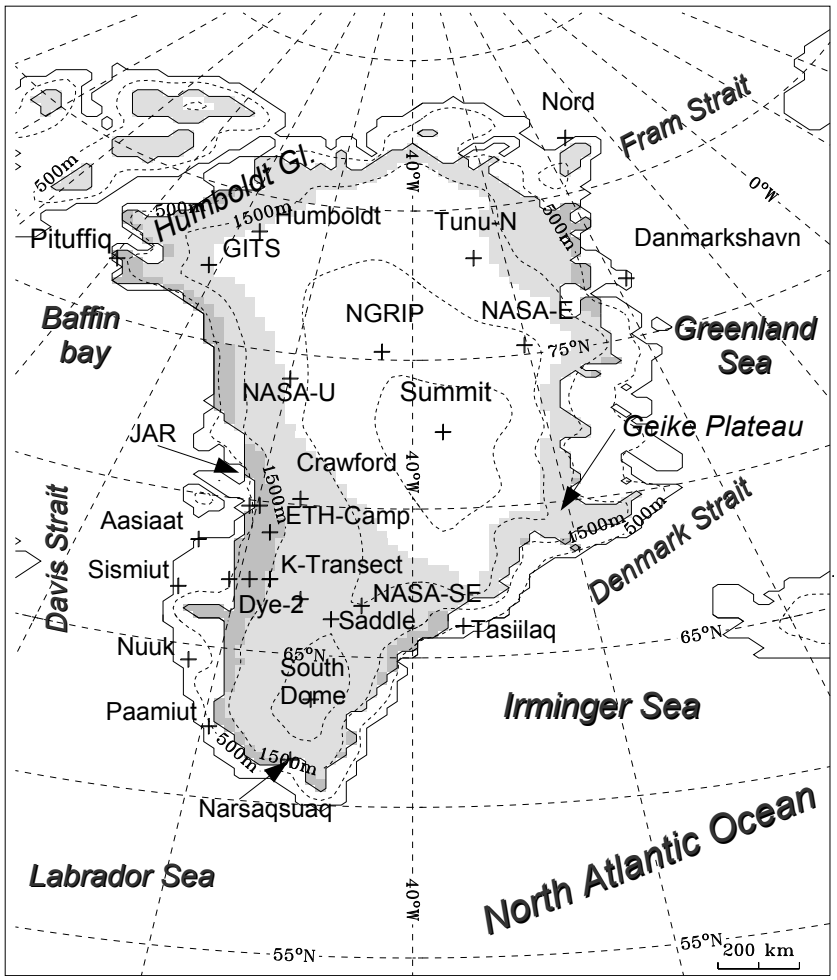

Figure 2.5 : Map of the domain of the simulation showing the MAR mass balance zones distribution on the Greenland ice sheet and locations quoted in the text. From dark to light grey on the ice sheet: the ice sheet ablation zone (including also the superimposed ice zone), the percolation zone (including also the wet snow and the flush zone) and the dry snow zone used to initialize the snow model at the beginning of the simulation. Finally, the scale in kilometre is shown.

We enlarged the integration domain previously used by Filip Lefebre (2002) to the whole Greenland (see Figure 2.5). It is surrounded by Baffin Bay, Davis Strait, Labrador Sea, the Atlantic Ocean, Denmark Strait,

Greenland Sea and the Arctic Ocean. The chosen resolution is 25km which is a good compromise between the computing time and a reasonable representation of the different SMB zones (Lefebre et al., 2005). The domain size is 2000 km by 3500 km with a minimum of 10 grid points between the Greenland ice sheet and the domain boundaries.

Usually, the prevailing Atlantic lows pressure areas cross the integration domain from the southern boundary to the eastern one. Therefore, the south(east)ern lateral boundary was chosen 30 grid points away from the ice sheet to ensure the possible development of (mesosclale) circulations (precipitation) which are not excessively constrained by the lateral boundaries. The topography and the land mask[23] for Greenland are based on Bamber et al. (2001).

2.2.2 Atmospheric model setup

The atmospheric part of MAR model has 30 levels. The lowest one has been put at 3 m above the surface, the 4 next levels are situated at 6 m, 12 m, 24 m, 48 m. On the one hand, levels in the boundary layer allow us to model the katabatic winds which are found to play an important role in the surface energy balance (Duynkerke and van den Broeke, 1994; Van den Broeke, 1994). On the other hand, a first level at 3m allows to easily compare MAR results with Automatic Weather Station (AWS) observations.

The time step was chosen to be 150 seconds which has been found the maximum that could be allowed at 25 km resolution for Greenland without precision and stability losses.

23 i.e. ocean, tundra or ice sheet

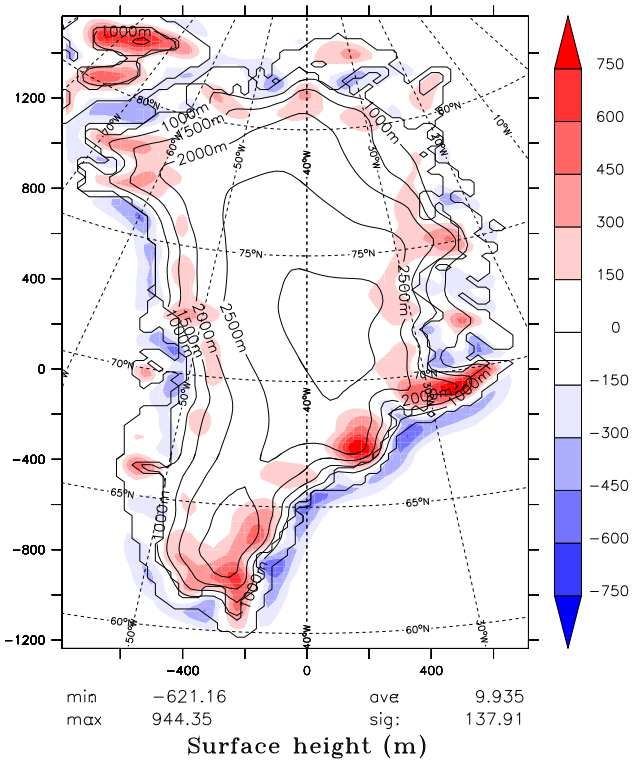

Figure 2.6 : MAR surface height (solid line) and the MAR/ERA-40 difference surface height (red/blue filled area).

The ERA-40 reanalysis (1977-2002) and after that, the operational analysis (2002-2005) from ECMWF are used to initialize the meteorological fields at the beginning of the simulation and to force the lateral boundaries every 6 hours with temperature, specific humidity and wind components which are interpolated in time. The (re)analysis is available every 6 hours at a resolution of one degree. It consists of a global climatological time series of model-consistent data generated by a numerical weather prediction model run retrospectively, feeding in all available observations to a 3D-Var data assimilation system (Simmons and Gibson, 2000). Since the end of the seventies, remote sensing observations are added to the assimilated station

and weather balloon (sounding) observations. It has been validated over Greenland with DMI and GC-Net observations by Hanna et al. (2005). The reanalysis prescribes also the SSTs and the sea-ice extent in SISVAT during the simulation. The ECMWF analysis sea-ice coverage is derived from the satellite passive microwave data (SMMR and SSM/I data set).

Figure 2.6 illustrates discrepancies in the topography used by MAR (with a resolution of 25 km) and by the lateral boundary forcing data (with a resolution of 1° ~ 100 km). The differences are largest along the south-eastern coastal mountainous range.

Begin	1st September 1977	
End	31th December 2005	
Domain	80 x 140 grid points (2000 x 3500 km)	
Resolution	25 km	
Time step	150 s	
1st atmospheric level	3 m	
Vertical levels	Atmosphere (MAR)	30 levels
	Snow (SISVAT)	20 levels
	Tundra (SISVAT)	7 levels
Forcing	Lateral boundaries	(Re)Analysis 6-hourly
	SSTs	(Re)Analysis 6-hourly
	Sea ice	(Re)Analysis 6-hourly

Table 2.1: Summary of model and simulation setups.

2.2.3 Snow model setup

As pointed out by Lefebre et al. (2005), if one wants to simulate an ablation season on Greenland, it is preferable to begin the simulation at the end of the previous summer to reduce the problem of the snow model initialization. When we start the simulation at the beginning of the summer

that we want to study, we have to cover the ice sheet and the tundra with the winter snow pack. Precipitation climatologies or reanalysis can be used to initialize the snow model but previous simulations showed a very large sensitivity to the initial conditions used in the snow model. The results are particularly sensitive to the initial snow height and the snow properties above the tundra and the ablation zone given the albedo feedback (Lefebre et al., 2005). For example, too large a snow pack height at the beginning of the summer above the ablation zone puts back the appearance of bare ice (with a lower albedo) in the ablation zone which can considerably reduce melt.

The initial location of the ELA is based on Zwally and Giovinetto (2001). As described in Lefebre et al. (2005), the percolation and the dry snow zones are initialized by 10 m of no-dendritic snow (with respective densities of 500 kg/m^3 and 300 kg/m^3), and over the ablation zone, an ice pack is prescribed at the beginning of the simulation (i.e. the first September). Later, the snow pack evolves during the simulation. If the snow pack height becomes higher than 15m, the height of the deeper layer in the snow model is divided by two. Similarly, 2m of ice are added at the bottom of the snow pack if the snow pack height becomes lower than 8m. Therefore, we suppose that the ice sheet mask here is fixed because we simulate only the current climate. In climate change simulations, the ice sheet should have the possibility to melt completely.

2.2.4 Simulation setup

The simulation starts in September 1977 and lasts till December 2005. To reduce at the maximum the influence on the results of the snow model initialization in the summer 1979, we have started the simulation at the end of 1977 to have a full year (1978) of spin-up. This 28-year simulation starting with the beginning of satellite observations, is the longest simulation

of the Greenland climate made with a regional model until now (Box et al., 2006; Fettweis et al., 2006). The previous simulation of the Greenland ice sheet made with MAR by Filip Lefebre was limited to the South of Greenland and covered only 4 months in 1991.

Such a simulation would take too much CPU time if one wanted to perform it on only one CPU given that MAR model is not yet a parallellized code. The computer time needed to model one year over Greenland with our configuration is in the order of 1 month CPU. Therefore, 2 years and half of computational time would be necessary to process continuously our 28-year simulation on only one computer! That is why we launched in parallel a series of shorter simulations beginning each time on different dates which we gathered by forming the 25 years afterwards. We have used so several CPUs from the European Center's *hpcd* cluster (ECMWF, England), from the UCL-CISM's *decci* cluster as well as the UCL-ASTR's *eole* and *idlserv* clusters allowing us to have the 25 years in a record time. On each CPU, we simulated on average 5 years by preserving only the 2 last simulated years. For example, to simulate the years 1990 and 1991, we started the simulation at the end of summer 1987. The first 3 years are used as a spin-up to limit at maximum the impact of a reinitialisation of the snow model compared to an uninterrupted simulation. By comparing/recovering simulations from different initialisation date, we robustly validated this manner of proceeding. It was allowed because the ice sheet mask is fixed here during the simulation.

Chapter 3

Evaluation of MAR with GC-Net measurements in 1998

The MAR model was adapted by Lefebre (2002) in order to make it more appropriate for the modelling and study of the Greenland surface mass balance. The improved snow model was validated at ETH-Camp (Lefebre et al., 2003) and a 3D version of the coupled snow-atmosphere model was compared with in-situ observations over South Greenland during the 1991 ablation season (Lefebre et al., 2005). This study notably highlighted a significantly better treatment of the near surface state variables in MAR than in the relatively coarse European Centre for Medium-Range Weather Forecasts (ECMWF) 15-year reanalysis (ERA-15). Since Lefebre et al. (2003, 2005) validations, the spatial resolution has been increased from 20km to 25km to encompass the whole Greenland in the integration domain, MAR has been run on several years to reduce the sensitivity to the initialization of the snow pack and a new ECMWF reanalysis data set has been used. The snow model has been incorporated in a 1D surface vegetation atmosphere transfer scheme, a new radiative scheme has been implemented, the advection scheme has been improved, the water conservation in the MAR hydrological scheme has been corrected and various improvements have been made by continual model refinements. Therefore, a new brief

evaluation of this MAR version with in-situ data is needed to validate our results. It is the aim of this third chapter in which temperature, humidity, wind, surface pressure, snow height and surface radiation simulated by MAR are compared with 13 GC-Net AWSs in 1998[24], one of the warmest years since the beginning of industrial era. The MAR results are also validated by comparison with the ERA-40 reanalysis data over the same period. The conclusions of this evaluation fully agree with what has been found by Lefebre (2002) and Lefebre et al. (2005) for previous MAR versions.

3.1 Data

The GC-Net was initiated in the spring of 1995 with the intention of monitoring climatological and glaciological parameters at various locations on the ice sheet over a period of at least 15 years. In 1998, GC-Net consisted of 15 AWS distributed over the Greenland ice sheet (Steffen and Box, 2001). Four stations are located along the crest of the ice sheet (2500m-3200m elevation range), nine stations are situated close to the 2000m contour line and two stations are positioned in the ablation region (962m-1150m). At each AWS, a total of 32 climate parameters are sampled every 15 s averaged over an hour, and then transmitted via a satellite link. GC-Net instruments are factory-calibrated; nonetheless, on-site relative calibrations are performed during most annual site visits to ensure good quality of the data. Each AWS is equipped with a number of instruments to sample the following[25]:

- *air temperature* using two different instruments at two measurements heights (typically between 1 and 3m and between 3 and 10m). As a

24 The year 1998 has been chosen because we have obtained the GC-Net data set for this year only.

25 Current measurements can be found at
http://cires.colorado.edu/science/groups/steffen/gcnet/

result, a total of four air temperature measurements is available with a relative accuracy of 0.1°C and an absolute accuracy of approximately 0.3°C. Type E thermocouples are notably used, mounted in radiation shields which are not actively ventilated but "naturally aspirated" due to the constant katabatic winds along the slope of the ice sheet. Some overheating is possible in areas of low wind speed and high solar radiation, like on top of the ice sheet;

- *wind speed* and *wind direction* at each measurement height with an instruments accuracy of 0.1 m s^{-1} and of 5°, respectively;
- *relative humidity* (RH) at each measurement height with an accuracy of 5 % if RH < 90% and of 10 % otherwise. The derived specific humidity is used here in the comparison;
- *surface pressure* accurate to within a 0.1hPa;
- surface height change (i.e. the *snow pack height*);
- *snow pack temperature* at ten depths;
- *downward, upward short-wave radiation* with an instrument accuracy of 5-15% and *net radiation* with an instrument accuracy of of 5-50%. Cassano et al. (2001) noted that net radiation measurements indicate periods with minimum net radiation during daylight hours and/or prolonged periods of nearly constant/zero net radiation. These problems are probably caused by hoarfrost formation on the radiometer domes. In addition, the radiation measurements are biased by AWS platform shadow or reflections, by shadings and when the Sun is near the horizon (Steffen et al., 1996). Therefore, net radiation measurements will not be used in this comparison and solar radiation samples must be considered with caution;

See Steffen et al. (1996) and Steffen and Box (2001) for more details about the instrument calibration.

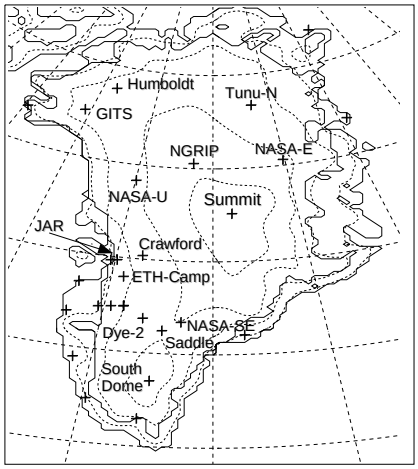

ID	Name	Lat. [°N]	Lon. [°W]	Elev. [m]	MAR Lat.	MAR Lon.	MAR Elev.
1	Swiss Camp	69.57	49.30	1149	69.59	49.06	1151
2	Crawford-1	69.88	46.97	2022	69.93	46.56	2068
3	NASA-U	73.83	49.50	2368	73.88	49.75	2316
4	GITS	77.14	61.10	1887	77.13	60.51	1849
5	Humboldt Gl.	78.53	56.83	1995	78.54	57.12	1960
6	Summit	72.58	38.50	3208	72.29	37.78	3242
7	Tunu-N	78.02	33.99	2020	78.06	33.50	2066
8	DYE-2	66.48	46.28	2165	66.55	46.22	2129
9	JAR-1	69.50	49.68	962	69.56	49.69	775
10	Saddle	66.00	44.50	2559	65.94	44.41	2486
11	South Dome	63.15	44.82	2922	63.23	44.98	2810
12	NASA-E	75.00	30.00	2631	75.02	30.41	2643
13	Crawford-2	69.91	46.85	1990	69.90	47.21	1924
14	NGRIP	75.10	42.33	2950	74.98	42.60	2948
15	NASA-SE	66.48	42.50	2579	66.43	42.81	2444

Table 3.1 : GC-Net automatic weather station location. Geographical position of the closest MAR grid point used in this comparison is also shown. Measurements from GITS AWS are not used here. Figure above gives an overview of AWS location on the Greenland ice sheet (See also Figure 2.5).

3.2 Comparison

Figures 3.1-3.4 compare the daily temperature, wind speed and wind direction, humidity, surface pressure, solar radiation (incoming and outcoming) and snow pack height from the MAR model to the GC-Net measurements in 1998 at JAR-1 located in the western ablation zone, at DYE-2 in the southern wet snow zone, at Humboldt on the dry snow line in the North Greenland and at NASA-E in the eastern dry snow zone. Figures 3.5 and 3.6 demonstrate the MAR ability to simulate the daily cycle for the most important near-surface atmospheric parameters during winter (from 1st February to 31th March) at Crawford Point-2 located near the western equilibrium line in the percolation zone, and during summer (from 15th June to 15th August) at South Dome in the southern percolation snow zone. The averaged diurnal cycle is evaluated in December and July at ETH-Camp (or called Swiss Camp) in Figure 3.7. The variations of the snow pack height is evaluated in Figures 3.1-3.8 for ten AWS's. Finally, Table 3.2 lists statistics about this comparison. The MAR values are taken at the grid point the closest to the AWS location and at the first level of the model (.i.e. at 3m). We use the AWS measurements the closest to 3m. The MAR outputs are generally in close agreement with observations although MAR 25km-resolution can not resolve the specificities of measurement sites. The following paragraphs comment the quality of the simulation per each parameter measured.

3.2.1 Temperature

The model has been found to accurately represent the seasonal and synoptic temperature variability as well as the diurnal cycle with a mean correlation of 0.93 with the hourly GC-net observations. During the polar

night, the absence of sunlight damps the daily thermal amplitude (Figure 3.7). At the beginning of spring, the Sun is already powerful enough to reactivate the daily cycle as shown in Figure 3.5. In summer, the diurnal cycle dominates the temperature variability. At JAR-1 in the ablation zone (see Figure 3.1), the diurnal melt (which prevents the surface temperature to exceed 0°C) as well as the night refreezing temper the synoptic variations and the daily cycle. Higher in altitude the daily amplitude can easily reach 15°C as it was observed at South Dome (Figure 3.6).

It should be noted that positive temperatures (i.e. >0°C) were reached several times at South Dome (2922m) during summer of 1998 (15th June, 20th July, 1st August). This is rare since the monthly mean 1995-1999 temperature for July at South Dome is -8.8±0.9 °C (Steffen and Box, 2001). These heat peaks are well simulated by MAR.

Averaged over the year and over all AWS sites, MAR is 3.98°C too cold compared to GC-Net measurements. This cold bias is more pronounced during the polar night and at AWS sites located on the crest of the ice sheet. In summer, this bias is considerably reduced. For example, the bias is of +0.17°C (resp. -3.5°C) in July and of -2.5°C (-10°C) in January at Swiss Camp (resp. Summit). This bias will be discussed further in this chapter conclusion.

3.2.2 Wind

The katabatic wind signature is clear in both MAR and observed fields for AWS sites situated along the ice sheet slope. At Crawford Point-2 and at JAR-1, for example, the main wind component comes from the east, at Humboldt from the south and at NASA-E from the west. The systematic katabatic wind direction discrepancies between MAR and GC-Net come from the model resolution, which is clearly insufficient to take explicitly into

account the specificities of measurement sites. At the top of the ice sheet, the wind direction is rather driven by the synoptic variability (Figures 3.4 and 3.6).

The modelled wind speed synoptic fluctuations are in phase with the observations. In summer, the wind speed exhibits a diurnal cycle, superimposed on the synoptic time scale variations like the temperature (Figure 3.6 and 3.7). The daily wind speed maximum occurs when the air temperature is minimal which is consistent with primarily katabatically forced winds. However, the summer observations at Swiss camp shows a lag of some hours in the maximum wind speed relative to the minimum air temperature. Other observations of the diurnal cycle of katabatic winds in Greenland and Antarctica indicate a similar lag (Wendler et al., 1988; van den Broeke et al., 1996; Cassano et al., 2001). This lag can be seen as an inertial response of the wind field to the thermal forcing reflecting complex interactions between the near-surface katabatic flow and vertical mixing through the boundary layer (van den Broeke et al., 1996). The MAR model successfully simulates this lag contrary to the Polar MM5 model (Cassano et al., 2001). On average over all AWS sites, MAR overestimates the wind speed as a result of the cold bias. This enhanced drainage flow is forced by colder near-surface air in the model since the SBL wind on the ice sheet is a primarily katabatically forced wind. Amplified katabatic driven winds lead down slope to lower SBL temperatures.

3.2.3 Specific Humidity

The atmospheric moisture content is strongly dependent on the air temperature. Therefore, the specific humidity exhibits also a diurnal cycle superimposed on the synoptic variations in summer (Figures 3.6). As for the temperature, most of the synoptic and daily variations in the specific

humidity are well depicted by the model, while the diurnal cycle is more pronounced in the observations at Swiss Camp (Figure 3.7). It is clear that many errors in the modelled specific humidity mirror biases in the modelled temperature time series. A cold bias in the model implies a reduced capacity of the model atmosphere to hold water vapour and leads to a negative bias in the modelled specific humidity. Consequently, an accurate simulation of the low-level moisture content of the atmosphere requires an accurate prediction of the near-surface air temperature.

According to the previous identified negative bias in the modelled air temperatures, MAR specific humidity is on average 0.24 g kg^{-1} lower than the GC-Net measurements. However, the simulated specific humidity is less in phase with the observations than the MAR air temperature. Given that the errors are larger on the humidity measurements than on the measured temperature, this suggests that the lower correlation (0.87) is the result of instrumental errors rather than model errors.

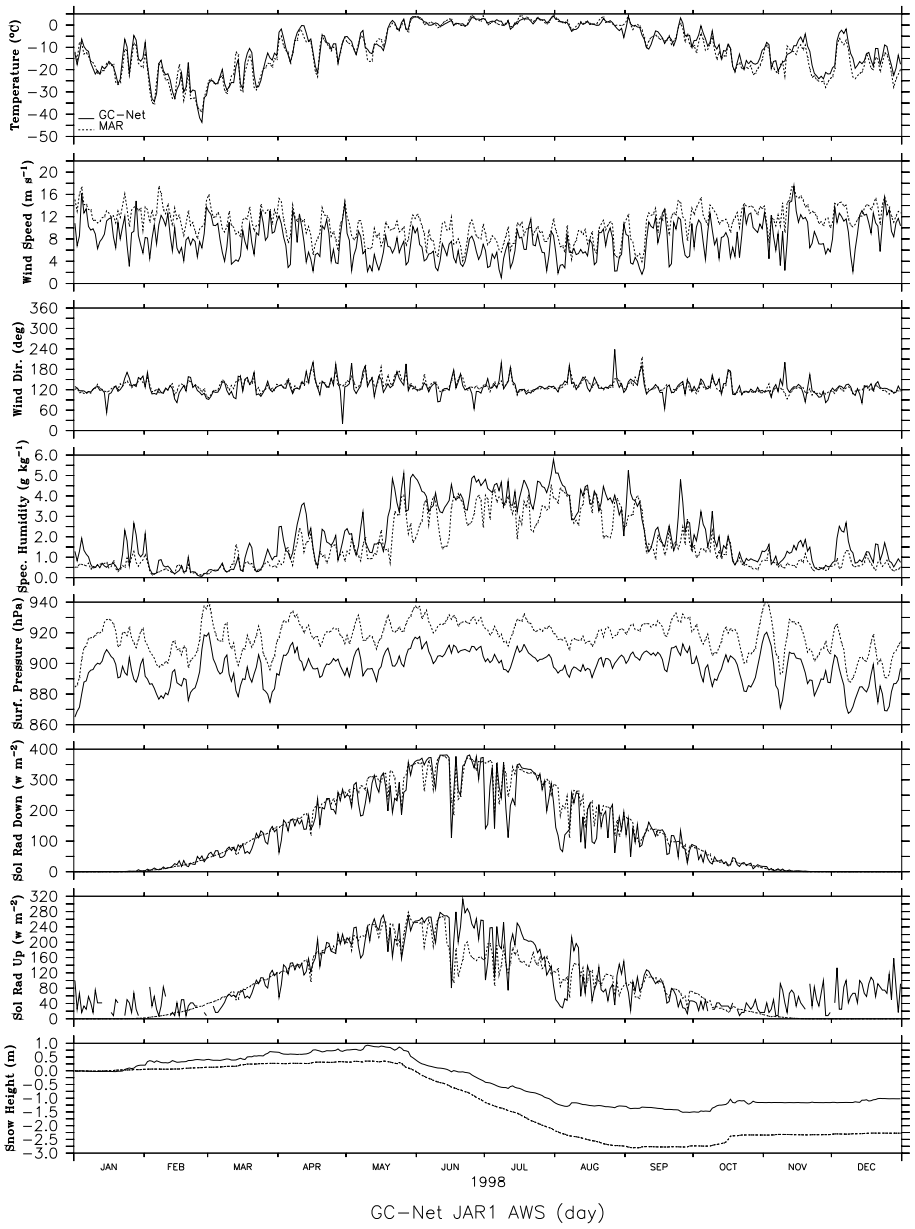

Figure 3.1 : 1998 time series of the daily AWS (thick solid line) and MAR data (thin dashed line) at JAR-1 AWS. See the previous page for more details.

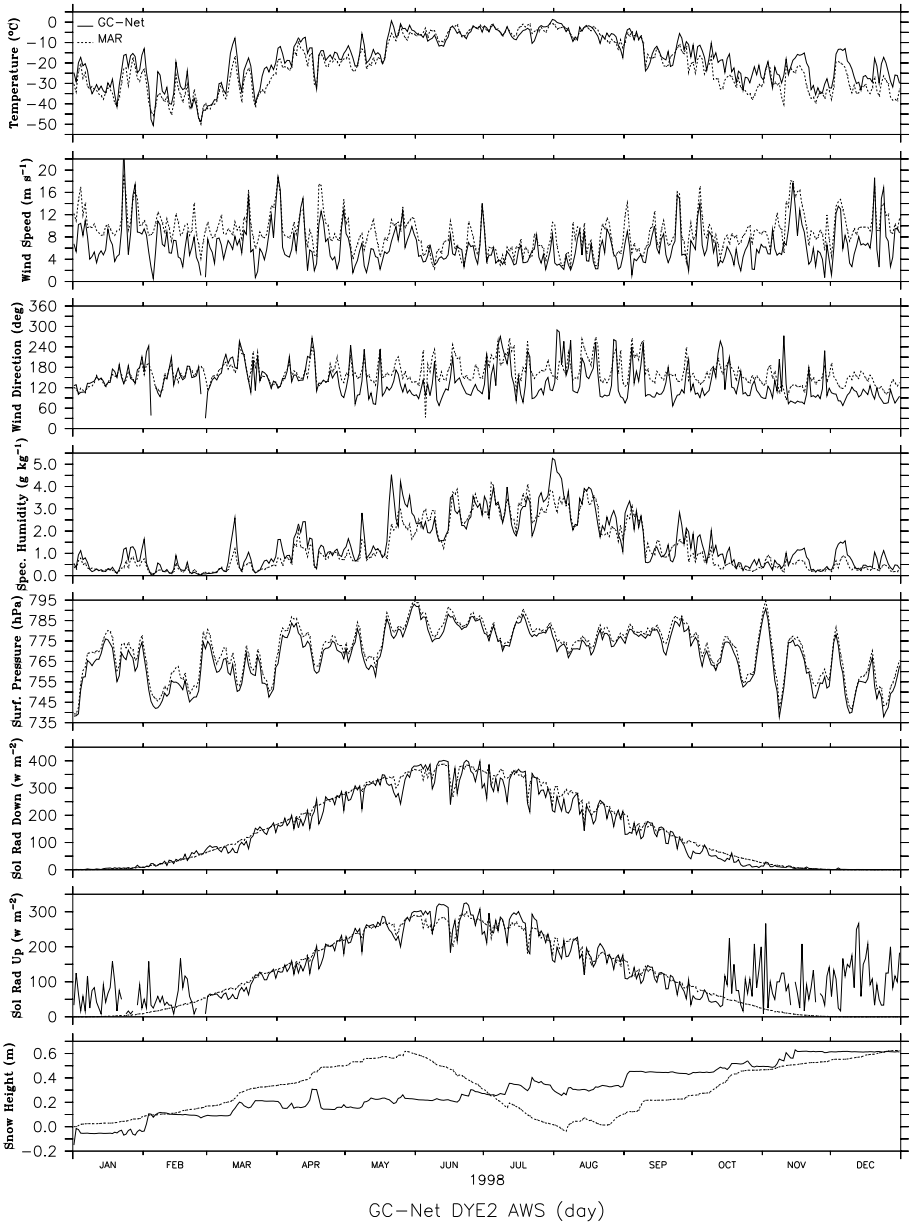

Figure 3.2 : Same as Figure 3.1 but for DYE-2 AWS.

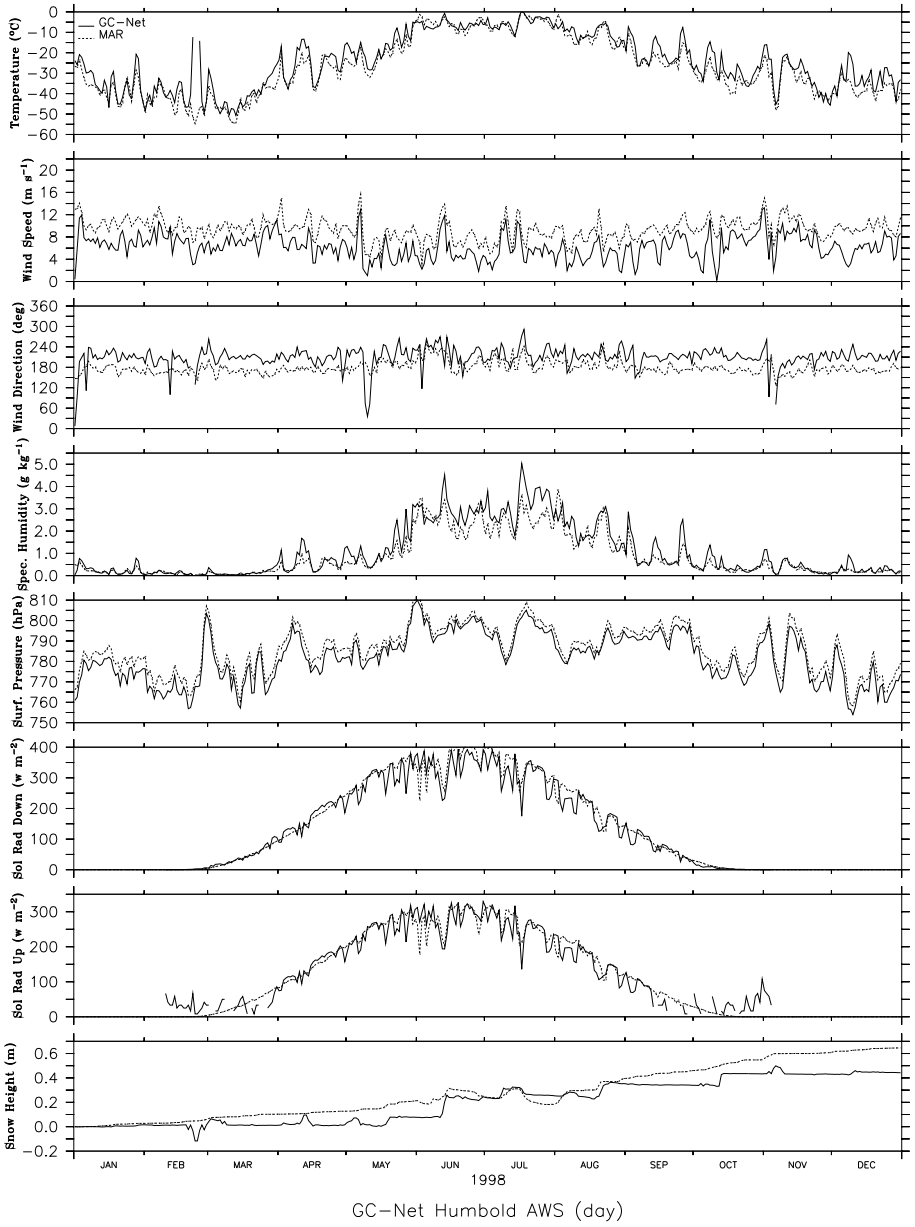

Figure 3.3 : Same as Figure 3.1 but for Humboldt AWS.

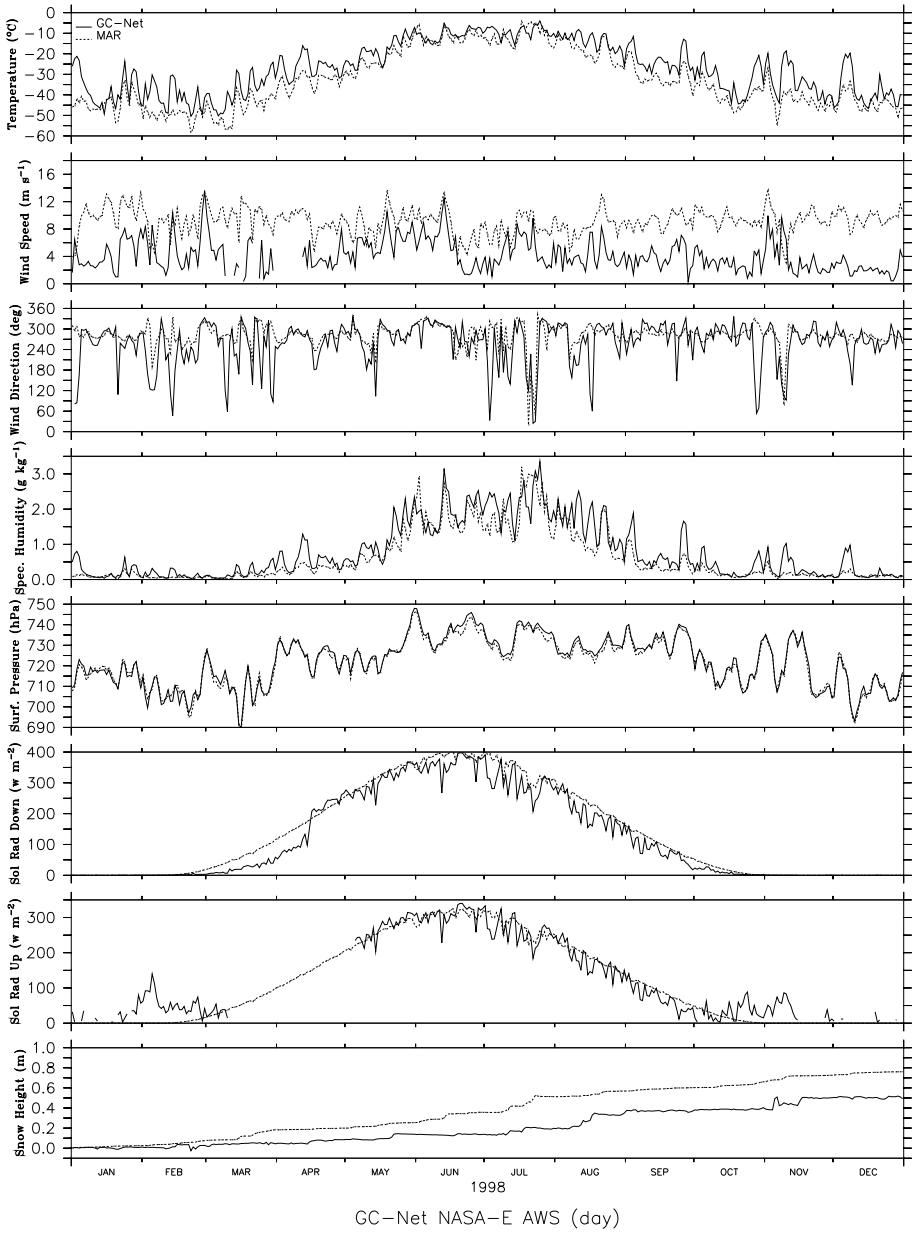

Figure 3.4 : Same as Figure 3.1 but for NASA-E AWS.

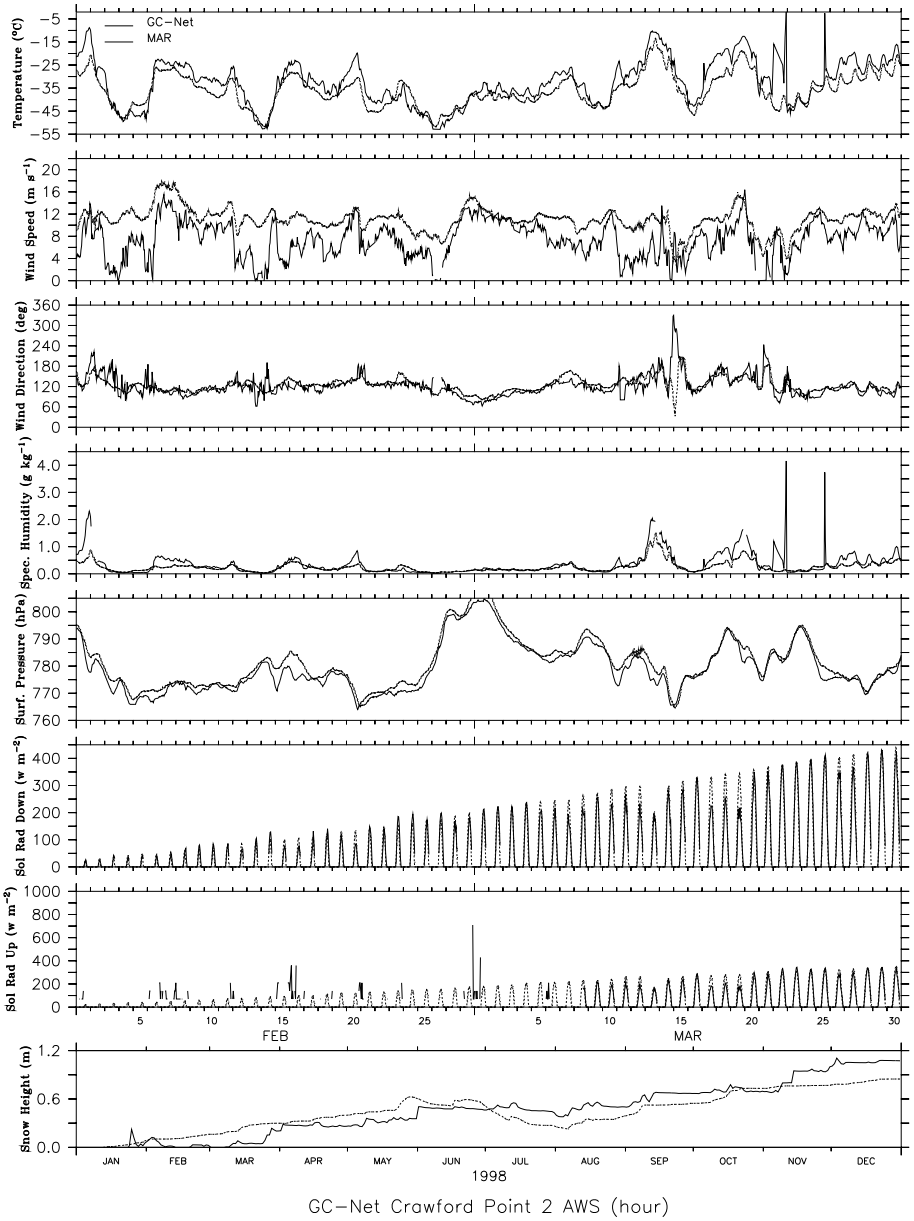

Figure 3.5 : Same as Figure 3.1 but for Crawford Point-2 in February and March 1998 (hourly value).

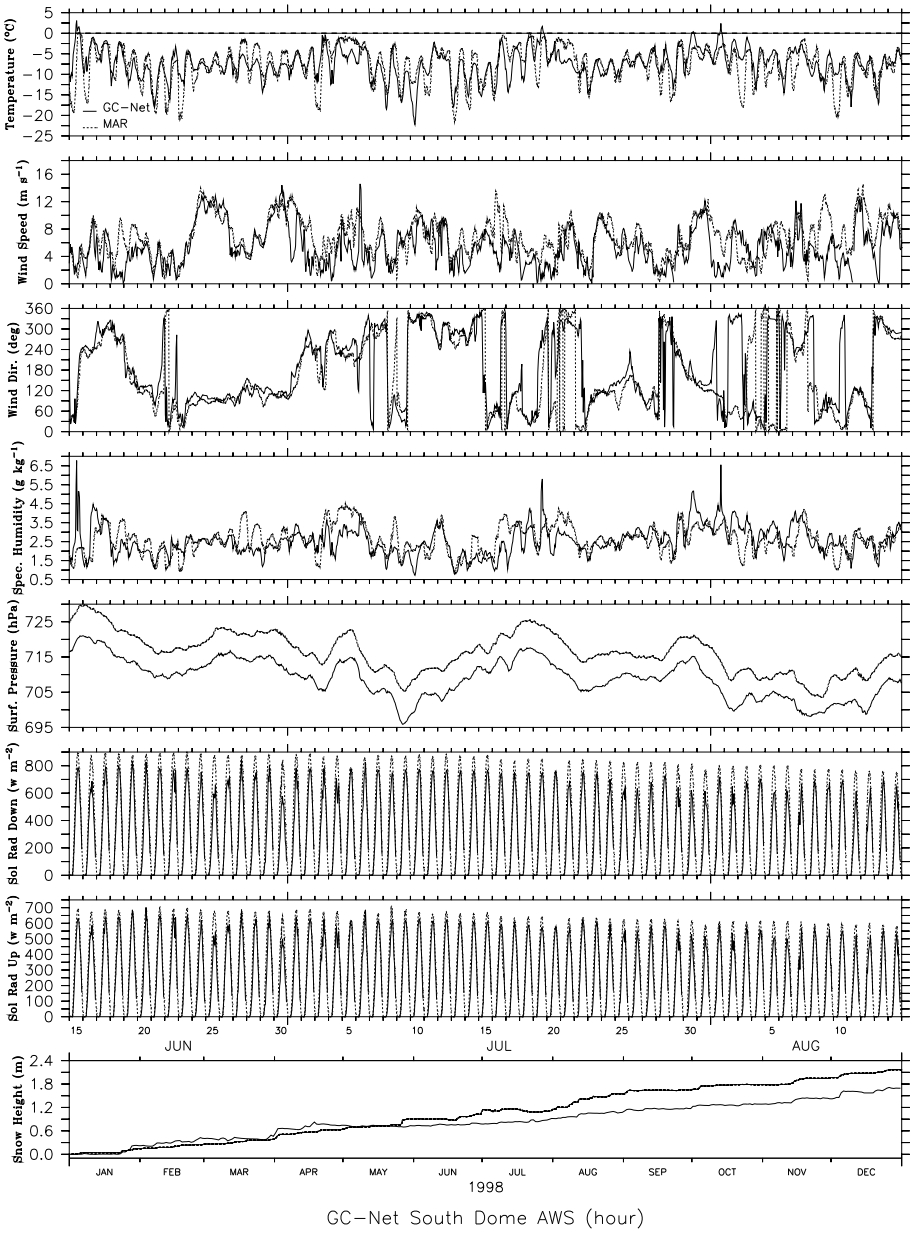

Figure 3.6 : Same as Figure 3.1 but for South Dome AWS in summer (from 15th June to 15th August) 1998 (hourly value).

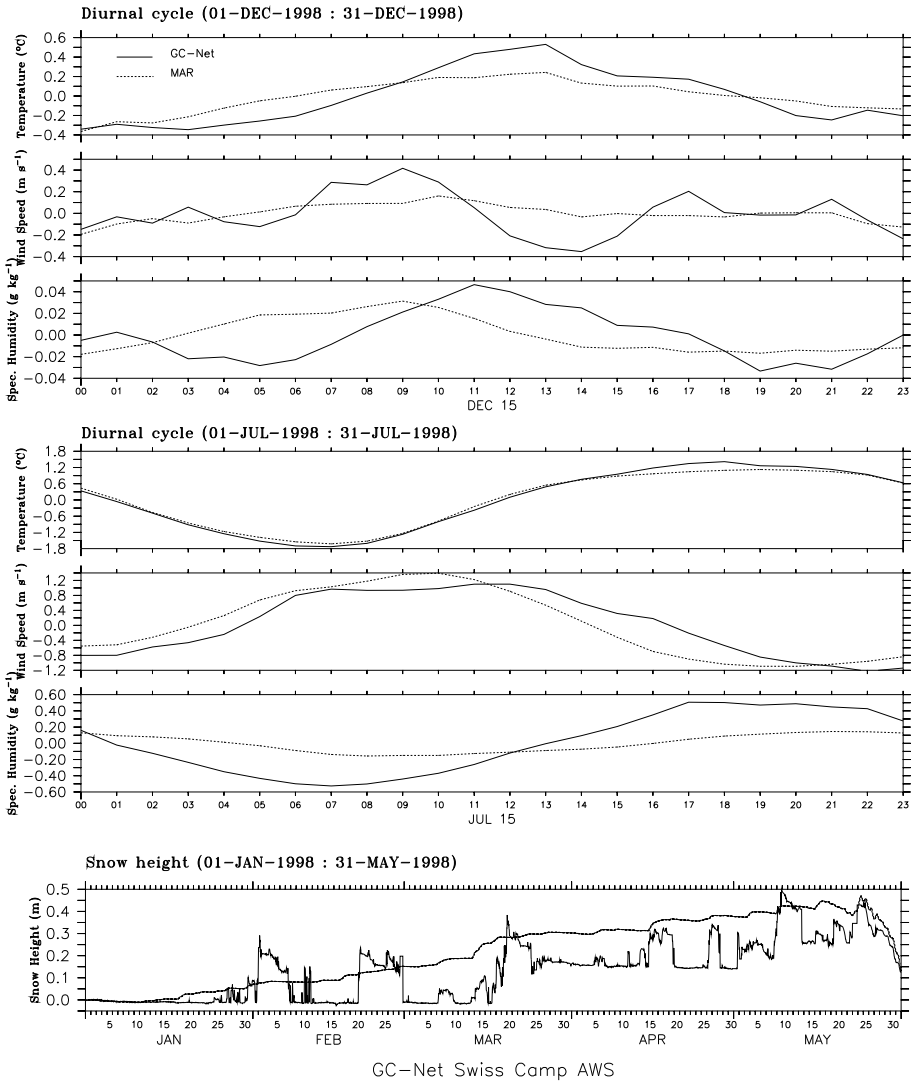

Figure 3.7 : Averaged diurnal cycle calculated from Swiss Camp observations (dark line) and from MAR data (dashed line) for December and July 1998. The averaged diurnal cycle is plotted for temperature, specific humidity and wind speed. Values on the temporal axis are in hours. Below, the snow height evolution from 1st January 1998 to 31th May 1998.

3.2.4 Surface pressure

The MAR skilfulness to accurately model surface pressure is illustrated in Figures 3.1-3.6. The agreement with the observations is excellent (with a mean correlation of 0.99) except of course where the AWS site and the representing MAR grid point are not at the same altitude (e.g. JAR-1).

3.2.5 Snow height

The simulated snow height matches well with the GC-Net accumulation rates although MAR overestimates the snow pack in some stations. On the one hand, these measurements depend very much on the local conditions (blowing snow, snow dune formation, ...), while MAR values represent an average on a grid cell measuring 25 km x 25 km. In addition, the blowing snow erosion is not taken into account in this simulation. On the other hand, MAR overestimates slightly the (solid) precipitation at the top of the ice sheet (see Chapter 4). At JAR-1, the representative MAR grid point is situated 200 m lower (due to the smoothing of the topography) than the station which gives a higher ablation in MAR and less solid precipitation (accumulation) in summer.

3.2.6 Solar radiation

The MAR simulation accurately represents the seasonal evolution of the downward solar radiation but tends to overestimate this quantity with an averaged bias of +23 W/m^2. Although the errors on the measured solar fluxes are large in the AWS fields (see section 3.1), this overestimation in the simulation of the incoming short wave flux was already identified by Lefebre et al. (2005) in a previous version of MAR using also the Fouquart and Bonnel (1980) formulation for solar radiation.

The AWS's fail to sample the upward short wave flux when it reaches low values in autumn/spring as can be seen in Figures 3.1-3.4. That is why it is just shown for information in Figures 3.1-3.6 and is not listed in Table 2.2.

Time series of the downward short wave radiation in Figures 3.5 and 3.6 are dominated by the diurnal cycle but are modulated by synoptic variability in the cloud cover. It is encouraging to note that the model appears to accurately represent the radiative effects of the cloud cover on a number of days at Crawford Point-2 (e.g. on February 14-15, on March 14). Differences between the modelled and observed incoming solar flux during other periods (e.g. on March 17-19) are caused by errors in the model-predicted cloud cover or errors in the measurements. At South Dome, the comparison is dominated by an overestimated modelled downward solar flux during both clear sky and cloudy conditions.

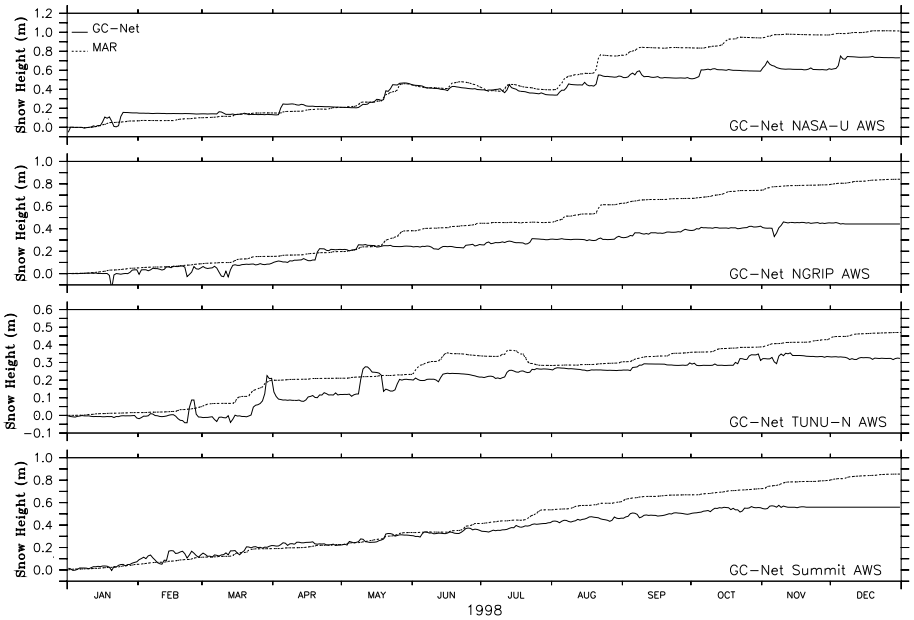

Figure 3.8 : Snow height time series for four other GC-net AWS's.

Table 3.2: Statistics for the 13 AWS's during 1998: mean observed value, difference (bias) between the observed one and the MAR mean value, MAR correlation and RMSE (Root Mean Square Error) with the GC-Net observations.

Station	Variables	Mean[26]	Bias[27]	Corr. Coef.[28]	RMSE[29]
Crawford Point-2	Temperature (°C)	-18.06	-2.71	0.93	5.37
	Wind Speed (m/s)	7.47	2.88	0.75	3.72
	Wind Dir. (degree)	137.9	-8.1	0.56	33.12
	Spec. Humidity (g/kg)	1.41	-0.27	0.86	0.7
	Surf. Pressure (hPa)	791.5	0.9	0.99	1.88
	Short Wave Down. (W/m^2)	199.6	15.2	0.97	55.73
Dye-2	Temperature	-17.7	-3.03	0.93	5.67
	Wind Speed	6.36	2.55	0.76	3.61
	Wind Dir.	138.7	23.4	0.51	56
	Spec. Humidity	1.44	-0.21	0.89	0.6
	Surf. Pressure	768.3	3.2	0.99	3.55
	Short Wave Down.	206.4	14.6	0.97	64.39
Humboldt	Temperature	-24.21	-2.5	0.96	4.77
	Wind Speed	6.29	3.12	0.7	3.62
	Wind Dir.	213.3	-34.4	0.41	45.06
	Spec. Humidity	1.08	-0.21	0.93	0.51
	Surf. Pressure	782.1	4.2	0.99	4.57
	Short Wave Down.	212.6	10.5	0.96	53.16

26 The *mean* is the average over 1998 of the AWS observed hourly values.

27 The *bias* is defined as the 1998 averaged difference (MAR – GC-Net) between the MAR and the AWS observed hourly value of a given variable and identifies any systematic differences between MAR simulation and the GC-Net observations.

28 The *correlation coefficient* (Corr. Coef.) measures the agreement in the phase of the variations in the modelled and observed time series.

29 The *RMSE* (root mean square error) is calculated as the square root of the hourly squared difference between the AWS observation and the MAR simulated value of a given variable. It is a measure of the typical difference between MAR modelled and AWS observed values.

Station	Variables	Mean	Bias	Corr. Coef.	RMSE
JAR-1	Temperature	-9.79	-1.04	0.96	3.07
	Wind Speed	7.77	3.09	0.75	3.92
	Wind Dir.	122.7	7.1	0.54	26.64
	Spec. Humidity	2.13	-0.54	0.85	0.96
	Surf. Pressure	897.3	20.2	0.98	20.34
	Short Wave Down.	193.6	17.8	0.93	81.67
NASA-E	Temperature	-28.74	-3.99	0.9	7.59
	Wind Speed	4.35	4.85	0.34	5.58
	Wind Dir.	260.2	21.2	0.29	79.32
	Spec. Humidity	0.79	-0.19	0.88	0.43
	Surf. Pressure	722.3	-0.7	0.99	1.91
	Short Wave Down.	207.2	29	0.96	67.66
NASE-SE	Temperature	-15.93	-5.37	0.88	8.25
	Wind Speed	5.49	1.11	0.65	2.5
	Wind Dir.	193.2	-18.7	0.57	120.6
	Spec. Humidity	1.57	-0.35	0.83	0.72
	Surf. Pressure	746.7	-3	0.99	3.38
	Short Wave Down.	274.8	9.9	0.97	69.3
NASA-U	Temperature	-22.18	-3.19	0.95	5.24
	Wind Speed	7.02	2.87	0.73	3.49
	Wind Dir.	135.4	7.2	0.62	25.5
	Spec. Humidity	1.1	-0.2	0.9	0.49
	Surf. Pressure	747.7	4.4	0.96	5.83
	Short Wave Down.	237.7	-1.7	0.97	57.18
NGRIP	Temperature	-28.92	-6.66	0.93	8.74
	Wind Speed	4.51	2.36	0.72	3.03
	Wind Dir.	178.2	12.5	0.62	39.81
	Spec. Humidity	0.85	-0.5	0.83	0.72
	Surf. Pressure	692.9	0	0.99	1.93
	Short Wave Down.	203.2	15.1	0.97	57.08

Station	Variables	Mean	Bias	Corr. Coef.	RMSE
Saddle	Temperature	-16.16	-5.04	0.91	7.96
	Wind Speed	5.56	1.45	0.73	3.3
	Wind Dir.	176.2	2.5	0.7	59.55
	Spec. Humidity	1.51	-0.22	0.86	0.62
	Surf. Pressure	740.7	-1.4	0.99	2.02
	Short Wave Down.	240.7	20.8	0.97	69.69
South Dome	Temperature	-16.02	-4.56	0.91	7.28
	Wind Speed	6.5	1.17	0.79	3.11
	Wind Dir.	168.7	-9.2	0.68	85.36
	Spec. Humidity	1.57	-0.03	0.82	0.76
	Surf. Pressure	700.3	8	0.99	8.13
	Short Wave Down.	233.4	67.6	0.94	122
Summit	Temperature	-26.6	-7.44	0.91	9.76
	Wind Speed	3.91	1.4	0.74	2.56
	Wind Dir.	162.9	11.1	0.52	88.35
	Spec. Humidity	0.9	-0.29	0.87	0.53
	Surf. Pressure	667.9	-0.7	0.95	3.99
	Short Wave Down.	246.6	32.3	0.96	74.3
Swiss Camp	Temperature	-11.39	-1.96	0.96	3.82
	Wind Speed	8.58	2.47	0.67	3.83
	Wind Dir.	130.7	-1.5	0.51	28.51
	Spec. Humidity	1.9	-0.42	0.87	0.84
	Surf. Pressure	874	-0.7	0.98	1.99
	Short Wave Down.	183.7	36.4	0.95	81.87
Tunu-N	Temperature	-26.49	-3.51	0.95	5.76
	Wind Speed	5.66	3.56	0.61	4.05
	Wind Dir.	254.2	25.9	0.3	53.35
	Spec. Humidity	0.97	-0.09	0.89	0.48

Station	Variables	Mean	Bias	Corr. Coef.	RMSE
	Surf. Pressure	780.8	-3.1	0.99	3.73
	Short Wave Down.	229.2	8.8	0.96	53.73
Average over the 13 AWS's	Temperature (°C)		**-3.98**	**0.93**	**6.52**
	Wind Speed (m/s)		**2.5**	**0.68**	**3.58**
	Wind Dir. (degree)		**2.65**	**0.52**	**59.64**
	Spec. Humidity (g/kg)		**-0.24**	**0.87**	**0.64**
	Surf. Pressure (hPa)		**2.24**	**0.99**	**7.78**
	Short wave Down (W/m^2)		**23.17**	**0.96**	**70.86**

3.2.7 Comparison between MAR and ERA-40

Before concluding this chapter, we will present a brief comparison between MAR and ERA-40 results for 1998 to confirm what has been previously found by comparing MAR fields with GC-Net observations.

The ERA-40 reanalysis data is output from model compilations and assimilations of available satellite, station and weather balloon observations and is therefore expected to be the closest to the observations as possible. Over Europe, the quality of the reanalysis is considered as good because of the large number of observations that are used in the data-assimilation process. Over Greenland, however, observational data is much scarcer and the representation of some polar atmospheric/surface processes is sometimes limited, which increases somewhat the uncertainties on the ERA-40 reanalysis data (Hanna et al., 2005). However, comparing both model results can be useful to see if the previously found biases at the surface are reflected in the free atmosphere at a larger scale, and to check if the nested simulation is not in conflict with the lateral boundary forcing data.

Although most of regional model validations are made at a 850 hPa geopotential height, the comparison will be performed at 500 hPa given that

the Greenland summit reaches about 700 hPa at its peak. The 1° ECMWF reanalysis data is interpolated on the 25 km MAR grid. The methodology used is based on the MAR validation used over Europe by Marbaix (2000).

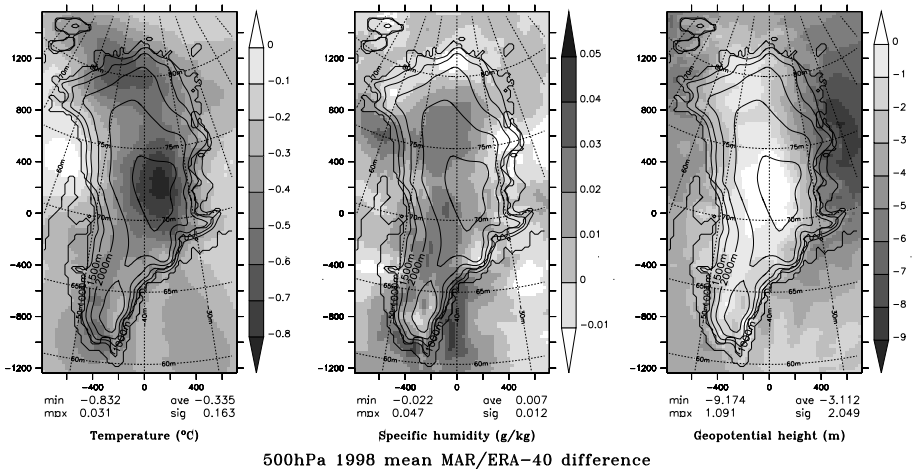

Figure 3.9 : Temporal mean of the 500 hPa temperature, specific humidity and geopotential height MAR/ERA-40 difference.

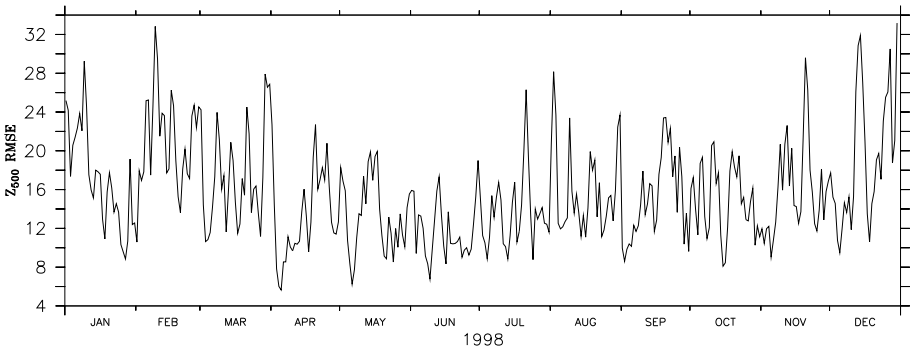

Figure 3.10 : 500 hPa mean geopotential height RMSE between MAR and ERA-40 for the whole Greenland domain excluding the lateral boundaries.

The previous mentioned SBL cold bias in MAR fields above the ice sheet is reflected in height and can be seen in Figure 3.9. We can also see this bias in the 500 hPa temporal mean geopotential height difference. MAR underestimates the 500 hPa mean geopotential height by some metres except

where it is too cold. Part of geopotential height differences also come from discrepancies in topography used by both models (see Figure 2.7). Both modelled specific humidity compare well.

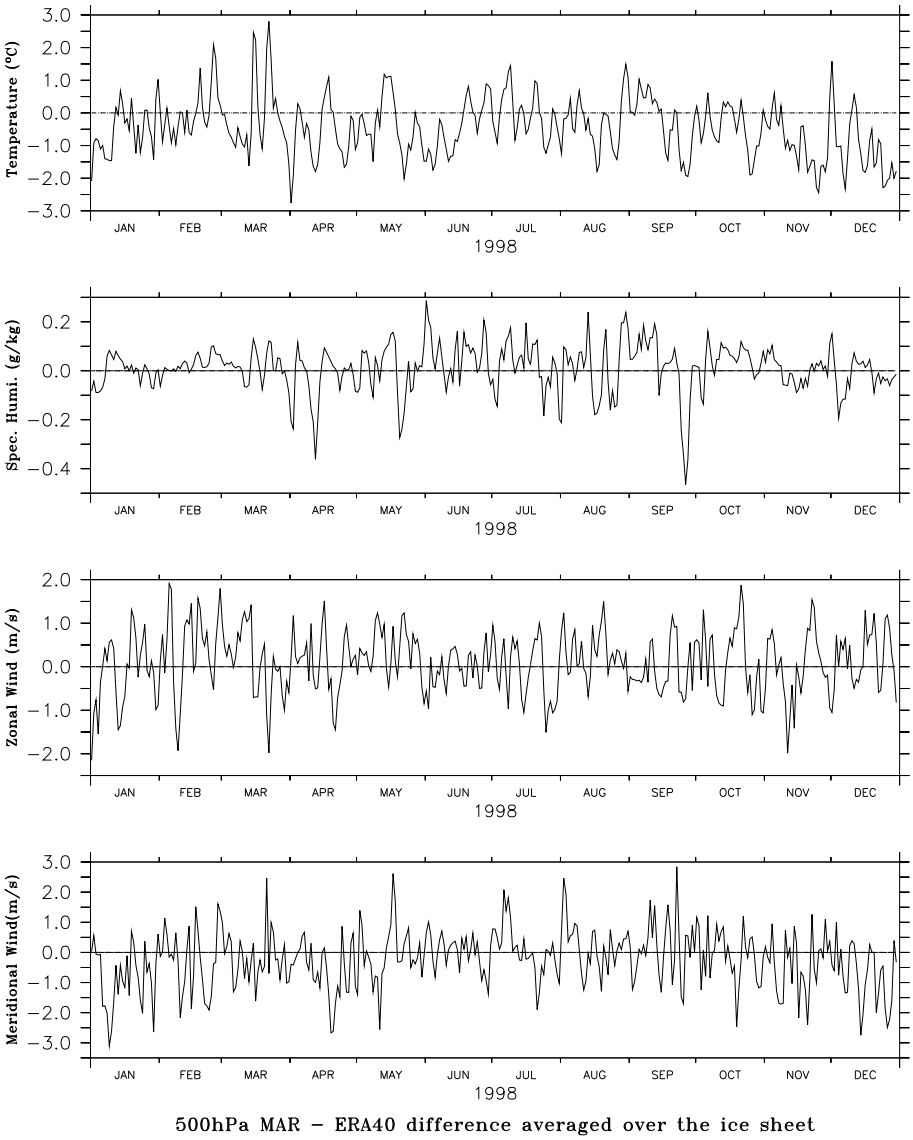

Figure 3.11 : Evolution of the 500hPa over the ice sheet mean temperature, specific humidity and wind speed difference between MAR and ERA-40 in 1998.

The ability of the nesting scheme to deal with synoptic perturbations entering and leaving the integration domain is illustrated in Figure 3.10 which shows the spatial averaged time series of the RMSE of the geopotential height. While the RMSE fluctuates around a roughly constant value, attributed to the equilibrium between the model and the constrain by the external forcing (Marbaix, 2000), the differences shown in Figures 3.10 and 3.11 are higher in the cold season according to which has been found in the MAR evaluation with GC-Net observations. In addition, Figure 3.10 and 3.11 do not show any trend. This indicates that the nesting procedure works well. To conclude, it is encouraging to note that the differences at 500hPa between both models remain small in both space and time over the ice sheet (Figures 3.9 and 3.11).

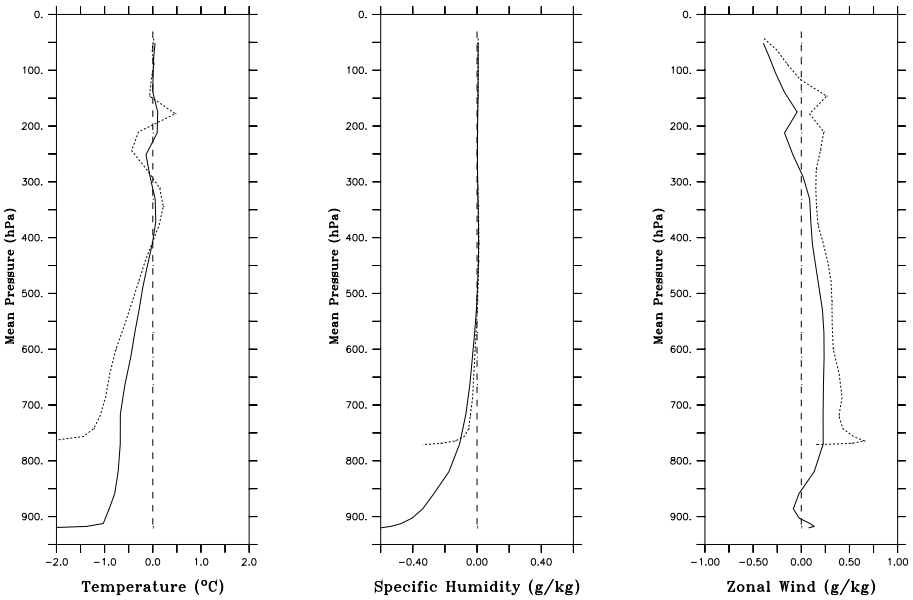

Figure 3.12 : Mean vertical profiles of temperature, specific humidity and zonal wind speed difference (MAR–ERA40) between the MAR model and the ERA-40 renalysis. The solid (resp. dotted) line gives the average over the whole domain (resp. ice sheet) excluding the model boundary zone.

In addition to the differences due to the topography (see Figure 2.6) and surface physics used by both models, the vertical profiles in Figure 3.12 illustrate also well the previously mentioned MAR biases in the SBL i.e. too cold and too dry. Both modelled zonal winds are nonetheless in excellent agreement.

3.3 Conclusion

Results from 12 months of a Greenland ice sheet simulation using the MAR model has been evaluated with GC-Net observations in 1998. The model has been found to accurately represent the evolution of the observed SBL for all seasons, but the agreement is better in summer. As the Polar MM5 model (Cassano et al., 2001), MAR is more skilful in the modelling of the surface pressure and temperature on the ice sheet than in the prediction of the specific humidity, wind and solar radiation. On average over the 13 AWS's compared, MAR is too cold and dry, overestimates the wind speed, the solar radiation and the solid precipitation. These biases are confirmed by comparison with the ERA-40 reanalysis while the differences between both models remain small in space and time except in the SBL. The conclusions of this evaluation fully agree with those of Lefebre (2002) and Lefebre et al. (2005) for previous MAR versions.

The biases in both MAR specific humidity and wind speed fields are probably consequences of the underestimated modelled temperature. A cold bias in the model implies a reduced capacity of the model atmosphere to hold water vapour and leads to a negative bias in the modelled specific humidity. Similarly, enhanced drainage flow is forced by colder near-surface air in the model since the SBL wind on the ice sheet is a primarily katabatically forced wind.

The overestimated snow height due to too heavy solid precipitation will be discussed in the next chapter and the bias in the modelled solar flux was already identified in a previous version of MAR using also the Fouquart and Bonnel (1980) formulation (Lefebre et al., 2005).

The MAR model underestimates the temperature mainly during the polar night and at the top of the ice sheet when/where the temperature is the coldest. In summer, this bias is considerably reduced by "errors compensation" because the downward solar radiation is overestimated. This error compensation allows MAR to simulate correctly the melt in summer (see Chapter 6). Therefore, it is reasonable to suppose that the cold bias weakly affects the simulated SMB except by favouring heavier snowfall in winter.

Largely overestimated incoming solar fluxes in cloudy conditions suggest errors in the simulated cloud cover and therefore, an underestimation of the modelled downward infra-red flux which is the main power supply due to the high rate of reflected solar radiation. A likely underestimated incoming long wave flux in the MAR radiative scheme was already highlighted by Lefebre et al. (2005) on the Greenland ice sheet and has been recently also identified on the Antarctic plateau by Hubert Gallée (personal communication). Comparisons with Dome C surface observations and soundings suggests indeed an underestimation of the MAR modelled downward infra-red flux on the Antarctic plateau during warm events very likely due to biases in the simulated cloud cover.

Chapter 4

Evaluation of MAR precipitation

Precipitation is the main component of the SMB equation by adding snow or liquid water to the ice sheet. Snow winter accumulation[30] also conditions the appearance of low albedo zones in summer which has an impact on the melt intensity. Mote (2003) further concludes that low ablation years are more likely associated with high winter accumulation. Hence, one needs to model precipitation as accurately as possible to be able to assess the SMB. In this chapter, we evaluate the MAR precipitation in 1990[31] against coastal weather station observations, climatologies, results from other models as well as with reanalyses. The conclusions of this comparison are the same for other years. The accuracy of the climatology-derived Greenland precipitation is also discussed and, finally, 8km-disaggregated MAR fields are presented. On the period 1978-2005, MAR shows a statistical insignificant increase of 1 km^3 per year of the total Greenland precipitation (~ 890 $km^3\ yr^{-1}$).

4.1 Data

Direct precipitation measurements are mostly collected on the coast by the Danish Meteorological Institute (DMI) weather stations. They are locally

30 Accumulation is defined as precipitation minus evaporation/sublimation. The evaporation/sublimation is evaluated to be 10% of the precipitation in average over the Greenland ice sheet (Box and Steffen, 2001).

31 The year 1990 has been chosen to perform this evaluation because we already published a similar evaluation for a previous MAR version for the year 1990 in Fettweis et al. (2005).

influenced by wind effects and snow drift during snowfall and, therefore, these observations are not really representative for the Greenland ice sheet conditions. For these reasons, their use is not sufficient to validate a model at the scale of the whole Greenland. On the other hand, the classical climatologies based on extrapolated weather station measurements are not so reliable in Greenland. Ice core measurements (see Figure 2 in Kiilsholm et al., 2003) show an accumulation of 300-500 mm/year at the top of the ice sheet in the south and along the north west of the ice sheet. In the north east, the accumulation is about 100 mm/year. None of the three climatologies plotted in Figure 4.1 shows this pattern. The climatologies compare evidently better with observations along the Greenland coast because very likely, only the DMI observations along the coast are used over the Greenland to build the climatologies.

Hence, our option is to use also other models to assess the precipitation simulated by MAR. To do so, we use the modelled precipitation from i) Bromwich et al. (2001) (noted Bro2001 here after), ii) results from the regional climate model HIRHAM4 (Dethloff et al., 2002), iii) forecasted precipitation from the ERA-40 data set and iv) precipitation from the NCEP-DOE Reanalysis 2 (Kanamitsu et., 2002). The ERA-40 precipitation is obtained from the 12-24h period of each forecast. The Bro2001 data set is available at a resolution of 50 km and is based on a statistical-dynamical and topographic forcing of precipitation (Chen et al., 1997) using the ERA-15 reanalysis data. It was successfully validated with measured accumulation from 11 ice core sites. Cassano et al. (2001) used these data to validate Polar MM5 simulations on Greenland and recently Mote (2003) estimated the Greenland ice sheet SMB using the same data set.

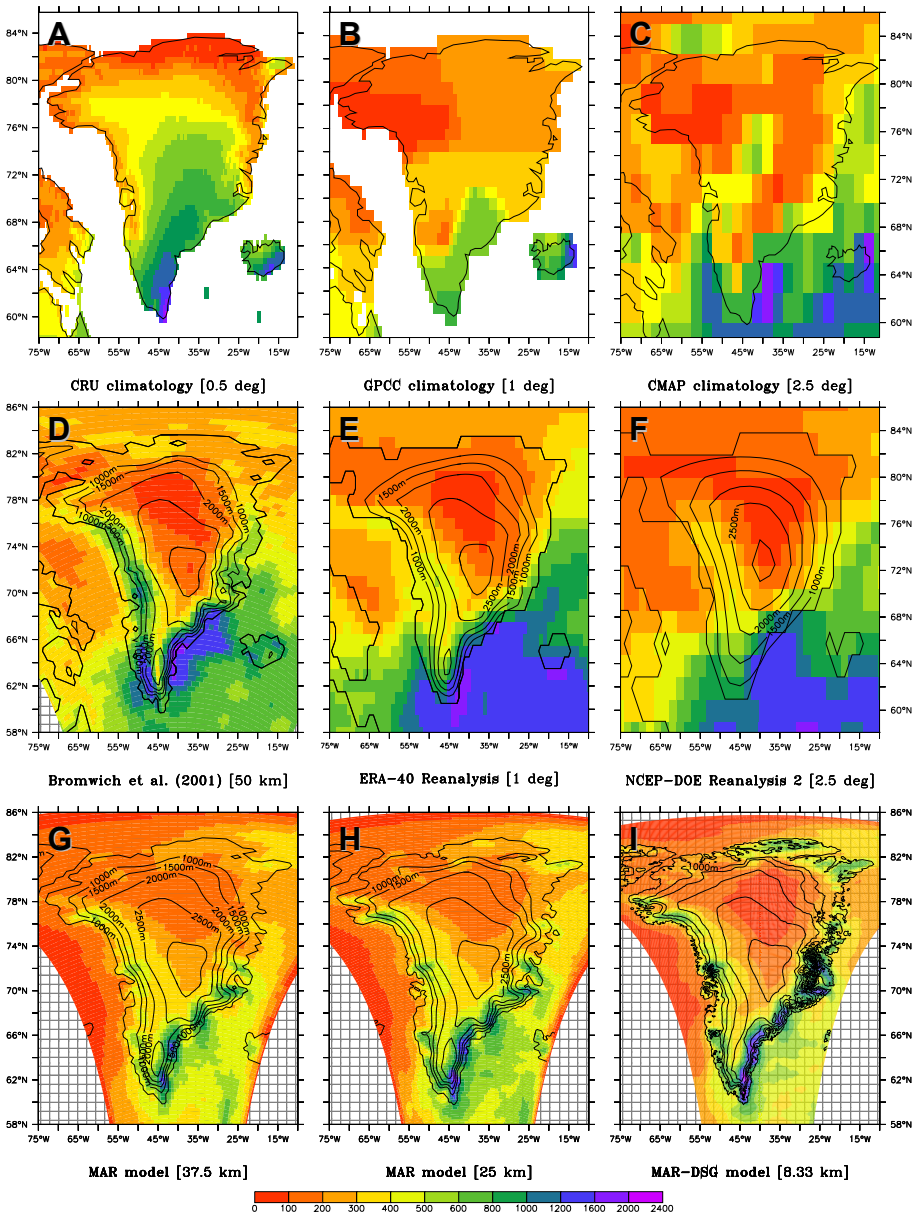

Figure 4.1 : Cumulated precipitation (mm) from January 1990 to December 1990, a) from monthly 1990 CRU climatology (New et al., 2000), b) from monthly 1990 GPCC climatology (see http://www.dwd.de), c) from monthly 1990 CMAP

climatology (Xie and Arkin, 1997), d) modelled by Bromwich et al. (2001), e) from the ERA-40 reanalysis data, f) from NCEP-DOE Reanalysis 2 (Kanamitsu et., 2002) and simulated by MAR at a resolution of g) 37.5 km, h) 25 km and i) 8.33 km via a rain disaggregator model from Sinclair (1994) forced by 25 km MAR fields. The resolution is indicated in brackets.

4.2 The 1990 MAR precipitation evaluation

4.2.1 Evaluation against coastal observations

Table 4.1 lists the cumulated total precipitation in 1990 observed and simulated by the four models cited above for 12 coastal DMI weather stations (shown in Figure 2.5). The DMI data (Cappelen et al., 2000) and the HIRHAM4 outputs are from Dethloff et al. (2002). The Bro2001 and ERA-40 values come from an interpolation on the MAR grid and are taken at the grid points closest to the stations.

All the models agree with the observations and MAR is even the closest to the observations (see the RMSE in the table). But, in view of the weather station sites, the assessment of the models ability to reproduce precipitation is limited to the Greenland coast, while the aim of these models is to study the ice sheet mass balance.

Since Fettweis et al. (2005) (noted Fet2005 hereafter), the water conservation in MAR hydrological scheme has been improved. Consequently, MAR underestimates rather now the observed precipitation on average contrary to other models and previous MAR results shown in Fet2005. Nevertheless, as we will see in the next section, these corrections allowed to improve significantly the precipitation amount modelled by MAR above the ice sheet.

Station name	**Station number**	**DMI**	**ERA40** (1° x 1°)	**MAR** (25km x 25km)	**Bro2001** (50km x 50km)	**HIRHAM4** (0.5° x 0.5°)
Pituffik	4202	46.4	323.6	205.9	352.0	**192**
Ilulissat	4216	no data	433.3	311.7	780.9	432
Aasiaat	4220	361.7	**400.9**	259.8	420.6	416
Sismiut	4230	358.1	606.7	**334.3**	361.9	344
Kangerlussuaq	4231	152.6	467.2	**305**	452.9	412
Nuuk	4250	690.2	904.6	427.6	**679.5**	936
Paamiut	4260	934.0	**1089.0**	533.2	1094.5	1435
Narsarsuaq Lufthavn	4270	794.6	1165.0	**815.8**	1059.2	1140
Qaqortoq	4272	998.5	1291.1	574.5	**1093.4**	1652
Station Nord	4312	321.5	**350.6**	428.3	233.6	800
Danmarkshavn	4320	308.9	427.9	**287.7**	373.8	612
Tasiilaq	4360	906.3	**1186.2**	521.1	1477.0	1596
	Mean:	533.9	746.6	**428.4**	690.7	866.8
	RMSE:	-	238.42	**235.72**	239.24	398.4

Table 4.1 : Total 1990 precipitation (mm) for Greenland from the Danish Meteorological Institute (Cappelen et al., 2000), ERA-40 reanalysis data, MAR simulation, Bromwich et al. (2001) and HIRHAM4 simulations (Dethloff et al., 2002). Mean precipitation and the Root Mean-Square Error (mm) between observations and modelled precipitation are also shown. The modelled results closest to observed DMI data are shown in bold.

4.2.2 Evaluation against other models

Figure 4.1 shows a good agreement between MAR, Bro2001, both ERA-40 and NCEP reanalyses and Dethloff et al. (2002) estimate (see their Figure 4), except in the Irminger Sea (south west of Iceland in the Atlantic Ocean) where MAR underestimates precipitation. But this oceanic region, near the

model boundaries, is of less interest. The underestimation of precipitation above the ocean does not come from the proximity of the integration domain boundaries but it is a known bias in the MAR model. It has also been identified in other regions like Africa or Europe (Personal communication from Emilie Vanvyve). The MAR precipitation overestimation found by Fet2005 with a previous MAR version above the ice sheet is now significantly reduced due to improvements in the hydrological scheme. The positive bias along the eastern coast and steep windward margins, found in a previous MAR simulation (Fet2005) as well as in Polar MM5 model simulations (Cassano et al. 2001) and the HIRHAM4 model (Dethloff et al. 2002), does not occur any more. The quality of the modelled ice sheet accumulation is also confirmed by the successful comparison between GC-Net observed and modelled snow height (see previous chapter). A slight precipitation-overestimation remains however mainly due to temperatures underestimated by MAR above the ice sheet. A cold bias in the model implies a reduced capacity of the model atmosphere to hold water vapour.

Precipitation occurs mainly along the western and south-eastern coast in the four models. At the southern coast of Greenland, precipitation is mainly a result of large-scale humidity transports connected with transient weather systems, enhanced by substantial orographic lifting. The minimum is found over the North Central Greenland, where it is known that the annual accumulation is smaller than 200 mm yr^{-1} (Bales et al., 2001; Dethloff et al., 2002). Precipitation maxima are found in the far south and along the eastern coast of Greenland in the MAR model, in both ERA-40 and NCEP reanalyses, in CRU (New et al., 2000) and GPCC 1990-climatologies, and in the Dethloff et al. (2002) estimates (see their Figure 4). Bromwich et al. (2001) simulate two precipitation maxima along south western and south-eastern coasts, and comparatively little precipitation in the far south of

Greenland. The local minimum of precipitation simulated by MAR in southern Greenland near Narsarsuaq (for a map, see Figure 2.5) is also present in the Dethloff et al. (2002) estimate (their Figure 4). The location of the MAR maxima agrees very well with that of the others models (particularly the ERA-40 reanalysis).

4.2.3 37.5 km MAR results

In addition to the 25 km reference simulation, a simulation with a spatial resolution of 37.5 km (= 3/2 * 25 km) was performed to study the influence of a higher resolution on the SMB simulation. This simulation has the same integration domain and model schemes as the 25km-simulation. Both simulations are in complete agreement. The precipitation patterns are the same. The amount is higher in the 25km-simulation in the mountainous regions due to a finer/higher topography. A finer resolution increases the "topographic barrier effect", which modifies the horizontal flow, and contributes to raise air masses and to produce condensation and thus precipitation during their forced ascent (Brasseur et al. 2001).

4.2.4 8.3 km disaggregated MAR results

A Rain Disaggregator Model (RDM), originally developed by Olivier Brasseur (Brasseur et al., 2001) by using the Sinclair (1994) formulation, was used to downscale the 25km MAR precipitation to a resolution of 8.33 km (= 25 km / 3).

The Sinclair's model (1994) predicts precipitation rate as a function of the vertical wind induced by the local topography and large scale wind speed, temperature and specific humidity. The name of the model (called VDEL) represents the model's fundamental assumption: vertical motion at the

surface ω_s can be approximated by the dot product of surface wind field and the local terrain gradient:

$$\omega_s \approx -\rho g \vec{V}_s \cdot \vec{\nabla} z_s$$

This vertical motion induced by the local topography propagates vertically and drives orographic precipitation. Sinclair adds the synoptic vertical motion to accurately estimate the decay of ω_s with height. The vertical velocity $\omega(p)$ at pressure height p above the surface is then parametrised as:

$$\omega(p) = \omega_{MAR}(p) + \omega_t(p)$$

where $\omega_{MAR}(p)$ is the synoptic scale vertical motion (simulated by MAR) and the $\omega_t(p)$ is the terrain-induced vertical motion. $\omega_t(p)$ is parameterized as some fraction of the initial vertical motion at the surface ω_s.

The instantaneous rate of precipitation R at the ground is estimated

$$R = \frac{\lambda_s}{g} \int_0^{LCL} \delta(p) \lambda(p) F(p) \omega(p) dp$$

by integration through a vertical column from the lifting condensation level (*LCL*) to the top of the atmosphere, the availability of moisture $\lambda(p)$ aloft, the rainfall efficiency F(p) and the vertical velocity $\omega(p)$ computed as above. λ_s is the availability of moisture at the surface and $\delta(p)$ is a On/Off switch based on direction of vertical wind (it takes a value of 1 if the vertical motion is directed upwards). $\lambda(p)$ and λ_s are heuristic relations that map the relative humidity to factors that vary between 0 and 1 to reflect the influence of relative humidity on precipitation rates. $F(p)$ is an efficiency factor derived

from the thermodynamic energy equation to provide the rate at which water condenses as a function of temperature and specific humidity. See Sinclair (1994) for more details about these variables.

Funk and Michaelsen (2004) found that the original Sinclair's formulation overpredicts precipitation amounts by comparison with a set of gauge observations in the United States and improved the Sinclair's model. Following them, we extended the VDEL model

1. by using internal gravity wave-based heuristics to replace the decay function of Sinclair with a deterministic function of $\omega_i(p)$;
2. by treating orographic rainfall as an addition of existing meso-scale precipitation patterns, rather than as an independent process. The disaggregator only rains (resp. snows) when the MAR model is raining (resp. snowing);
3. by incorporating cloud cover data into our model. The predicted intensities of the VDEL model are reduced by the fraction of cloud cover.

The last two improvements do not change significantly the outputs of the RDM in Greenland but the first one, based on atmospheric buoyancy to determine an alternative decay function for $\omega_i(p)$, improves the results and corrects well the overestimated precipitation amounts by the original Sinclair's model.

The 25 km MAR results and 8.3 km disaggregated fields compare very well in Figure 4.1. On average, we have less precipitation above the ice sheet and more on the coastal mountainous ranges with the RDM. The RDM is above all sensitive to unevennesses in the topography given the formulation of its precipitation rate. That is why we have less precipitation above the sea and above the dome of the ice sheet. However, the agreement is very good with the MAR 25km-precipitation and it should be interesting to couple the

RDM with SISVAT to produce the SMB at lower resolution and at a low computational cost from the 25km MAR fields.

4.3 The 1978-2005 MAR and ECMWF precipitation

To conclude this chapter, the mean 1978-2005 precipitation simulated by MAR and ECMWF (re)analysis are compared in Figures 4.2, 4.3 and Table 4.2. The 1° ECMWF forecast precipitation is interpolated on the 25 km MAR grid and averaged on the Greenland MAR mask.

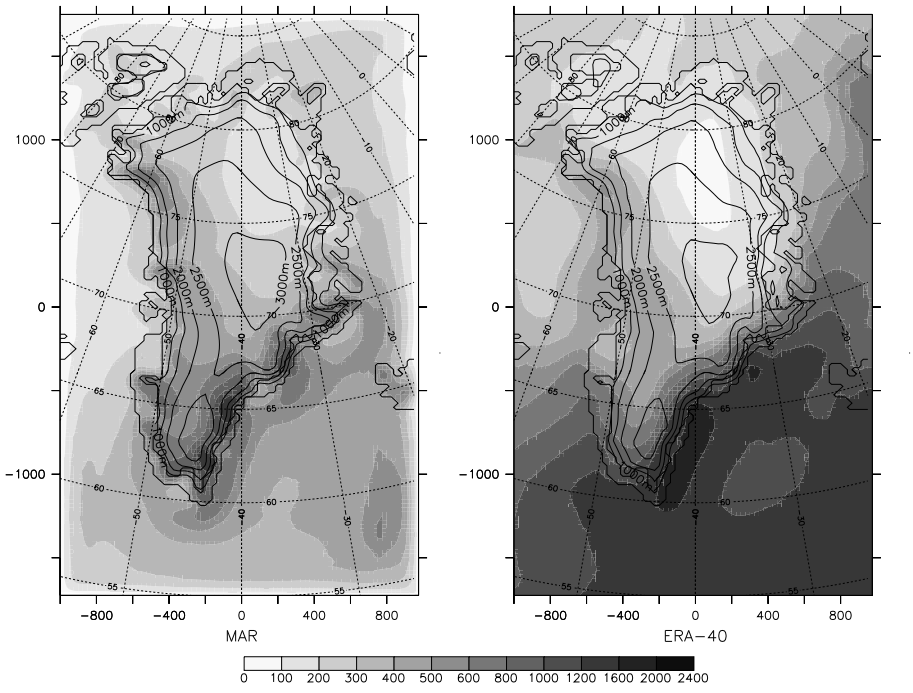

Figure 4.2 : annual mean total precipitation (solid + liquid) simulated by MAR (left) and from ERA-40 (right) over the 1978-2005 period.

As for 1990, MAR agrees well with ERA-40 on the ice sheet but simulates less precipitation along the south-eastern coast and in the Irminger Sea than ERA-40. The agreement with the 1988-2004 averaged estimates from the

Polar MM5 model (Figure 5 of Box et al., 2006) is also very good. On average on the ice sheet, MAR simulates more precipitation than ERA-40 whereas both models are in good agreement on the whole Greenland. The repartition solid/liquid precipitation is not the same between both models but the resolution and the topography (which is higher in MAR along the coast) are very different (see Figure 2.7). Both models show a statistical[32] insignificant precipitation increase of 1.4 to 4.2 ± 9 $km^3\ yr^{-1}$ per year from 1978 to 2005. However, operational ECMWF forecast precipitation is used after August 2002 and part of interannual variability in ECMWF fields results from changes in the operational model. Therefore, the correlation with MAR precipitation is better (0.65) if the comparison is restricted to 1978-2001 versus 1978-2005 (0.48).

	Mean ($km^3\ yr^{-1}$)		***Trend ($km^3\ yr^{-2}$)***	
	MAR	ERA-40	MAR	ERA-40
Total Precipitation (Greenland)	**892**	**887**	**1.4 ± 8.8**	**4.2 ± 9.6**
Total Precipitation (only Ice sheet)	678	608	1.5 ± 6.4	2.5 ± 6.6
Snowfall (Greenland)	803	681	0.6 ± 8.2	1.5 ± 6.9
Snowfall (only Ice sheet)	640	505	1.1 ± 6.1	1.2 ± 5.3
Rainfall (Greenland)	88	205	0.8 ± 1.5	2.7 ± 4.2
Rainfall (Ice Sheet)	39	102	0.5 ± 0.8	1.2 ± 2.0

Table 4.2 : Statistics for both MAR and ERA-40 models over the 1978-2005 period.

32 The significance has been tested using a Monte-Carlo method with 1,000,000 simulations of autocorrelated data series with the same autocorrelation as the precipitation time series. The error bar in the trend is the division of the standard deviation of the precipitation temporal series by the number of years (i.e. 28).

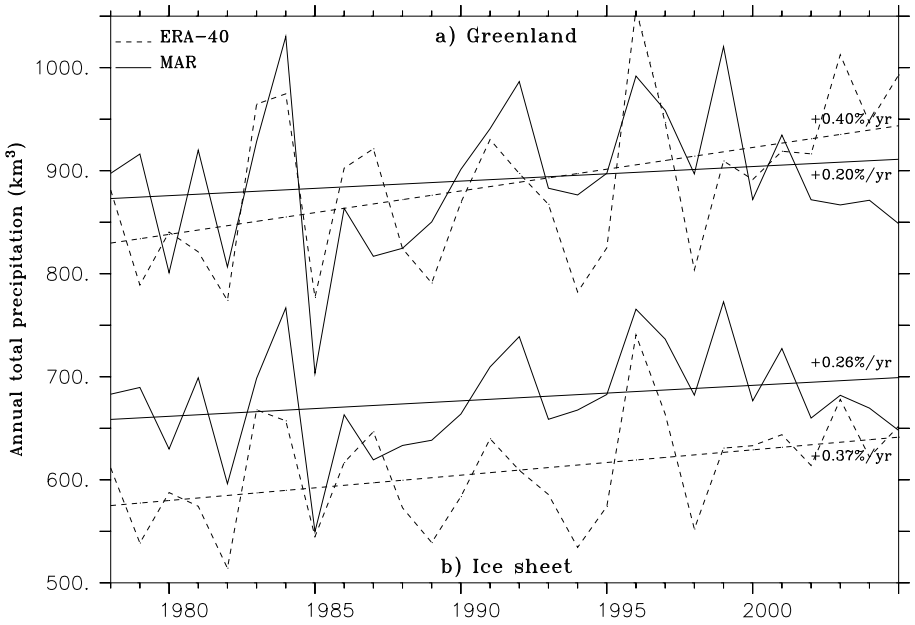

Figure 4.3 : Evolution of the annual total precipitation over Greenland (resp. the ice sheet) in km³ simulated by MAR (solid) and ERA-40 (dashed).

4.4 Conclusion

The MAR precipitation agrees well with measurements, results from other models, and reanalyses on Greenland. The good agreement between MAR simulations at a spatial resolution of 25 km, 37.5 km, and 8.3 km via a RDM shows the coherence in the simulation of precipitation with MAR model. It would be interesting to couple the RDM with SISVAT to produce the SMB at lower resolution and at a low computational cost from the 25 km MAR fields.

Chapter 5

The surface albedo using satellite data and MAR output

As the surface albedo depends on the nature of the snow, its grain size, its water content and its thickness, the albedo is an excellent indicator of the snow pack properties. In addition, it is one of the most critical parameters of the surface energy balance equation since part of the energy needed for melting is supplied by solar radiation. So far only the surface albedo from some weather stations on the ice sheet has been used to validate a model (Bugnion and Stone, 2002; Lefebre et al., 2005)). We compare here the modelled surface albedo with the surface albedo derived from the AVHRR Polar Pathfinder (APP) data set (Fowler et al., 2000). This is based on the Advanced Very High Resolution Radiometer (AVHRR) flown on the U.S. National Oceanic and Atmospheric Administration (NOAA) operational meteorological satellites. However, the latter are only valid in clear-sky cases, which limits the comparison. Part of this chapter is published in Fettweis et al. (2005) (referred to as Fet2005 hereafter).

5.1 The AVHRR-derived surface albedo

5.1.1 Data

We use here the AVHRR Polar Pathfinder Twice-Daily 5 km Equal Area Scalable Earth-Grid Composites product (Fowler et al., 2000) available from the National Snow and Ice Data Center (NSIDC). This data set includes channel reflectances (channels 1 and 2 in visible and near-infra-red), brightness temperatures (channels 3-5 in infra-red), clear sky surface temperature and albedo, solar zenith angle, satellite elevation angle, Sun-satellite relative azimuth angle, cloud and surface mask, and time information. These products are available twice a day (approximately 0400 UTC and 1400 UTC) at 5 km resolution on a global area coverage (GAC) for the period July 1981 through December 2000. They are fitted to the Equal Area Scalable Earth-Grid (EASE-grid) (Armstrong and Brodzik, 1995). This data set is used in Stroeve (2001) to study the albedo variability of the Greenland ice sheet from 1981 to 1998.

5.1.2 Methodology

The methodology used by the APP product team to derive the surface temperature, albedo, and cloud masking is based on the Cloud and Surface Parameter Retrieval (CASPR) system (Key, 1999; Key et al., 2001). In brief, the retrieval of the clear-sky surface albedo involves the following four steps:

- normalization of the AVHRR channels 1 and 2 with respect to the solar zenith angle;
- conversion of the calibrated channel 1 and 2 reflectances to a top-of-the-atmosphere (TOA) broadband reflectance;

- correction of the dependence of the Sun-satellite-surface geometry on the TOA broadband reflectance, using an anisotropy factor;
- conversion of the TOA broadband reflectance to a surface broadband albedo, using a linear relationship.

For more detailed information on the derivation of the surface albedo, we refer to Key (1999), Stroeve et al. (2000) and Stroeve (2001). See also Fowler et al. (2000).

In contrast to microwave data, the current algorithm for the retrieval of the surface albedo is only valid during clear-sky periods. This makes the cloud detection critical. Clouds over Greenland are particularly hard to detect in the infra-red part of the spectrum because their temperature is often similar to that of the surface. Three cloud masks using a combination of time series analysis and multichannel threshold tests are provided in the 5 km APP products. One is based on multichannel and multiday techniques in the CASPR algorithms. Another is obtained by using a long time series of channel 4. A third is a modified method of replacing the channel 4 statistic required in the CASPR algorithm using the channel 4 series from the second method. These three methods are described in detail in Stroeve (2001).

Following the recommendations of Stroeve (2001), the second cloud mask (based on a temporal thermal filter) is used here to detect clouds. The other two cloud masks tend to overestimate clouds over Greenland (Stroeve, 2001). However, the cloud detection remains imperfect and an albedo filter is applied to discard grid points with too low an albedo or an albedo greater than 1.0. We consider that the minimum albedo is 0.15 in the tundra area, 0.3 in the ablation zone, 0.6 in the percolation zone and 0.7 in the dry snow zone. The albedo of dry snow varies generally between 0.8 and 0.9 (Wiscombe and Warren, 1980), the wet snow albedo between 0.6 and 0.8 and the bare ice albedo between 0.3 and 0.55 (depending on the liquid water

present at the surface). The APP surface albedo is interpolated on the 25 km MAR grid for a better comparison with MAR results and the gaps due to the presence of clouds are filled by interpolation. The daily MAR albedo is defined as the ratio of the daily total short-wave reflected radiation and global radiation. It is clear that the i) cloud detection, ii) the estimate of APP parameters at extreme viewing angle and iii) the interpolation of clear skies to cloudy areas can result in a large source of uncertainty in the current estimates of surface albedo using AVHRR data.

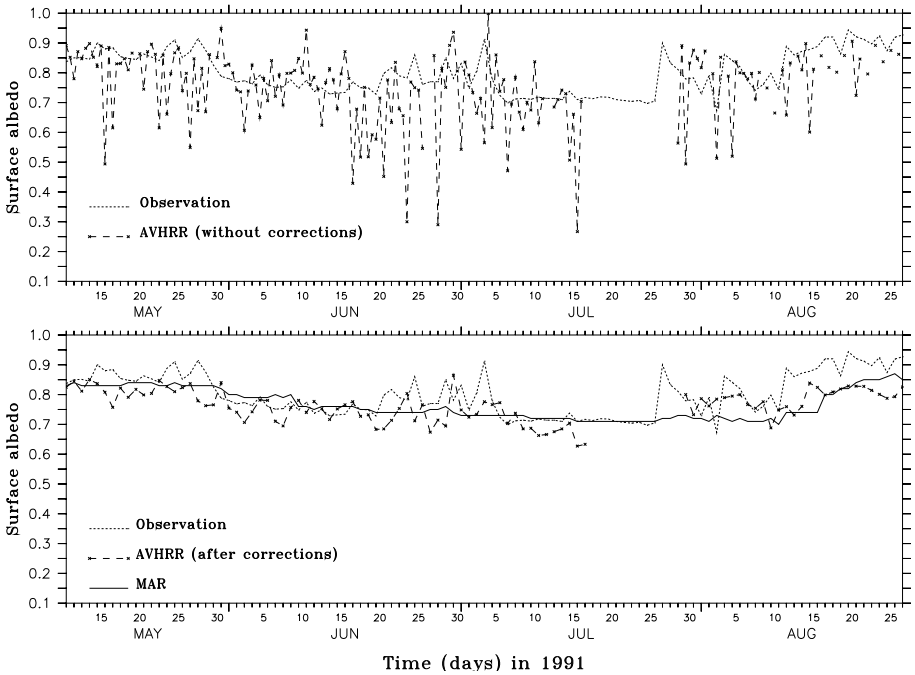

Figure 5.1 : Top: Observed (dotted) and AVHRR (dashed) surface albedo at ETH-Camp in 1991 (Ohmura et al., 1992); no corrections have been applied to AVHRR product (Fowler et al., 2000). Below: The surface albedo at ETH-Camp simulated by MAR (solid), observed (dotted) and derived from AVHRR data (dashed) after interpolation on the MAR grid, removal of cloud contaminated grid points and corrections for unrealistic values.

The surface albedo observed at ETH-Camp in 1991 (Ohmura et al., 1992), derived from APP products and simulated by MAR is shown in Figure 5.1. Small-scale oscillations in the AVHRR albedo are a known artifact in the APP products (Stroeve, 2001). The comparison between the two plots shown in Figure 5.1 supports our interpolation method of APP products to the MAR grid. Figure 5.1b also confirms the ability for MAR to simulate the surface albedo at ETH-Camp (see also Lefebre et al., 2005).

5.2 MAR albedo evaluation in summer 1998

By continuity with the MAR vs GC-Net observations comparison (see Chapter 3), the summer of 1998 was also chosen to evaluate the MAR albedo. In addition, similar results are shown in Fet2005 for 1990 and 1991. In Figures 5.2, 5.3, 5.4 and 5.5 are plotted the time evolutions of the surface albedo averaged in 1998 over the four zones shown in Figure 2.5: a) the ablation zone, b) the percolation zone, c) the dry snow zone, and d) the tundra.

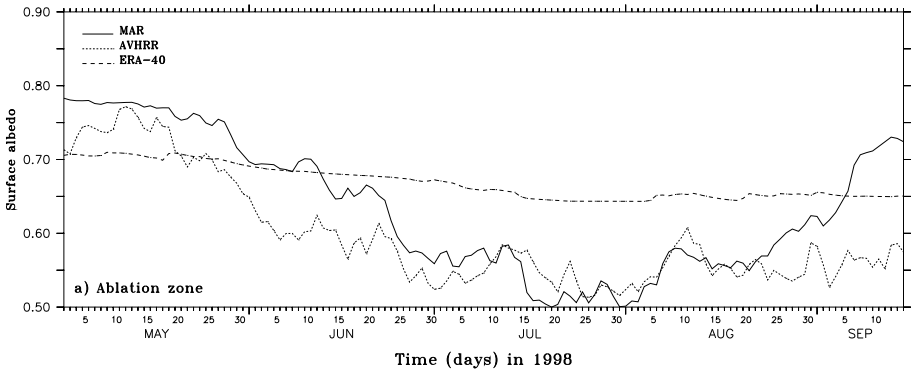

Figure 5.2 : Time evolution in 1998 of the surface albedo averaged on the ablation zone (as defined in Figure 2.5) simulated by MAR (solid), derived from the APP products (Fowler et al., 2000) (dotted) and from the ERA-40 reanalysis data (dashed).

a) The surface melt starts at the end of May in the ablation zone in 1998. The sharp transition from a dry snow pack in May to a wet snow pack in June is clearly visible in Figure 5.2. The albedo variations in June are associated with snowfall that temporarily raises the snow albedo. Bare ice (albedo lower than 0.55) begins to appear from the end of June and the albedo continues to decrease to reach a minimum value in mid-July, when the snow pack has melted away in many places. Two snowfall events found in both AVHRR and MAR fields at the end of July temporarily increase the mean ablation zone albedo. At the beginning of 1998 September, the melt season is over as shown by the SSM/I-derived data (see chapter 4) and fresh snow begins to cover the bare ice. The albedo increases then to reach the typical value of dry snow in mid-September. The AVHRR albedo don't show this increase at the end of the melt season, likely due to cloud contamination. As a result the satellite-derived snow albedo is underestimated. In addition, the Sun is already very low in the sky in September which decreases the CASPR albedo algorithm accuracy (Fowler et al., 2000). Finally, MAR mostly overestimates the albedo compared to the one derived from satellite, but Stroeve et al. (2000) mention that the APP albedo values are on average 10% less than those measured by AWS stations and this for period from January 1997 to August 1998. This bias can be reduced to 6 % considering that the ground-based measurements are also biased.

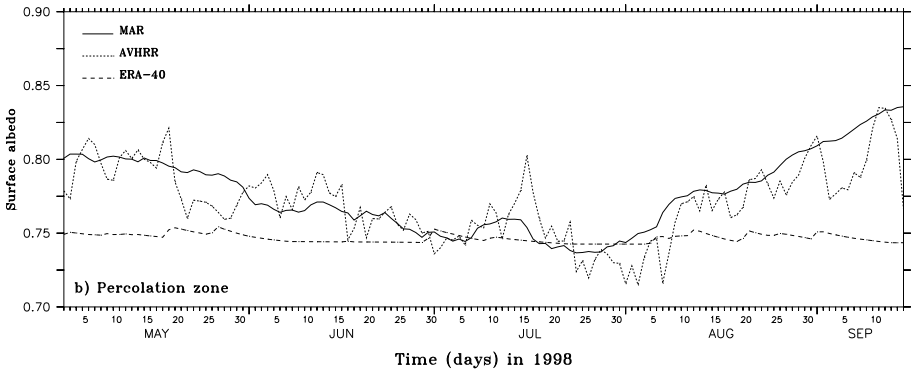

Figure 5.3 : Same as Figure 5.2 but for the percolation zone.

b) In the percolation zone (Figure 5.3), there is a small albedo decrease associated with the moistening of the snow pack in June and July. But no bare ice appears and the albedo remains above 0.7. From the beginning of August, fresh dendritic snow covers gradually the ice sheet.

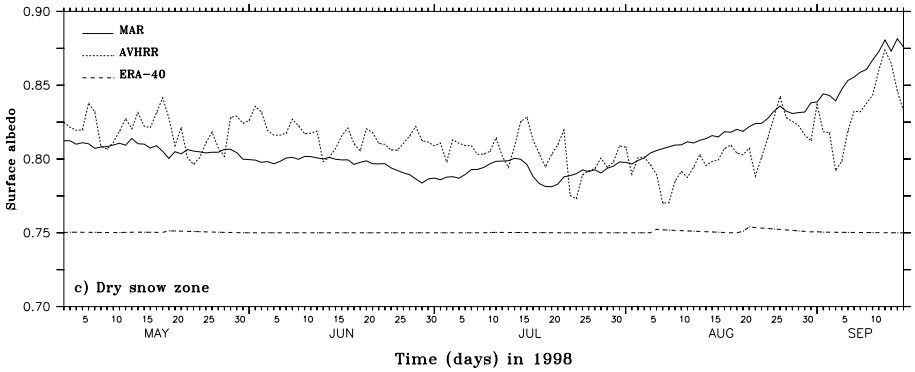

Figure 5.4 : Same as Figure 5.2 but for the dry snow zone.

c) The snow pack remains dry in the dry snow zone (Figure 5.4) and therefore no significant variations are observed. The very small variations in AVHRR albedo are most likely due to cloud contamination. For example, stratospheric clouds (di Sarra et al., 2002) are abundant over the Greenland ice sheet summit but are not detected by the CASPR algorithm.

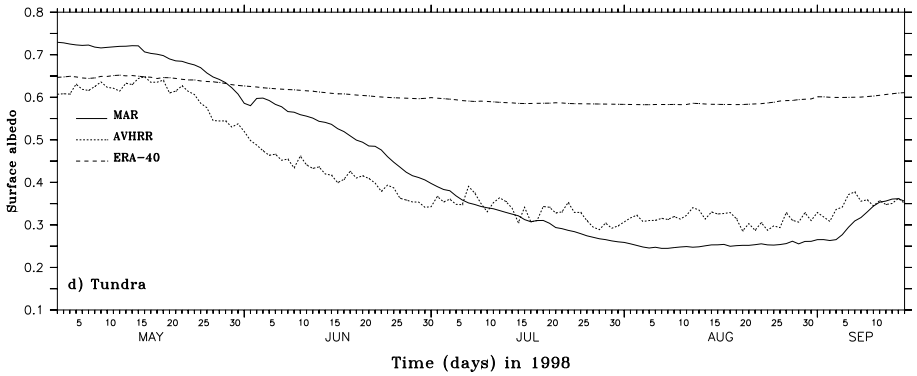

Figure 5.5 : Same as Figure 5.2 but for the tundra.

d) The albedo evolution in the tundra area (Figure 5.5) is similar to that in the ablation zone with dry snow that becomes wet snow at the end of spring. A grass surface appears in August once all snow has melted away. A wet snow pack covers the soil again at the end of summer. MAR overestimates (underestimates) the albedo in May and June (in August and September). Besides a possible overestimated accumulated MAR snow pack at the end of the winter, very few corrections are applied to the satellite-derived albedo in the tundra (albedo minimum = 0.15). It is likely that errors in the cloud mask significantly bias the APP fields in this often cloudy region located near the coast. These errors lower the derived albedo when the soil is covered by snow and raise it when all the snow has melted away on the grass. The cloud contaminated albedo varies generally between 0.3 and 0.7 and is therefore higher than the grass albedo (0.15) and lower than the snow albedo (0.6-0.8).

Figures 5.2-5.7 show also the albedo from the ERA-40 reanalysis data. It is obtained from the 12-24h period of each forecast and is interpolated on the 25 km MAR grid to be afterwards averaged on the Greenland MAR mask. The ECMWF albedo does not vary a lot in time during the melt season and in space between the four previous mentioned SMB zones. Furthermore, it is in worst cases in total disagreement with both MAR and AVHRR albedo. On

the one hand, the nearly constant nature of the ERA-40 albedo in time illustrates the poor representation of the polar processes on the ice sheet surface in the ECMWF model. On the other hand, the very weak differences between the four cited zones show the limits of a coarse resolution (~100 km) as used in the ERA-40 reanalysis data. At this resolution, it is almost impossible to resolve accurately some zones not wider than 100 km as the tundra or the ablation zone in Greenland. The ERA-40 reanalysis only exhibits low albedo zones along the southern Greenland coast (see Figure 5.6). The rest of the Greenland is represented as an ice sheet with an almost time-constant albedo.

In Figure 5.6, the albedo evolution is plotted through the four summer months in 1998, i.e. (i) the transition from dry snow albedo to wet snow albedo first in the tundra and often in the ablation zone (May) and later in the percolation zone (June), (ii) the drop in the albedo due to the completely melted snow pack above the soil in the tundra and the ice in the ablation zone (July), iii) the progressive increase of the albedo at the summer end (August) because of new snowfalls. As explained earlier, MAR overestimates albedo on the tundra when compared to the AVHRR estimates. We show here the comparison in summer 1998 because it is the summer studied in Chapter 3 but similar plots/analyses for summers 1990-1991 can be found in Fet2005.

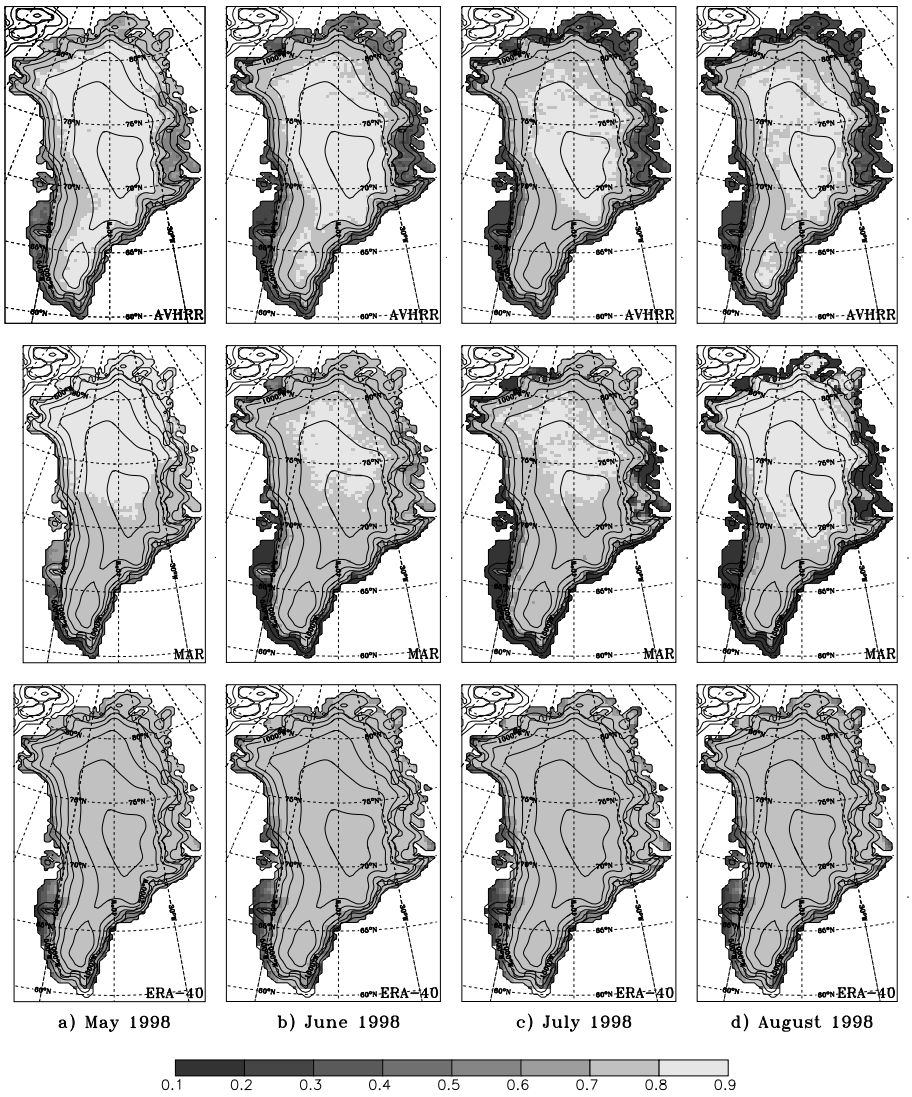

Figure 5.6 : Monthly mean surface albedo for May, June, July and August 1998, from the AVHRR remote sensing observations (top), simulated by MAR (middle) and from the ERA-40 reanalysis data (below). AVHRR values correspond to an average of available grid points after application of the cloud mask.

5.3 Conclusion

The comparison with AVHRR data enabled the validation over the whole ice sheet of (i) the modelled surface albedo, (ii) the snow pack evolution and (iii) the snow accumulation simulated by MAR. If the simulated snow pack height is too high at the beginning of the summer, this delays the appearance of low albedo zones, such as grass in the tundra, and bare ice in the ablation zone, which has an impact on the SMB. MAR snow pack evolution agrees generally with the AVHRR data. The satellite-derived albedo remains probably still too contaminated by clouds over the tundra despite the cloud mask. The cloud detection, correction and interpolation in the AVHRR data remain unfortunately a large source of errors in this comparison. Moreover, in spring and autumn, the Sun is low in the sky which reduces the CASPR albedo algorithm accuracy (Fowler et al., 2000).

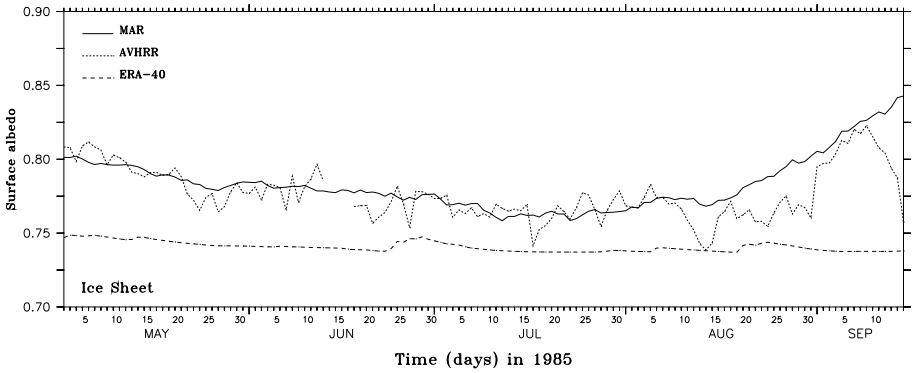

Figure 5.7 : Time evolution in 1985 of the surface albedo averaged over the ice sheet simulated by MAR (solid), derived from the APP products (Fowler et al., 2000) (dotted) and from the ERA-40 reanalysis data (dashed).

The bias in the AVHRR data due to a low solar zenith angle is particularly visible at the end of the summer of 1985 in Figure 5.7 when the AVHRR

albedo decreases surprisingly in mid-September while the MAR albedo reaches values typical of the dry snow.

Furthermore, an evaluation of the albedo from the ERA-40 reanalysis data has been performed. The ERA-40 albedo compares very badly with both MAR and AVHRR derived albedo. This illustrates the poor representation of the surface polar processes in the ECMWF model and the difficulty to accurately resolve some zones not wider than 100 km, such as the tundra or the ablation zone in Greenland, at a resolution of one degree.

Chapter 6

The modelled and microwave satellite-retrieved melt extent

Melt extent can easily be retrieved from the satellite microwave brightness temperature and is an excellent indicator to evaluate the surface mass balance simulated by MAR. The first evaluation of MAR results with passive microwave satellite-derived melt extent was made by Lefebre (2002) over the South of Greenland for summer 1991. Here, we extend this comparison to the whole simulated period and the whole ice sheet. The simulated extent and the time evolution of the wet snow zone compare generally well with the satellite-derived data. Nevertheless, measurements from ETH-Camp, from JAR-1 AWS (West Greenland) as well as MAR outputs allowed us to highlight flaws in the cross-polarized gradient ratio (XPGR) technique used to identify melt from the passive microwave satellite data. It was found that dense clouds (causing notably rainfall) on the ice sheet severely perturb the XPGR melt signal. We adapted the original XPGR melt detection algorithm to better incorporate the atmospheric variability over the ice sheet and an updated melt trend for the 1979-2004 period was calculated. The agreement with the model is then clearly better. Compared to the original algorithm, the melt zone area increase is doubled from 0.78 to 1.69 % yr^{-1}. The increase is higher and becomes significant if we use the

improved XPGR technique because the rainfall also increased during this period. This is correlated to higher atmospheric temperatures. Finally, the model shows a very high correlation between the simulated total ice sheet run-off and the melt extent area detected by the satellites. Part of this chapter is published in Fettweis et al. (2005, 2006).

6.1 Passive microwave melt signal

Liquid water forms in the snow pack when the snow melts. It changes dramatically the snow microwave emissions to approach the black body behaviour (Ulaby and Stiles, 1980). This change in the emission characteristics appears clearly in the satellite microwave data. Algorithms can then derive very effectively the melt extent over the ice sheet (Mote et al., 1993; Mote and Anderson, 1995; Abdalati and Steffen, 1995 and 1997). In contrast to visible remote sensing, the microwave remote sensing offers the advantage of not being strongly affected by clouds, cloud shadows, haze and ground fog as well as the extended polar night when the visible image collections are unavailable.

6.1.1 Data

The brightness temperatures used for the remote sensing melt monitoring come respectively from the Scanning Multichannel Microwave Radiometer (SMMR) satellite (1979-1987), the Special Sensor Microwave/Imager (SSM/I) F-8 satellite (1987-1991), the SSM/I F-11 satellite (1992-1994) and the SSM/I F-13 satellite (1995-2004). These data are provided by the National Snow and Ice Data Center (NSIDC, Boulder, Colorado). They are arranged on a regular grid of 25 km x 25 km and are available twice a day (Armstrong et al., 1994). Before interpolating these data to the model grid, we averaged the two satellite passages per day as in Abdalati and Steffen

(1997 and 2001) (referred to as AS1997 and AS2001, respectively). If the gaps were shorter than three days, missing data have been corrected through linear interpolation in time as in Torinesi et al. (2003).

6.1.2 Methodology

The approach of AS1997 is used here to deduce the melt extent over the ice sheet from the satellite data. This technique has been developed for the Greenland ice sheet by comparison with in-situ observations in the snow pack. It uses multiple frequencies and polarizations to take advantage of their differing responses to the Liquid Water Content (LWC) increase inside the snow pack. When this method detects melt, it gives the LWC of the snow pack which is very useful to compare with a model. Another algorithm has recently been developed by Torinesi et al. (2003) using only the 19-Ghz horizontal polarized brightness temperature. But i) this technique has been calibrated/validated only in Antarctica, ii) it detects mainly the surface melt and not the massive melt (i.e. the melt water deeper in the snow pack) as observed in Greenland and iii) it does not give the LWC equivalent of the snow pack. For these reasons, we will use the AS1997 retrieval melt algorithm.

The AS1997 method is based on the cross-polarized gradient ratio (XPGR), which is defined as the normalized difference between the 19-GHz horizontal polarized brightness temperature (T19H) and the 37-GHz vertical polarized brightness temperature (T37V):

$$XPGR = \frac{T_b(19\mathrm{H}) - T_b(37\mathrm{V})}{T_b(19\mathrm{H}) + T_b(37\mathrm{V})}$$

where T_b is the brightness temperature, which is defined as the product of the physical surface temperature and the microwave emissivity. A XPGR

threshold value is then used to distinguish melt from non-melt points. The threshold values were determined by comparing XPGR to the LWC of the snow pack at ETH-Camp (Greenland) in 1990, 1991, 1992 and 1994, and by intercalibration between the different satellite data sets. The XPGR threshold was determined by AS2001 to be -0.0265 for SMMR date, -0.0158 for both SSM/I F-8 and F-11 satellites and -0.0154 for the SSM/I F-13 data. The SSM/I F-11 brightness temperatures need to be intercalibrated to the F-8 baseline before using these thresholds (AS2001). When XPGR detects melt, it corresponds approximately to a LWC of 1 % by volume in the top metre of snow (AS1997). We use this last criterion to distinguish melt in the MAR simulation.

Observations of the Greenland ice sheet are made near local noon and midnight by the SMMR. The SSM/I satellites flew over the Greenland ice sheet early morning at about 0600 LT on descent and late afternoon at about 1800 LT on ascent when the melt is maximum. A daily average XPGR value was calculated from those two signals before processing the data. Therefore, the daily SSM/I-derived melt signal could result in an overestimation of the melt region considering that the (after)noon melt can mask the night-time refreezing. This is an issue especially at the beginning and at the end of the melt season when the melt period may last only a few hours during the mid to late afternoon.

To compare the model results with the satellite-derived melt area, the daily average modelled LWC of the top metre of snow is used instead of the surface temperature. The surface temperature variable is often used to detect the modelled melt area. But, preliminary analysis of MAR output showed that the use of this variable would lead to an unrealistic determination of the simulated melt area compared to XPGR, because this algorithm is sensitive to both surface and sub-surface melt water. At the beginning of the ablation

season, the surface temperature is a good indicator because the melt water is mainly situated at the surface. But, in late summer, a cold front or a clear night can refreeze the surface while the subsurface remains wet, which is classified as wet by XPGR until the snow is frozen at greater depths. According to AS1997, we use a mean LWC of 1 % by volume as a threshold value to distinguish melt from non-melt points in the simulation. The bare ice (i.e. when the winter snow pack has completely melted and the ice appears) in the ablation zone is assumed to be melting in the model.

6.2 Comparison between MAR and satellite-derived melt extent

6.2.1 Perturbations in the XPGR melt signal

6.2.1.1 The summer 1983

In 1983[33], the melt season began mid-June and ended at the beginning of September with a maximum in mid-July. The timing and amplitude of the simulated melt compare generally well with the SMMR satellite-derived melt except at the end of June, July 6-7th, July 12-14th, July 19th, August 1-2th and August 14-16th when the satellite-derived melt signal is extremely low compared to MAR. During these events, rainfall on the ice sheet is simulated by MAR (grey bar in Figure 6.1a). If we remove grid points with MAR daily liquid precipitation greater than 1 mm/day, the MAR and SMMR melt extents are more consistent. This suggests that rainfall on the ice sheet

33 The years 1983 and 1995 has been chosen to perform this comparison to have one year by data set (SMMR and SSM/I) as well as because the rainfall-resulted biases in the satellite-retrieved melt are particularly obvious during these two summers.

could bias the microwave melt signal detected by XPGR. To uphold this hypothesis, we will analyse in more details July 11-13th of 1995.

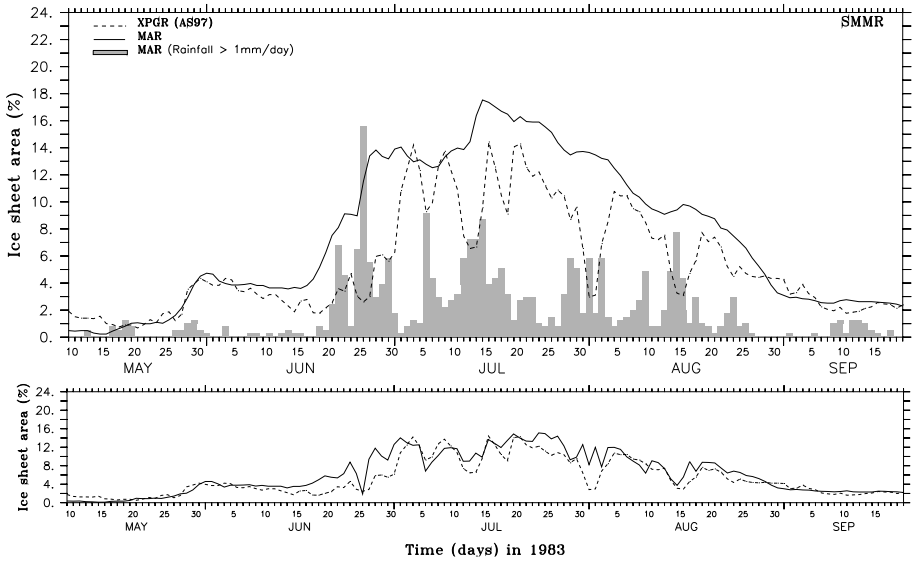

Figure 6.1 : a) Comparison between the MAR simulation (solid line) and the SMMR satellite-derived observations (dashed line) of the daily averaged melt extent zone in 1983. Melt is expressed in percentage of the Greenland ice sheet area. Also shown is the percentage of Greenland ice sheet area where MAR simulates daily rainfall greater than 1 mm/day (grey bars). b) The same as a), except that all the grid points with MAR daily liquid precipitation greater than 1 mm/day are removed in average computation of both MAR and SMMR fields melt extent. The same plot for 1990 and 1991 is shown in Fettweis et al. (2005).

6.2.1.2 July 11-13th 1995

As for SMMR-derived data, the comparison is good between MAR and SSM/I-derived melt except during rainfall events. This disagreement between the model and the satellite-derived observations is particularly obvious around July 11-13th of 1995 when the XPGR algorithm detects very few melt compared to MAR.

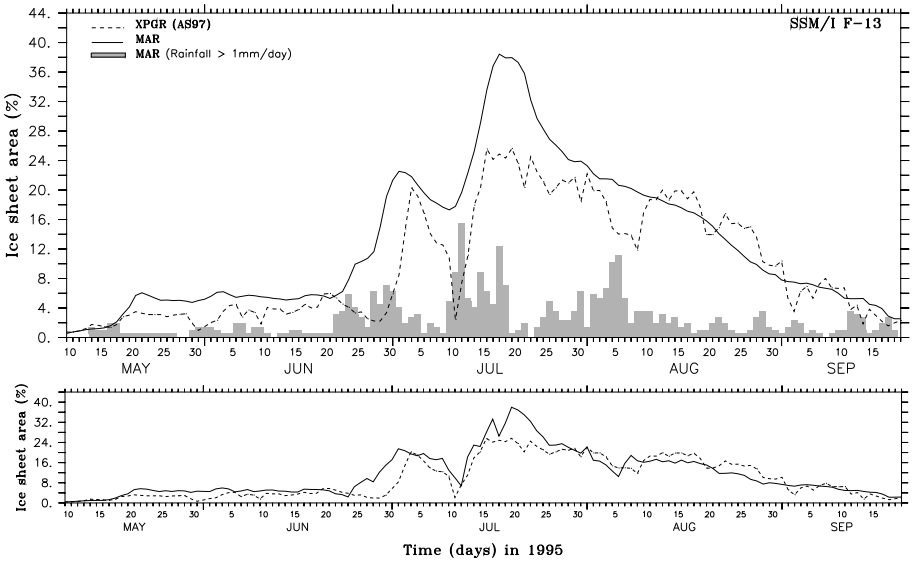

Figure 6.2 : Same as Figure 6.1 but for 1995.

During this episode, a low pressure in Labrador Sea advects wet and warm air from the south along the Greenland western coast (see Figure 6.3). This type of circulation, called barrier-type flow, increases the ablation on the ice sheet (Van den Broeke and Gallée, 1996) and is notably responsible of rainfall on the ice sheet.

The SSM/I-derived melt patterns do not show melt along the western ice sheet margin during these three days but XPGR surprisingly detects melt higher in the western melt zone (see Figure 6.4). Moreover, melt is observed in the low western melt zone just before and after this period (Figure 6.4). Finally, the zones in which XPGR should logically detect melt correspond very well in Figure 6.4 with zones where MAR detects melt and simulates liquid precipitation higher than 1 mm/day.

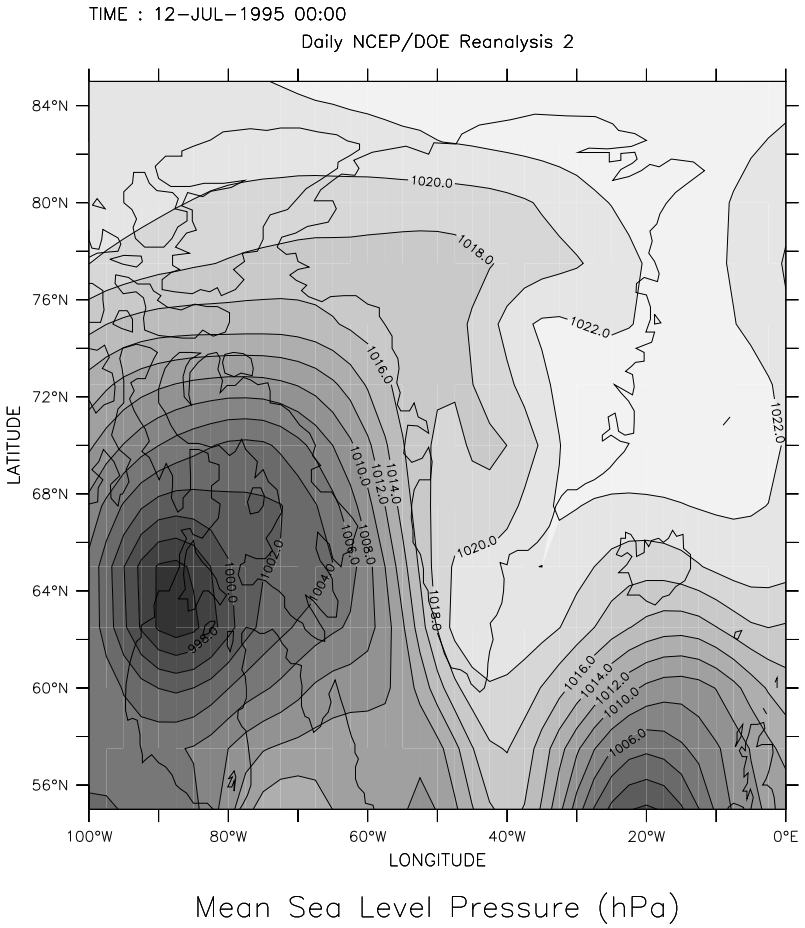

Figure 6.3 : Mean sea level pressure for July 12th of 1995 from NCEP-DOE Reanalysis 2 (Kanamitsu et. al, 2002).

This leads us to conclude that "no melt" in the western ablation zone during this period is unrealistic and is very likely due to rainfall that perturbs the microwave melt signal. The 19-GHz channel is known to be not very sensitive to the atmospheric variability (AS1997) but the wavelength of the 37-GHz channel is of the order of the water droplets diameter in the clouds, which contaminates the signal emitted by the surface. Chevallier and Bauer (2003) use this effect to detect rainfall over oceans.

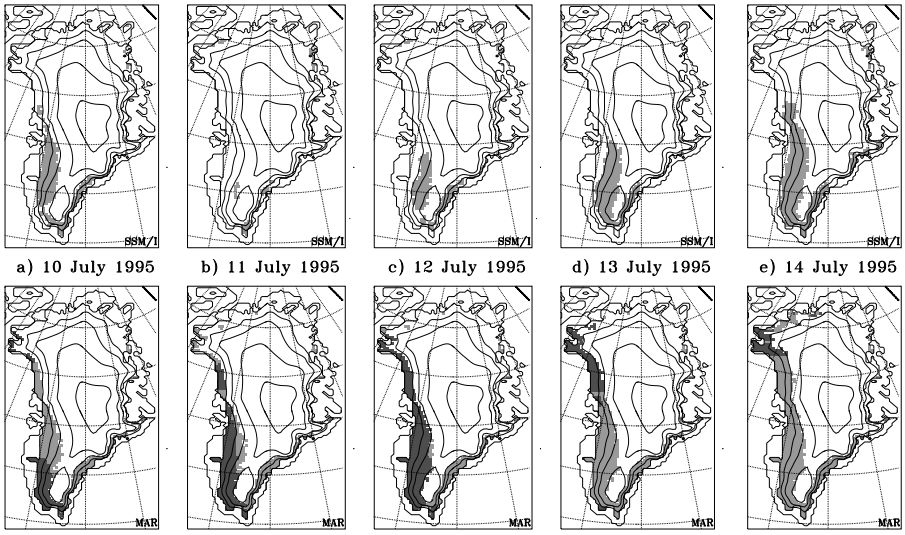

Figure 6.4 : Melt extent (in light grey) derived from the SSM/I satellite observations (Abdalati and Steffen, 1997) (top row) and simulated by MAR (bottom row) for different dates. The dark grey zones in the MAR fields represent the melt zones where MAR simulates daily liquid precipitation higher than 1 mm/day.

6.2.1.3 The summer 1991 at ETH-Camp

These perturbations in the microwave melt signal can be also seen at ETH-Camp in 1991[34]. This camp is located some 40 km away from the ice sheet margin, close to the long-term equilibrium line, at 1154 m a.s.l..

This bias can be seen in 1991 at ETH-Camp, located some 40 km away from the ice sheet margin, close to the long-term equilibrium line, at 1154 m a.s.l.. XPGR detects melt when the LWC is above 1% by volume in the top metre of snow. Figure 6.5 plots here the LWC of the observed snow pack above the ice (Ohmura et al., 1992).

34 We have observational data at ETH-Camp only for summers 1990, 1991 and 1998.

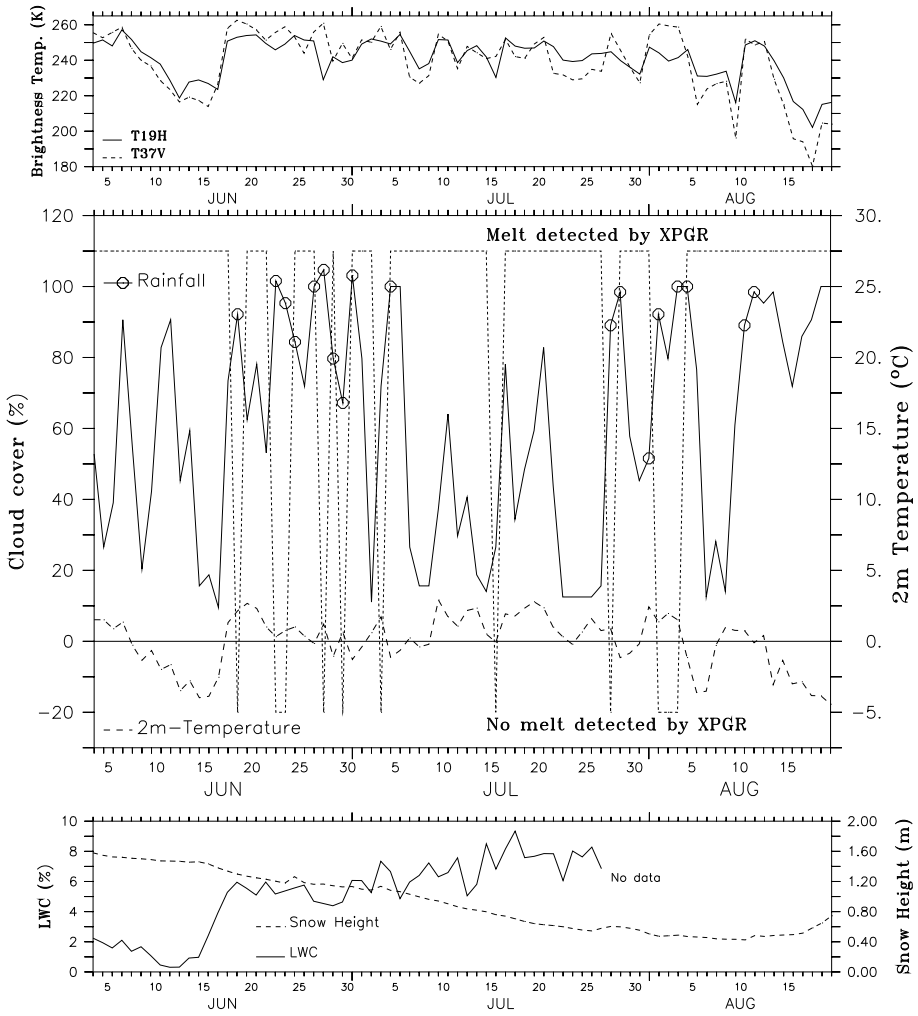

Figure 6.5 : Top: the 19-GHz horizontal polarized brightness temperature (solid) and the 37-GHz vertical polarized brightness temperature (dashed) from SSM/I F-8 satellite at ETH-Camp. Middle: the daily means of the cloud cover (solid) observed at ETH-Camp. The circles on the curve indicate the days when rainfall was observed at ETH-Camp in 1991 (Ohmura et al., 1992). Also shown is the observed 2m-temperature (dashed) at ETH-Camp in 1991 (Ohmura et al., 1992). Finally, the dotted curve shows when XPGR (AS1997) detects melt: above zero when XPGR detects melt, below zero otherwise. Below: the snow height (dashed) and its LWC

(solid) observed at ETH-Camp. The ImpXPGR algorithm detects melt during the whole period (not shown). In detail: improvement n°1 accounts for 11 days, improvement n°2 for 0 days, improvement n°3 for 0 days and improvement n°4 for 0 days.

The LWC reaches values above 1% during the whole period shown in Figure 6.5, except in mid-June although XPGR detects melt. During this period, the height of the observed snow pack is about 1.4 m and the LWC of the top metre of snow is higher than the LWC of the total snow pack because the melt water has not yet reached the depths of the snow pack at the beginning of the melt season. That is why XPGR detects melt during this event. At the end of August, although the 2m-temperature is below zero degrees, the snow pack is still detected as melting by XPGR because the freezing surface temperatures are not low enough to refreeze the liquid melt water from deeper area.

However, XPGR fails several times to detect melt because the T37V is too warm, while the LWC of the snow pack is above 1% and the 2m-temperature is above the freezing point. Rainfall was observed at ETH-Camp in most of these cases which suggests perturbations in the remote observed melt signal.

6.2.1.4 The summer 1998 at JAR-1

Some abnormal short gaps in the melt season detected by XPGR can also be seen in Figure 6.6 at the JAR-1 automatic weather station (AWS) from the Greenland Climate Network (GC-Net). This AWS is situated underneath ETH-Camp at 962 m a.s.l. in the ablation zone. During the warm summer of 1998[35], the snow pack was observed to melt about 2.4 m of water equivalent, continuously from May 24th until the end of September (Steffen et al., 2001).

35 We have measurements at JAR1 only during summer 1998.

XPGR fails several times to detect melt during some days in the melt season when i) it detects melt some days before/after the day considered and ii) the observed (and simulated) 2m-temperature remains positive during each of these small episodes. Therefore, the snow pack should continue to be detected as melting during these days as it was observed on the site (Steffen et al., 2001). For almost each of them, low short-wave incoming radiative fluxes were measured at JAR-1 indicating dense clouds, and rainfall was simulated by MAR most of the time. A rainfall/snowfall episode at the end of May postpones the melt onset to the 28th of May in XPGR fields.

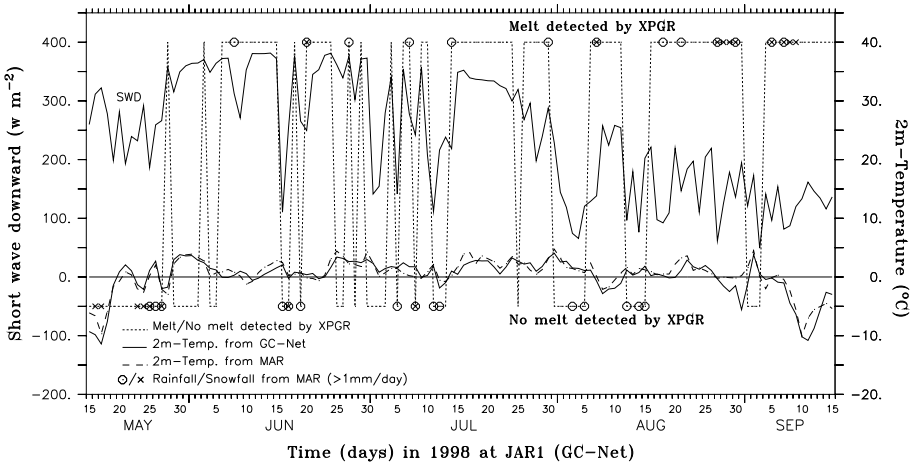

Figure 6.6 : The solid lines show the daily means of the incoming short-wave (top, left axis) and the 2m-temperature (bottom, right axis) measured at the JAR-1 AWS in the summer of 1998 (Steffen et al., 2001). The dotted curve shows when XPGR (AS1997) detects melt: above zero when XPGR detects melt, below zero otherwise. The 2m-temperature simulated by MAR is plotted as a dashed line. Days on which MAR simulates rainfall (resp. snowfall) higher than 1mm/day are indicated by circles (resp. crosses). Finally, the ImpXPGR algorithm and MAR detect melt continuously from May 22th until the end of September (not shown here). The ImpXPRG algorithm detects 42 more melt days than XPGR in 1998 at JAR-1. In detail: improvement n°1 accounts for 34 days, improvement n°2 for 6 days, improvement n°3 for 2 days and improvement n°4 for 0 day.

After September 7th the snow pack begins to refreeze from the surface due to lower air temperatures, but the snow pack is still detected as melting because of the deeper liquid melt water. The improved XPGR algorithm (see below) and MAR detect successfully melt continuously from May 22th to the end of September (not shown here). Finally, a good agreement between the measured and modelled 2m-temperature was also highlighted in Figure 6.6.

6.2.2 Improvements in the original XPGR method

The perturbations in the XPGR melt signal, as discussed in the previous section, are more largely due to dense clouds. This is also highlighted in Figures 6.11 and 6.12 where abnormal low melt signals detected by XPGR are mostly associated to rainfall events simulated by MAR. Hence, the XPGR algorithm must be improved to better incorporate the atmospheric variability. During rainfall events notably, XPGR does not detect melt most of the time because T37V is abnormally high. The ideal solution would be to correct T37V but it is difficult to detect efficiently the perturbations due to atmospheric variability. Therefore, we propose four improvements to the XPGR algorithm. The original XPGR melt retrieval algorithm from AS1997 together with these fours improvements is referred hereafter to as ImpXPGR.

Improvement n°1: i) We impose the continuity of the melt season to remove gaps shorter than three days between two melting days. The XPGR method aims to detect massive melt i.e. when the LWC is higher than 1% in the top metre of snow. Therefore short gaps in the middle of the melt season detected by XPGR, as those shown at ETH-Camp and at JAR1 AWS, are mostly unrealistic. They are in general found to be associated with dense clouds mostly causing precipitation on the ice sheet. It is clear that the snow pack continues to melt when it is raining. When it is snowing, the fresh snow layer above the melting snow pack is normally insufficient to decrease the

LWC below 1 % in the top metre of snow. In the middle of summer, a snow pack with a LWC of 2 % and more is usual and therefore more than 50 cm of fresh snow are needed so that the grid point is not detected as melting any more. Rather than dry fresh snow addition, lower temperatures that refreezing the melt water deeper in the snow pack can efficiently mask the melt signal. However, as shown at ETH-Camp and at JAR1 AWS, periods of refreezing during the melt season lasting less than three days are too short to refreeze in depth the liquid melt water, which prolongs the remote detection of the melt (AS1997). XPGR without corrections detects successfully melting during these refreezing events. The satellite stops to detect melt at the end of the ablation season until the subsurface snow has refrozen. This correction constitutes the main improvement as shown in both Figures 6.7 and 6.8b.

Improvement n°2: Grid points situated at lower altitudes than three adjacent grid points where XPGR detects melt are classified as melting grid points. Indeed, the true resolution of T19H is 69 x 43 km^2 and 37 x 28 km^2 for T37V. These values are then interpolated on a regular grid (25 km x 25 km) by the NSIDC. Therefore, the signal emitted by the ice sheet margin grid points near sea, fjord or fresh melt water lake, in the tundra or on the ice sheet are contaminated by the water signal which is very different from the snow/ice signal. This second correction allows to resolve this problem to a large extent.

Improvement n°3: For each year, we compute the mean T19H temperature and the standard deviation over time and over all the grids points where XPGR (+ improvements n°1 and n°2) detects melt. We add half of the mean standard deviation to this average. This computed value is spatially constant and varies only interannually around 235K to take into account disparities between the three satellites of SMMR-SSM/I data as the

XPGR threshold. If T19H is above this value, we assume that melt takes place: on the one hand, to remove eventual anomalies in the SMMR-SSM/I brightness temperature fields and, on the other hand, to detect melt along the ice sheet margin. It is a correction à la Torinesi et al. (2003). The 19-GHz channel is chosen because it is the least sensitive to the atmospheric variability. As for the second improvement, this correction improves the remote melt detection along the ice sheet margin (see Figure 6.7).

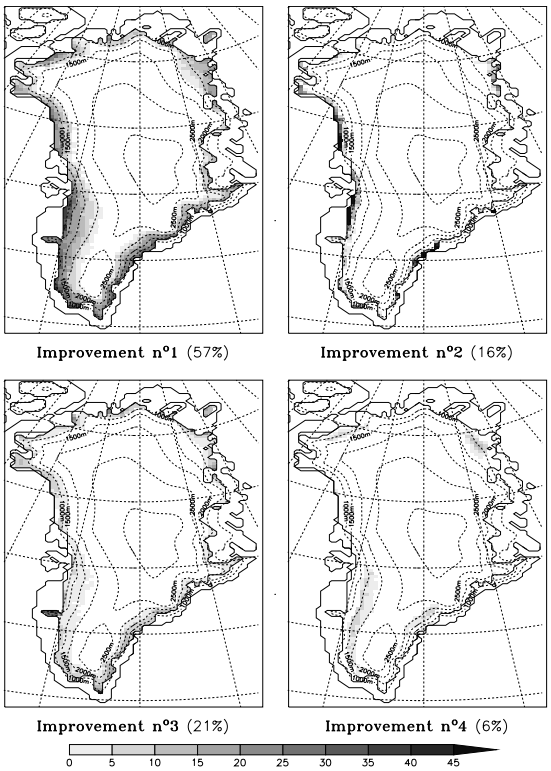

Figure 6.7 : The number of ablation days per year, averaged over the 1979-2004 period, changed by the four corrections of ImpXPGR in comparison to the original XPGR algorithm detection. The first three improvements of ImpXPGR add melting days to original XPGR algorithm detection. The last one from which the absolute value is shown here removes melting days. The relative effect of each improvement is also indicated in brackets. Finally, this figure explains the disparities between Figures 6.12a and 6.12b.

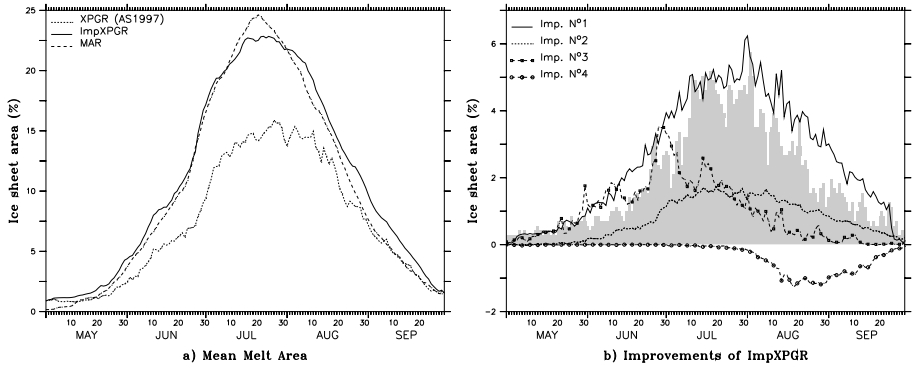

Figure 6.8 : a) The mean melt area for 1979-2004 and b) the mean relative effects of the four improvements of ImpXP7GR to the original XPGR algorithm (AS1997). Also shown in b) is the 1979-2004 mean percentage of Greenland ice sheet area in which MAR simulates daily rainfall greater than 1 mm/day (grey bars).

Improvement n°4: As for the third improvement, we compute the mean T19H temperature and the standard deviation but now when XPGR does not detect melt. We subtract half of the mean standard deviation from this average. To remove anomalies in the remote sensing observations, "no melt" is imposed if T19H is lower than this value (around 176 K). The third improvement adds melting grid points to the melt detected by the original XPGR at the beginning of the ablation season whereas the fourth improvement rather removes melting grid points at the end of the ablation season (see Figure 6.8b).

6.2.3 Evaluation of the improved XPGR method

The same plots as Figures 6.1 and 6.2 are shown in Figures 6.9 and 6.10 with the melt detected by ImpXPGR in addition. The agreement between the MAR-simulated and satellite-retrieved melts becomes significantly better when ImpXPGR is used. For example, at the end of June 1983 or the 11-13th July of 1995, MAR and ImpXPGR compare much better. The abnormally low satellite-derived melt signal due to rainfall events are now corrected in a

large part. Three different threshold values (represented by the error bars) are used to detect melt in the MAR snow pack: a LWC of 0.5 % (upper limit of the error bar), 1 % (the solid curve) and 1.5 % (lower limit of the error bar) in the top metre of snow. Table 6.1 and the error bars in the two next figures highlight the choice of the importance of the LWC threshold value to detect melt in the MAR fields.

Year	LWC_{MAR} > 1.0% vs. XPGR	LWC_{MAR} > 0.5% vs. ImpXPGR	LWC_{MAR} > 1.0% vs. ImpXPGR	LWC_{MAR} > 1.5% vs. ImpXPGR
1983	3.455	2.365	1.885	1.940
1995	5.253	4.230	2.999	2.754

Table 6.1: The Root Mean-Square Error (in percentage of the Greenland ice sheet area) between melt extent simulated by MAR and derived from satellite in 1983 and 1995.

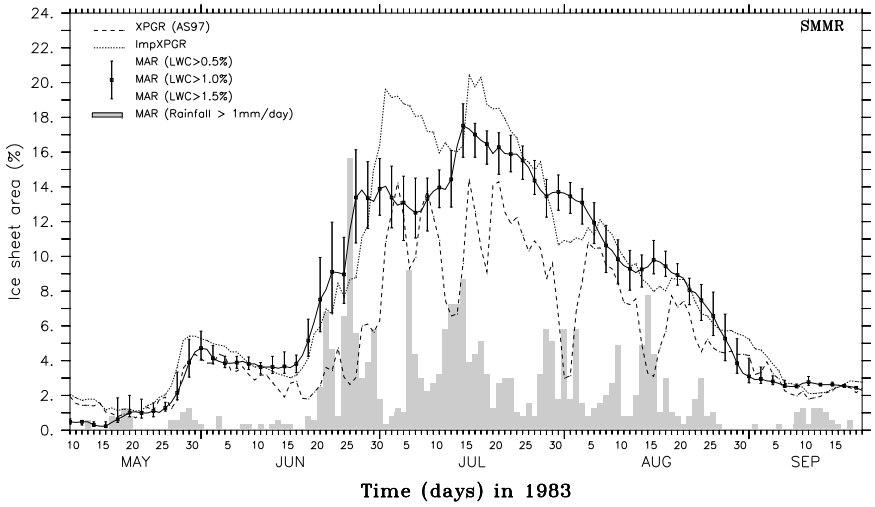

Figure 6.9 : Daily mean melt zone extent detected by XPGR from AS1997 (dashed), by the improved XPGR (ImpXPGR) (dotted) and simulated by MAR (solid) in 1983. Three different LWC thresholds represented by the error bar (0.5%, 1%, 1.5%) are used to detect melt in the MAR snow pack.

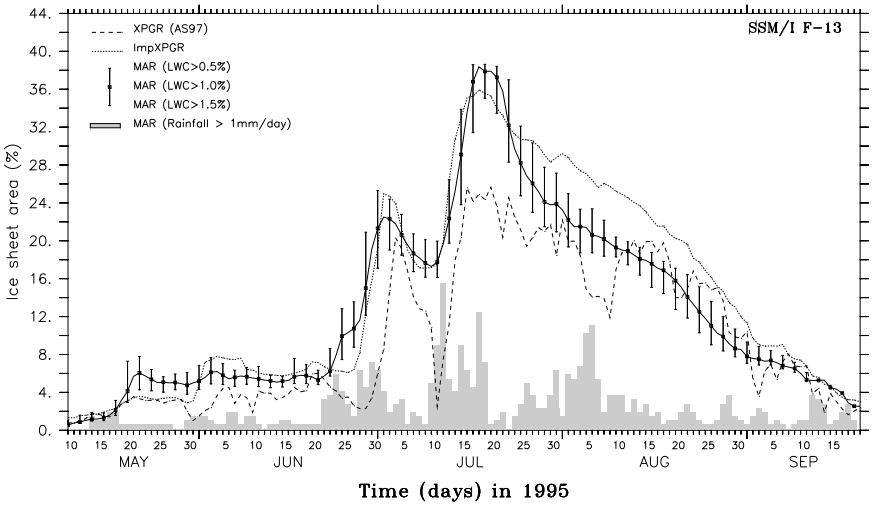

Figure 6.10 : Same as Figure 6.9 but for 1995.

6.2.4 Comparison

Figures 6.11 and 6.12 confirm the better agreement mentioned in the previous section between the MAR-simulated and the satellite-retrieved melt when ImpXPGR is used. The statistics are summarised in Table 6.2. MAR compares better with XPGR when rainfall/snowfall grid points are removed according to Fettweis et al. (2005). As shown in Table 6.2, the removal of rainfall grid points does not improve significantly the comparison with ImpXPGR because this last corrects the melt detection during rainfall. The yearly RMSE are shown in Figure 6.11 below each plot.

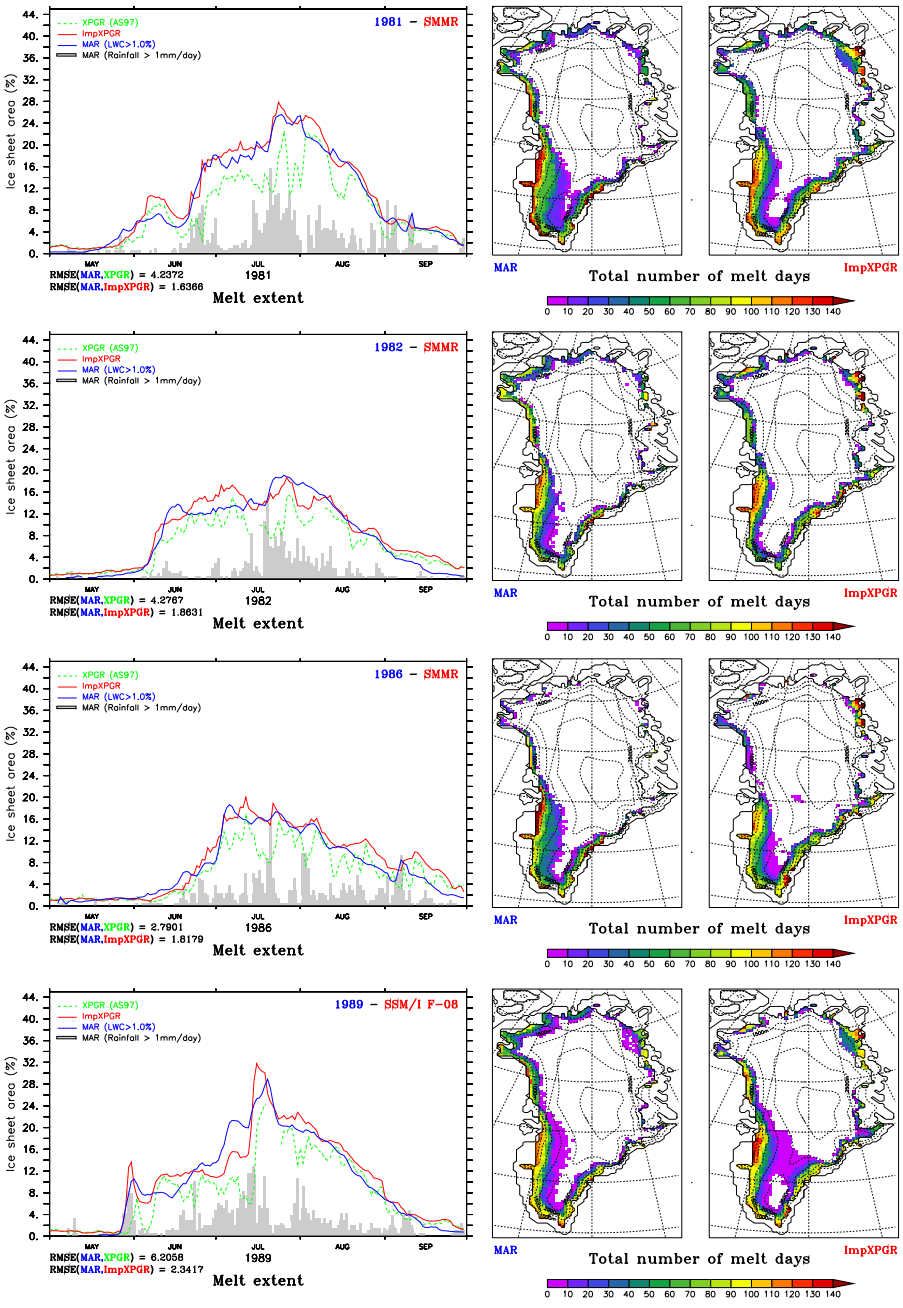
XPGR (AS97)
ImpXPGR
MAR (LWC>1.0%)
MAR (Rainfall > 1mm/day)
1981 - SMMR
Ice sheet area (%)
MAY
JUN
JUL
AUG
SEP
RMSE(MAR,XPGR) = 4.2372
RMSE(MAR,ImpXPGR) = 1.6366
1981
Melt extent
MAR
ImpXPGR
Total number of melt days
0 10 20 30 40 50 60 70 80 90 100 110 120 130 140
1982 - SMMR
RMSE(MAR,XPGR) = 4.2767
RMSE(MAR,ImpXPGR) = 1.8631
1982
1986 - SMMR
RMSE(MAR,XPGR) = 2.7901
RMSE(MAR,ImpXPGR) = 1.8179
1986
1989 - SSM/I F-08
RMSE(MAR,XPGR) = 6.2058
RMSE(MAR,ImpXPGR) = 2.3417
1989

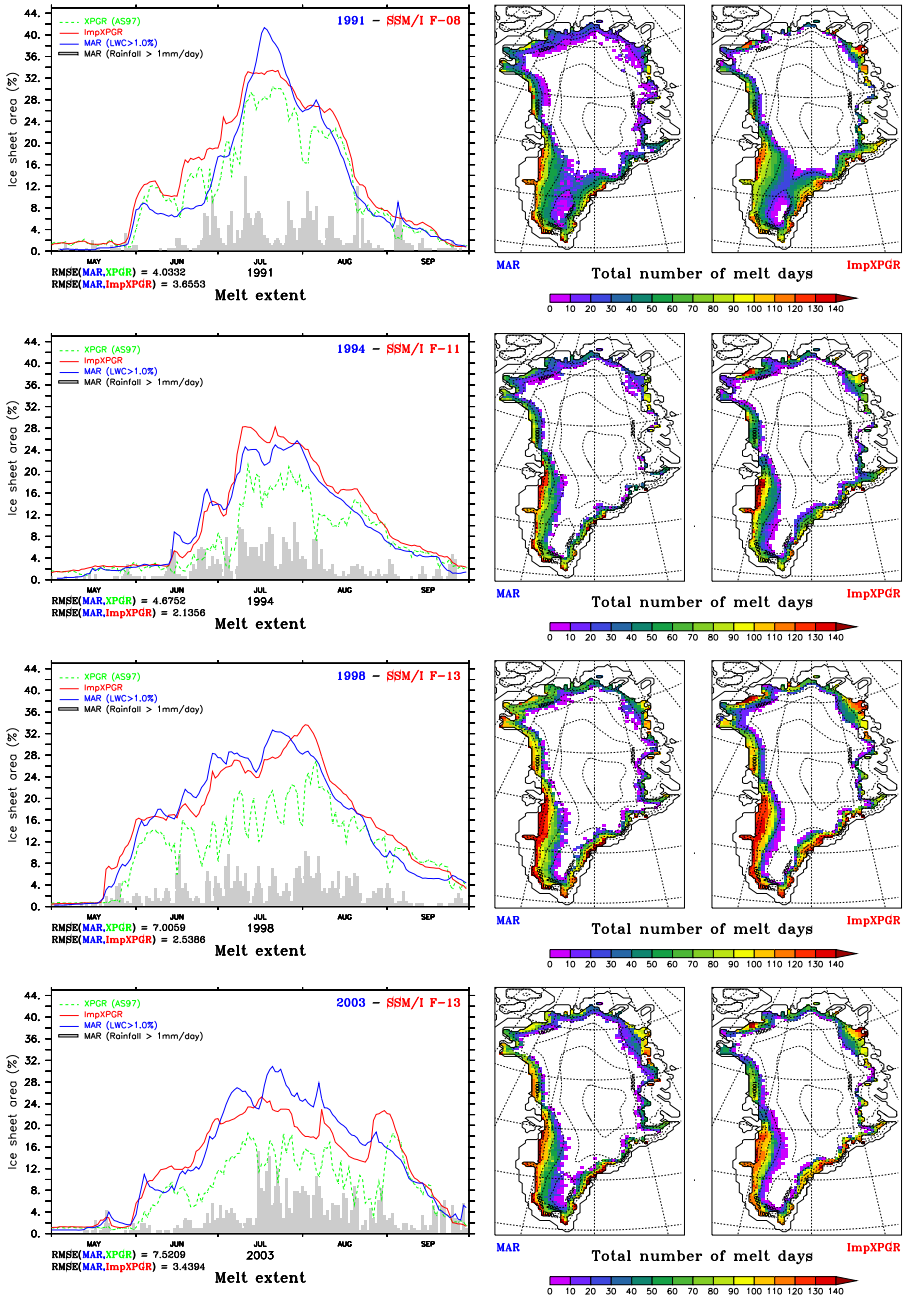

Figure 6.11 : Left: Daily mean melt zone extent detected by XPGR from AS1997 (green), by the improved XPGR (ImpXPGR) (red) and simulated by MAR (blue) for

selected years in SMMR/SSMI data set. Also shown in is the percentage of Greenland ice sheet area in which MAR simulates daily rainfall greater than 1 mm/day (grey bars). Right: Total number of ablation days from May to September simulated by MAR and from ImpXPGR. Similar plots for other years can be seen in Fettweis et al. (2005, 2006).

The abnormally low satellite-derived melt signal due to rainfall events are now corrected in a large part. See for example the improvements during the following time periods: end of July 1981 and 1982, July 21th 1986, May 29-30th 1989, August 6th 1994 and multiple episodes during the melt record years 1998 and 2003. The rainfall perturbations in the XPGR signal become insignificant at the end of melt season when the melt signal is then emitted only by sub-surface melt water (see both last plots of Figure 6.8b). When the surface begins to refreeze, the melt signal comes mainly from the T19H channel which is less sensitive to the cloud liquid water contrary to the T37V channel.

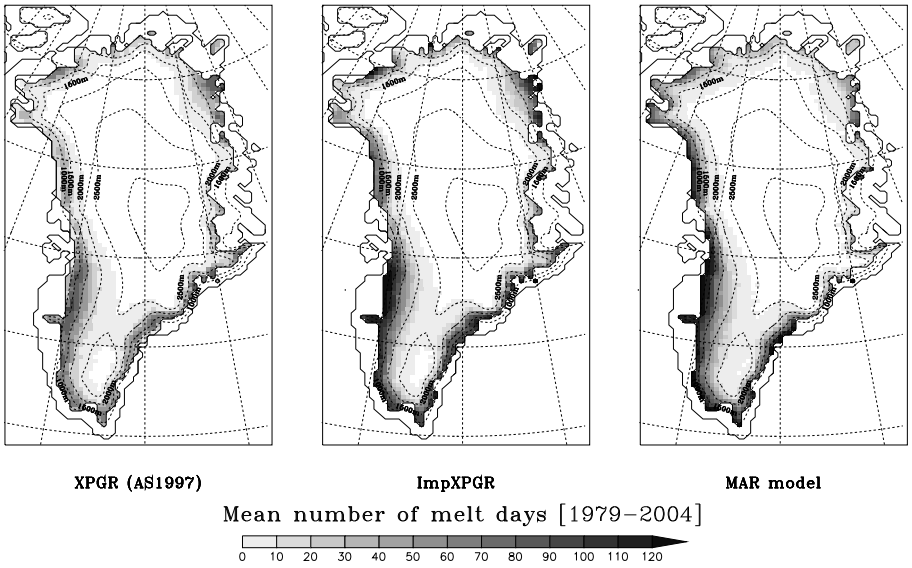

Figure 6.12 : Yearly mean total number of ablation days detected by XPGR from AS1997 (left), by ImpXPGR (middle) and simulated by MAR (right).

Both MAR and ImpXPGR detect much more melt than XPGR along the ice sheet margins (Figure 6.12). Indeed, the closer a grid point is to the ice sheet margin, the higher the probability to have rainfall or clouds with liquid water and the higher the probability that XPGR is biased. As already pointed out by Fettweis et al. (2005), MAR simulates less melt along the eastern and south-eastern mountainous regions of the ice sheet than the XPGR and the ImpXPGR estimates. On the one hand, MAR overestimates somewhat (solid) precipitation in this region (see Chapter 4). This decreases the LWC in the snow pack, raises the albedo and therefore reduces the melt. Given the altitude of this region, no rainfall events are simulated. On the other hand, the satellite-derived values may constitute an overestimation of melt in the high percolation area. The threshold LWC value of 1 % in top metre of snow to detect melt was only validated at ETH-Camp in the ablation zone and should be compared with in situ data from a site located in the higher percolation area. The snow pack characteristics in the ablation zone differ a lot from those in the percolation zone and a similar LWC could have a different melt signal. The importance of the choice of the melt threshold value is shown in Table 6.1 and Figures 6.9 and 6.10. In addition, as pointed out by Torinesi et al. (2003), the microwave brightness temperature could be biased by numerous rock outcrops (boulders) found in this mountainous region.

	MAR	***XPGR***	***ImpXPGR***
Mean melt extent	10.54 %	7.45%	10.83%
Mean melt extent (without rainfall grid points)	9.06%	6.99%	9.64%
Mean melt extent (without snowfall grid points)	8.52%	5.94%	9.06%

	MAR	*XPGR*	*ImpXPGR*
Corr. coefficient with MAR		0.84	0.93
Corr. coefficient with MAR (without rainfall grid points)		0.85	0.92
Corr. coefficient with MAR (without snowfall grid points)		0.84	0.90
RMSE with MAR		5.68%	3.27%
RMSE with MAR (without rainfall grid points)		4.38%	3.15%
RMSE with MAR (without snowfall grid points)		5.11%	3.32%

Table 6.2 : The 1979-2004 mean melt extent, correlation coefficient and Root Mean-Square Error (RMSE) between melt extent simulated by MAR and derived from SMMR-SSM/I remote sensing observations by XPGR and ImpXPGR algorithms. According to Fettweis et al. (2005), MAR vs. XPGR "without rainfall/snowfall grid points" means that all the grid points with MAR daily liquid/solid precipitation greater than 1 mm/day have not been considered in the computation.

6.3 Runoff

Mote (2003) uses a Positive Degree Day (PDD) model to deduce the run-off of the Greenland ice sheet from the satellite-derived melt extent. Here, we propose an estimate of the total ice sheet run-off using the melt extent surface detected by ImpXPGR. It is clear that ImpXPGR can not be used directly to quantify locally the run-off because it is based on a threshold value. Moreover, the run-off comes mainly from the low altitude regions along the ice sheet margin while ImpXPGR sometimes detects melt up to the crest of the ice sheet. However, the more extended the melt area, the higher the melt takes place, the stronger the melt will be and so will be the run-off.

This hypothesis is confirmed in Figure 6.13 where a high correlation of 0.91 (resp. 0.82) is found between the 1979-2004 daily total ice sheet run-off simulated by MAR and the ImpXPGR (resp. XPGR) melt area.

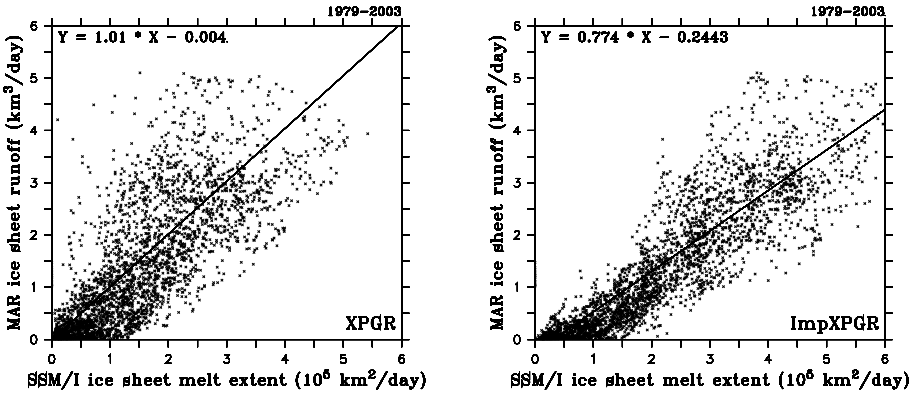

Figure 6.13 : Comparison between the total ice sheet run-off simulated by MAR (in mm) and the melt extent detected by XPGR (left) and ImpXPGR (right) (in 10^5 km^2) for the period 1979-2004. The regression line is also plotted.

Based on this hypothesis and on the MAR results, an empirical estimate of the Greenland ice sheet run-off is made from the ImpXPGR melt extent via this linear regression:

$$Ru_{SMMR-SSM/I} = ME_{SMMR-SSM/I} \times 77.42\,10^{-7} - 0.24$$

where $Ru_{SMMR-SSM/I}$ is the total ice sheet run-off in km^3 yr^{-1} and $ME_{SMMR-SSM/I}$ is the melt extent in km² yr^{-1} detected by ImpXPGR. The coefficients of the regression line are of course "model dependent". But, as far as we assume the linearity in this relationship to be correct, an increase of the melt extent (easily detected by satellite) corresponds to an increase of the ice sheet run-off in the same proportions, no matter the run-off value. The 1979-2004 RMSE between the MAR run-off and the ImpXPGR (resp. XPGR)-derived

run-off estimate is 0.56 (resp. 0.75) km^3. By comparison with Mote (2003) and Box et al. (2004, 2006) estimates, the run-off simulated by MAR (and then derived from SMMR-SSM/I) is lower as we will show in the next chapter despite the good agreement with the satellite melt data. The most important here is the linearity of the relation rather than the values themselves which could be refined later.

The linear relation has a negative intercept. ImpXPGR detects melt when the LWC of the top metre of snow is higher than 1 %. Before running off, a part of the meltwater is retained inside the snow pack assuming a maximum value for the LWC or can accumulate above ice, or snow layers having high densities, or being saturated by liquid water. The run-off of excessive internal and accumulated surface meltwater in the MAR model is based on the work of Zuo and Oerlemans (1996) and described in more detail in Lefebre et al. (2003). The maximum value of the LWC is chosen to be 0.07 according to Colbeck (1974) and corresponds approximatively to a LWC of 3.5 % by volume in the top metre of snow that has a density of 500 kg/m^3 which is a typical value for a melting snow pack. Therefore, ImpXPGR detects the meltwater at the beginning of the ablation season before it can be run off in MAR, which explains the negative constant in the regression.

6.4 Melt trend estimates

Between 1979 and 2004, XPGR and ImpXPGR respectively detect over the Greenland ice sheet an average increase of the cumulated melt extent of 0.78 % yr^{-1} (0.13×10^6 km^2 yr^{-1}) and of 1.69 % yr^{-1} (0.39×10^6 km^2 yr^{-1}) (Figure 6.14a). The MAR results show larger changes although they are consistent with satellite-derived melt. But part of the interannual variability in the passive microwave-derived fields comes very likely from changes in the used data set (see Section 6.1.1); especially between the SMMR (1978-

1987) and SSM/I (1987-2004) satellites where the brightness temperatures used in the XPGR algorithm are not sampled exactly at the same frequencies (AS1997). The cumulated melt extent is defined as the annual total sum of every daily ice sheet melt area. This trend corresponds to a melt area increase of respectively 3.4×10^6 km^2 and 9.8×10^6 km^2 from 1979 to 2004 with a significance[36] of about 83% (resp. 98%) for (Imp)XPGR.

According to the previous section, we find the same trends for the total run-off of the ice sheet. The positive trend becomes more significant with ImpXPGR because rainfall on the ice sheet has been increasing with temperature (Box, 2002). For the 1979-2004 summers, MAR simulates an + 0.087 ± 0.04 °C yr^{-1} increase of the mean air temperature above the ice sheet and an increase of the total rainfall on the ice sheet of 0.38 km^3 yr^{-1} (see Chapter 7). The trends of the mean melting area in June-July-August as defined by AS1997 (Figure 6.14b) and of the maximum melting area as Steffen (2002) (Figure 6.14c) are also shown. But the cumulated melt area parameter is a better indicator of the total melt of the year. The trends simulated by MAR will be discussed in more detail in Chapter 7.

36 The significance has been tested using a Monte-Carlo method with 1,000,000 simulations of autocorrelated data series with the same autocorrelation as the (Imp)XPGR time series.

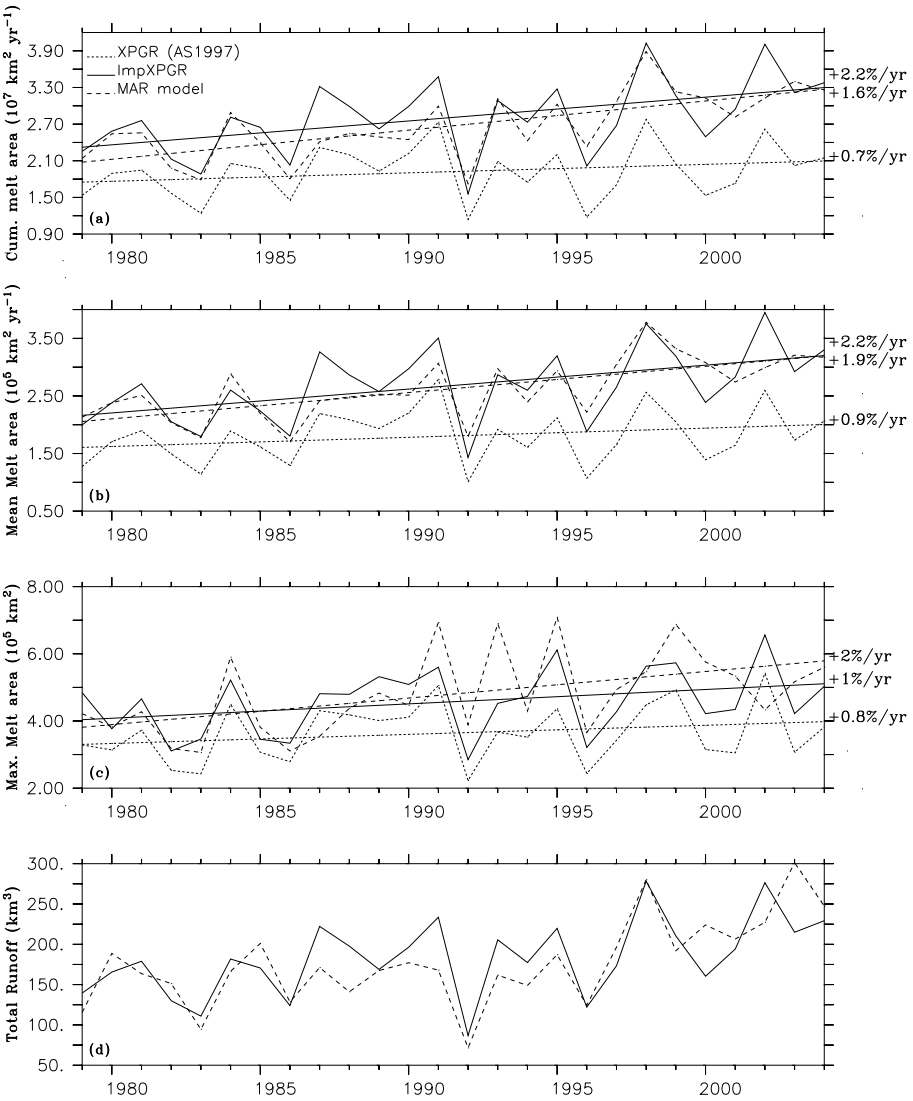

Figure 6.14 : a) Annually cumulated melt area detected by XPGR from AS1997 (dotted), by ImpXPGR (solid) and simulated by MAR (dashed). b) Annually averaged summer mean melt extent defined by AS1997 (June, July, August). c) Maximum melt extent of the ice sheet as in Steffen (2002). d) Total ice sheet run-off simulated by MAR and derived from the melt extent detected by ImpXPGR. The trends are also shown.

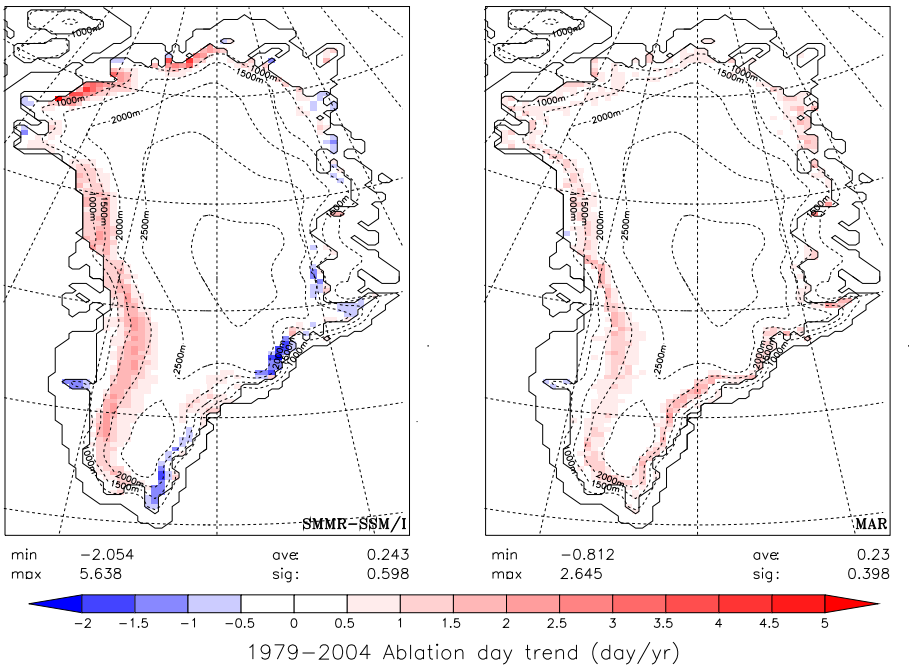

Figure 6.15 : Melt trend (in ablation days yr^{-1}) detected by ImpXPGR (left) and simulated by MAR (right) for the period 1979-2004.

The melt zone extent lies mainly in the northern part of Greenland (especially the Humboldt Glacier) and along the western coast in the higher ablation zone and in the percolation zone (Figure 6.15). In the lower western ablation zone, no change is detected by both satellites and MAR because melt occurs almost always during the melt season (see Figure 6.12). The changes are smaller along the eastern coast and the trend is even negative in the satellite fields. In the south-east of the Greenland, MAR simulates an increase of the snowfall and no rainfall change which can explain the observed melt trends. Indeed, more snowfall and less rainfall decrease the LWC in the snow pack, raise the albedo and therefore reduce the melt. In the

north-west, the changes are not significant. Finally, these regional trends are in agreement with AS2001 (see their Figure 3).

6.5 Discussion and conclusion

A comparison between the Greenland melt extent simulated by the regional climate model MAR and derived from the SMMR and SSM/I satellite data has been performed. This has highlighted some biases during rainfall events in the XPGR algorithm (AS1997) used to retrieve melt area from the passive microwave satellite data. The XPGR technique has been improved to correct the abnormally low satellite-derived melt signals during rainfall events. The agreement with the model has become clearly better. The improved XPGR method shows a significant cumulated melt area increase of 1.7 % yr^{-1} (0.39×10^6 km^2 yr^{-1}) for the period 1979-2004. This increase is mainly situated in the north and along the west coast of Greenland in the ice sheet percolation zone. In the lower western ablation zone, no change is detected by the satellites because melt occurs already almost always during the melt season. The non-modified XPGR technique shows lower changes because the rainfall on the ice sheet has also increased which partly masks the melt increase. The simulated extent and the time evolution of the wet snow zone is successfully compared with the improved SMMR-SSM/I-derived data and a tendency to a melt increase is also simulated by MAR. Nevertheless, MAR underestimates melt along the south-eastern mountain range, likely because of excessive simulated snowfall and the presence of nunataks[37] in this region which could bias the remote sensing signal.

From 1979 to 2004, the satellites show an increase of 40% of the cumulated melt extent. This trend agrees well with recent observations

37 A nunatak is a mountain top that never has been covered by land ice (glaciation, ice age) or glaciers. The wildlife on a nunatak can be isolated by the surrounding glacier, just like an island is in the ocean (source http://www.wikipedia.org).

highlighting rapid and substantial changes on the Greenland ice sheet due to a climate warming (Krabill et al. (2000), Rignot and Thomas (2002), Schiermeier (2004)). Moreover, the melt of the Greenland ice cap may be irreversible if the ice sheet melts completely (Toniazzo et al., 2004). By using model results, we have found a very high correlation between the total Greenland ice sheet run-off simulated by the model MAR and the melt extent area detected by the satellite. Therefore, it is probable that the run-off has also increased in the same proportions which, combined to an ice discharge increase (Zwally et al., 2002), gives an increasing freshwater flux to the North Atlantic Ocean. These results are important for the understanding of the effect of Greenland melting on the stability of the thermohaline circulation.

Chapter 7

The 1979-2005 surface mass balance using the MAR model

Results from a 27-year simulation (1979-2005) reveal an increase of the solid precipitation (+ 1.6 ± 1.8 km^3 yr^{-1}, not significant) and the run-off (+ 4.2 ± 1.9 km^3 yr^{-1}, significant) of surface melt water. The net effect of these competing factors leads to a nearly statistically significant SMB mass loss rate of – 2.7 ± 3.0 km^3 yr^{-1} (with a significance of 87%). The contribution of changes in the net water vapour fluxes to the SMB variability is negligible. The melt water supply has increased because the Greenland ice sheet surface has been warming up +0.09 ± 0.04 °C yr^{-1} since 1979. Latent heat flux, sensible heat flux and net solar radiation have not varied significantly over the last three decades. However, the simulated summer downward infra-red (IR) flux has increased by 8.2 W m^{-2} since 1979. The natural climate variability (e.g. the North Atlantic Oscillation) does not fully explain these changes on the Greenland ice sheet. The recent global warming due to greenhouse gas concentration increase is very likely at the root of these changes. This increase of 78% in the melt water run-off in the period 1979-2005 suggests that the overall ice sheet mass balance has been increasingly negative, given the melt-induced outlet glacier acceleration observed by Rignot and Kanagaratnam (2006).

7.1 Definitions

7.1.1 Surface mass balance

The surface mass balance is defined here as

$$SMB = SF - E - R$$

where

- *SF* = *snowfall* (solid precipitation).
- *E* = *evaporation* including surface water fluxes from a frozen surface (sublimation and deposition) and from a melting surface (evaporation and condensation). The *accumulation* is defined as SF – E.
- *R* = *run-off* defined as the liquid water production (including melt and rainfall) minus the melt water retention.

The snow erosion by the wind is not taken into account here because the SISVAT blowing snow module developed by Hubert Gallée for Antarctica was not full developed and validated at the beginning of this thesis. Despite the weak quantified contribution of this latter to the total Greenland ice sheet SMB in simulations with the MM5 model (Box et al., 2004 and 2006), it would be very interesting to test this module on the Greenland ice sheet.

7.1.2 Ice sheet mass balance

Although the ice sheet representation is limited in SISVAT and no ice dynamical module is yet available, we will discuss briefly the Ice sheet Mass Balance (IMB) of the Greenland ice sheet. As a reminder, the ice sheet mask is fixed and the glaciers do not flow in the MAR simulations. The ice sheet is represented in SISVAT as a static snow/ice layer varying between 8 to 15 metres that can not melt completely (see section 2.2 for more details).

The IMB is defined as the SMB minus the iceberg calving and the basal melting. The Greenland ice sheet gains mass through snowfall and loses it by surface melting and run-off to the sea, together with the production of icebergs and melting at the base of its floating ice tongues. The contribution of basal melting to the IMB is weak but it is generally believed that the mass loss due to snow/ice melting is equivalent to the iceberg calving (Reeh et al.,1999). Moreover, an increasing melt could accelerate the ice discharge according to Zwally et al. (2002).

The basal melting and calving are yet very badly known and estimated (Box et al., 2006). Reeh et al. (1999) estimated the glacier discharge to 263 $km^3\ yr^{-1}$ and the basal melting to 35 $km^3\ yr^{-1}$ by assuming an ice sheet equilibrium with the SMB. Therefore, these estimates does not account for the melt-induced outlet glacier acceleration observed by Zwally et al. (2002) and represent minimum values in the present climate characterized by an increasing melt water supply.

7.1.3 Surface energy balance

The ice sheet surface temperature is the result of the Surface Energy Balance (*SEB*) equation given by:

$$SEB \equiv (1-\alpha)\ SWD + LWD - HCF - LHF - SHF - \varepsilon\ \sigma\ T^4 = 0$$

where α is the albedo of the snow/ice, *SWD* is the Short Wave Downward flux (solar radiation) in W/m^2, *LWD* is the Long Wave Downward flux (infra-red radiation), *HCF* is the Heat Conduction Flux through the snow pack, *LHF* is the Latent Heat Flux, *SHF* is Sensible Heat Flux, ε is the emissivity, σ is the Stefan-Boltzmann constant (= $5.6703 \times 10^{-8}\ W/m^2\ K^4$) and *T* is the surface temperature in kelvins.

7.2 The Greenland surface mass balance

7.2.1 Average annual rates of the SMB components

All the models in Table 7.1 have an annual total ice sheet mass snowfall rate of ~ 600 km^3 yr^{-1}. The net erosion by surface water vapour fluxes is estimated to be ~ 50-100 km^3 yr^{-1}, which gives an accumulation rate (usually noted *P-E*) of approximatively 550 km^3 yr^{-1}. The MAR simulated annual snowfall and net surface water vapour fluxes are respectively plotted in Figures 7.1 and 7.2. The MAR solid precipitation exhibits recognized spatial patterns found from interpolation of ice core and snow pit data (e.g., Ohmura et al., 1999; Cogley, 2004) or simulated by models (e.g., Hanna et al., 2002; Box et al., 2006). See Chapter 4 for more details above the validation of the MAR precipitation.

Unlike other models, the deposition/condensation accumulation simulated by MAR dominates the sublimation/evaporation erosion in average over the whole ice sheet (see Table 7.1). The MAR simulated erosion in the low altitude regions (i.e. in the ablation zone) is in agreement with the Polar MM5 outputs (Figure 7 of Box et al., 2006) and the Box and Steffen (2001) estimates based on GC-net observations (see Figure 7.2). At Summit, MAR is also consistent with the GC-Net observations. But along the perimeter of the percolation zone and at South Dome, MAR overestimates the deposition. Three likely sources of error could explain this bias. We have shown in Chapter 3 that MAR underestimates the temperature during the polar night and at the top of the ice sheet when/where the temperature is the coldest, which increases abnormally the deposition.

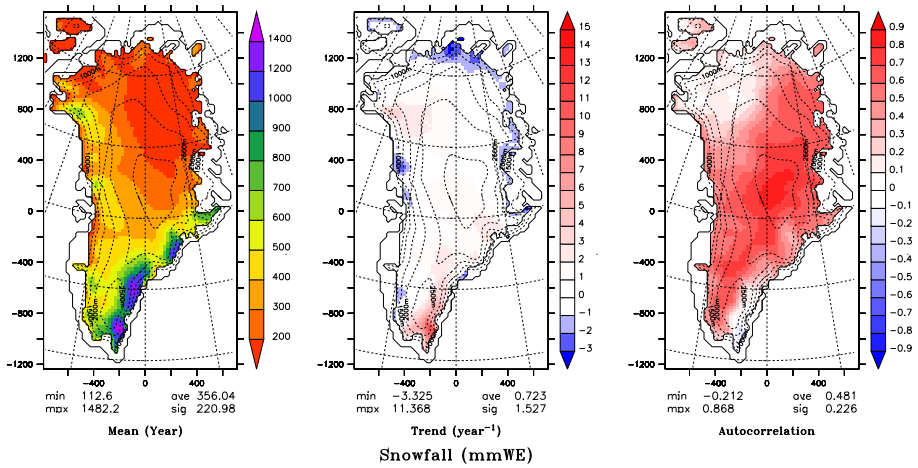

Figure 7.1 : The 1979-2005 annual mean (left), 27-year linear regression change (centre) and autocorrelation (right) of the snowfall. The autocorrelation is defined as the correlation between time series of the total ice sheet snowfall with that at each grid location. Minimum and maximum values are indicated as well as the ice sheet average and the standard deviation.

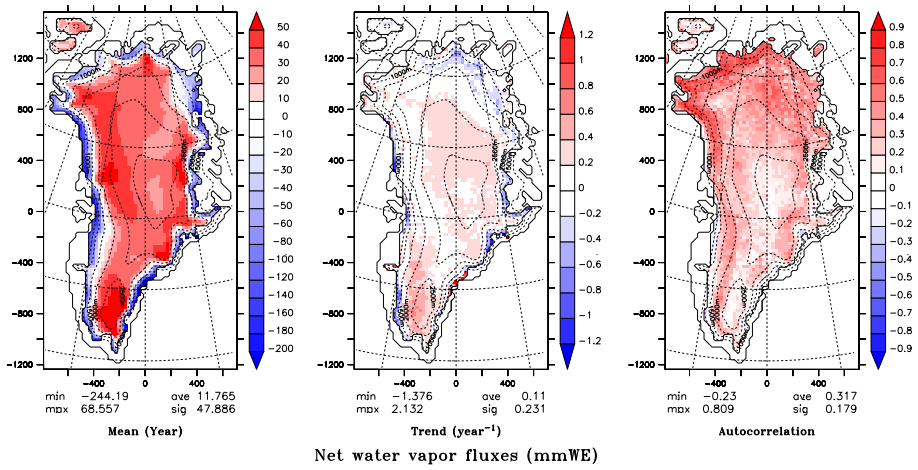

Figure 7.2 : Same as Figure 7.1 but for the net surface water vapour fluxes (i.e. the evaporation, condensation, sublimation and deposition).

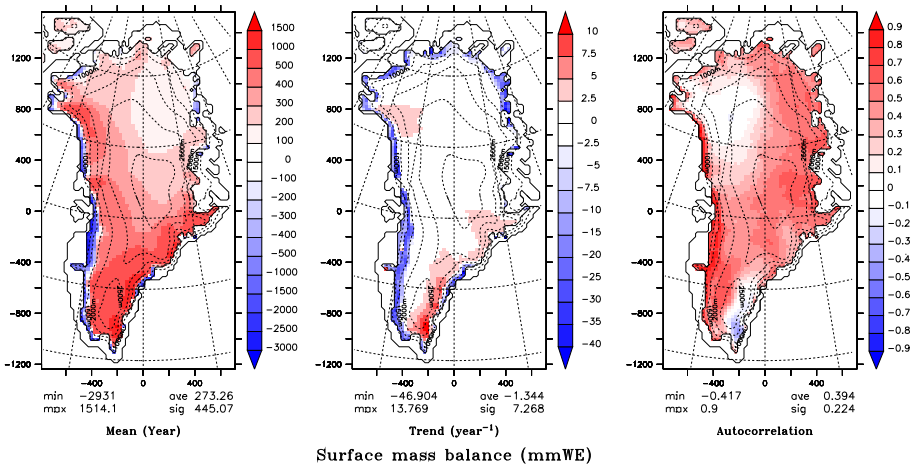

Figure 7.3 : Same as Figure 7.1 but for the surface mass balance.

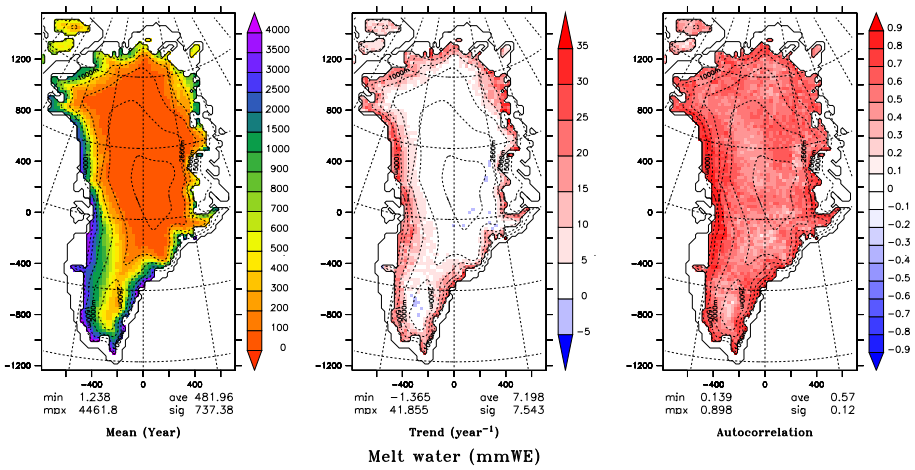

Figure 7.4 : Same as Figure 7.1 but for available melt water.

The run-off is estimated to be ~ 250-300 km^3 yr^{-1}. The larger run-off rate simulated by the Polar MM5 model could be partly explained by the discrepancies in the used ice sheet mask i.e. in the classification of ice/land/ocean land surface type. Along the south-eastern coast, the MM5 ice sheet margin runs directly along the sea, which increases significantly the melt overall. In other ice sheet masks (Mote, 2003; Fettweis et al., 2005;

Hanna et al., 2005), there are tundra grid points between the ice sheet margin (which is higher in altitude as a result) and the sea. The disagreement between both MAR and MM5 masks along the south-eastern coast can be seen in Figure 7.5. The run-off rate simulated by MAR is weaker than other estimates, although the MAR melt area is in complete agreement with satellite observations. Furthermore, the available amount of melt water is simulated to be 821 $km^3\ yr^{-1}$ for a run-off rate of 178 $km^3\ yr^{-1}$.

- On the one hand, this suggests that the MAR retention/refreezing of the melt water is likely too high. The run-off of the excessive internal and accumulated surface melt water in MAR (shown in Figure 7.4) is based on the work of Zuo and Oerlemans (1996) and described in detail in Lefebre et al. (2003). It should be good to check/validate again the implementation of this parametrisation in SISVAT and the choice of the constants c_1, c_2 and c_3 in the run-off rate formula (see section 2.1.2) by comparing for example the results obtained with the Pfeffer et al. (1991) parametrization used by the MM5 model. Unfortunately, very few data are available to validate such parametrizations.
- On the other hand, the MAR ice sheet mask could be revised by including glacier tongues as in Box et al. (2004, 2006) (e.g. in southern Greenland). Maximum run-off rates are found at these outlet glaciers.

Finally, the ECHAM4 and MIT models (Bugnion and Stone, 2002) underestimate also the ablation because the absence of run-off along the northern coast of the ice sheet due to a excessive rate of the melt water according to Bugnion and Stone (2002).

	Snowfall	Rainfall	Sublimation / Evaporation	Blowing snow	Runoff	Surface mass balance	Iceberg calving + Basal melting
MAR *Period: 1979-2005* *Area: 1,701 x 10^6 km^2*	615±50	40±6	-20±5 Accumulation = 634±54		179±50	464±83	
Polar MM5 *Period: 1988-2004* *Area: 1,691 x 10^6 km^2*	617±59	24±7	64±8 Accumulation = 534±131	34±6	373±66	170±152	
ECHAM4	585		46 Accumulation = 540		122		
MIT	649		95 Accumulation = 554		162		
ECMWF analysis *Period: 1958-2003*	Accumulation = 573±70				280±69	293±104	
Mote (2003) *Period: 1988-1999* *Area: 1,648 x 10^6 km^2*	645	25	77 Accumulation = 539		278	261	
Reeh et al. (1999) *Area: 1,707 x 10^6 km^2*	Accumulation = 602				304	298	263+35

Table 7.1 : Annual mass balance components simulated by MAR, Polar MM5 (Box et al., 2006), ECHAM4 and MIT models (Bugnion and Stone, 2002), derived from the ECMWF (re)analysis (Hanna et al., 2005), derived from SSM/I observations (Mote, 2003) and estimated by Reeh et al. (1999) which uses in situ observations. The period over which it is averaged and the ice sheet area are shown in italic. Units are km^3 yr^{-1}.

The SMB estimates vary between 170 km^3 yr^{-1} and 464 km^3 yr^{-1}. The Polar MM5 estimate is likely too low given the overestimation of the run-off rate. The MAR estimates are clearly too high due to both overestimations of the deposition and the melt water retention. Other estimates agree with a SMB

rate of ~ 300 km^3 yr^{-1} balancing the glacier discharge and basal melting rate estimated by Reeh et al. (1999).

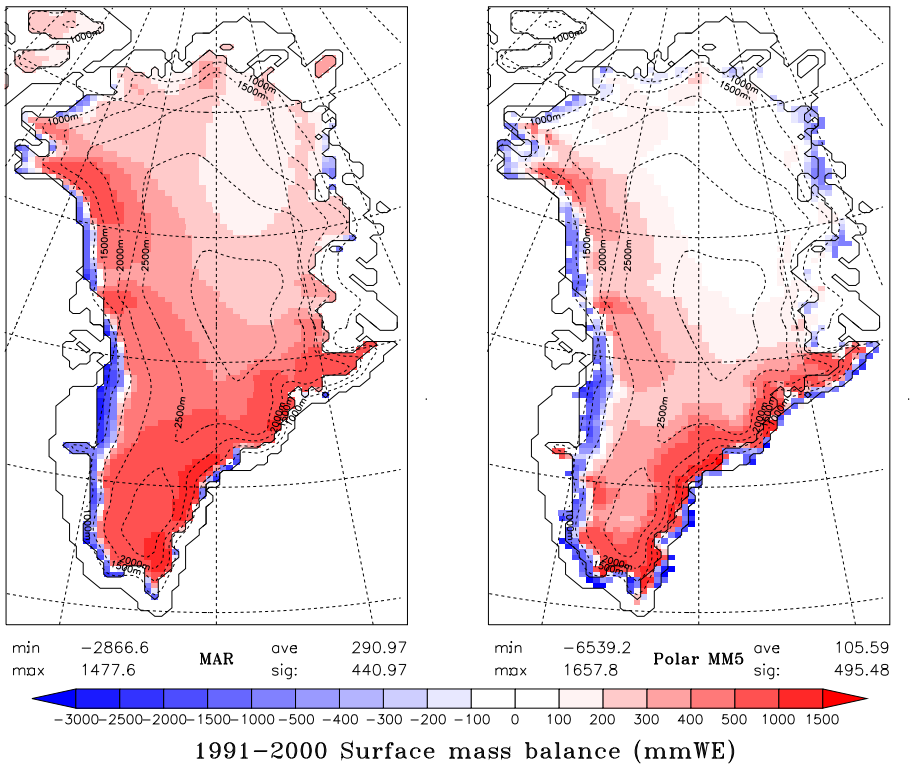

Figure 7.5 : Comparison of the 1991-2001 annual mean SMB simulated by MAR and by Polar MM5 (Box et al., 2004). The Polar MM5 24km-results are interpolated on the MAR 25km-grid. Finally, the Polar MM5 SMB is calibrated with in situ observations (snow pits, ablation stakes, ice cores) to remove systematic biases via statistical regression (Box et al., 2004 and 2006). The Polar MM5 data comes from [http://polarmet.mps.ohio-state.edu/jbox/data/.](http://polarmet.mps.ohio-state.edu/jbox/data/)

In Figure 7.5, we observe a similar overall pattern in MAR and Polar MM5 modelled SMB despite the ice sheet mask discrepancies. The equilibrium line is identically simulated by both models. The maximum in accumulation area occurs along the south-eastern mountain chain and the minimum at the north-east. The accumulation is higher in the MAR model along the west

accumulation area margin, at Summit and in the South Dome vicinity because of the overestimated deposition and snowfall. As mentioned above, the disparities in the run-off rates are explained for a large part by the ice sheet mask used by both models. For example, in southern Greenland, the MM5 ice sheet mask stretches at lower altitudes than the MAR mask which increases significantly the total run-off rates.

This section highlighted biases (overestimation of the deposition, of the melt water retention and of the snowfall) in the MAR estimates of the SMB components. These biases are nonetheless systematic and are assumed to be repeated each year. Therefore, it is reasonable to suppose that they only weakly affect the temporal variability of the components simulation and that the MAR results can be used in a reliable way to study the SMB components evolution over the last 27 years.

7.2.2 Temporal variability and trend of the SMB components

The SMB is governed, on the one hand by the accumulation (snowfall) and on the other hand, by the run-off (temperature). The interannual variability in precipitation and ablation causes SMB fluctuations (with a correlation of 0.77 (see Figure 7.6)). In 1985, the SMB is minimum because of a weak snowfall rate. Other minima, rather due to high run-off rates, are found in 1998 and 2003. In 2005, low snowfall and high run-off rate induce a negative anomaly in the SMB. Maxima of SMB occur in 1983, 1992 and 1996 owing to both negative run-off and positive snowfall anomalies. Integrated over the ice sheet, the 27-year snowfall rate shows a positive trend[38] of + 1.6 ± 1.8 km^3 yr^{-1} (with a significance of 72%). The run-off

38 The error bar in the trend is the division of the standard deviation of the MAR field temporal series by the number of years (i.e. 27). The significance has been tested using a Monte-Carlo method.

increase is evaluated to be + 4.2 ± 1.9 km^3 yr^{-1} (with a significance of 99%) which gives a rate of global average sea level[39] rise of +1.1 10^{-2} mm yr^{-1}. The net effect of these competing factors lead to a nearly statistically significant (87%) SMB mass loss rate of – 2.7 ± 3.0 km^3 yr^{-1}. The contribution of changes in the net water vapour fluxes to the SMB variability is negligible (+ 0.26 ± 0.19 km^3 yr^{-1}). These results are consistent with the Polar MM5 estimate (Box et al., 2006) and some recent observations (Krabill et al. (2000), Rignot and Thomas (2002), Schiermeier (2004), Alley et al. (2005)). As shown in Figures 7.5 e) and f), the heavier precipitation in the accumulation zone partly offsets the significant melt increase in the ablation zone. Indeed, the SMB variability shows an insignificant positive trend above 1500 m (+ 1.5 ± 1.5 km^3 yr^{-1}) against a significant negative trend of – 4.0 ± 2.0 km^3 yr^{-1} below 1500 m, as it was recently observed by the satellite laser altimetry (Kabrill et al., 2004; Johannessen et al., 2005)).

According to Johannessen et al. (2005), the ERS-1 and ERS-2 satellites[40] show an elevation increase of 6.4 ± 0.2 cm yr^{-1} in the vast interior areas above 1500 m and an elevation change rate of –2.0 ± 0.9 cm yr^{-1} below 1500 m throughout the period 1992-2003. The total ice sheet spatially averaged elevation change shows a positive trend of 5.4 ± 0.2 cm yr^{-1} which is in complete disagreement with other studies. The generally accepted sign of the Greenland ice sheet mass balance since the last nineties is negative (Alley et al., 2005; Hanna et al., 2005; Zwally et al., 2005; Box et al., 2006). Therefore, the results of Johannessen et al. (2005) need to be considered with caution. On the one hand, the marginal areas (outlet glaciers) are not measured completely using ERS-1/ERS-2 altimetry. MAR shows that pronounced ablation in low-elevation marginal areas offsets the elevation

39 The computation was made by using an area of the World Ocean of 361 million km².
40 Satellites from the European Space Agency (ESA).

increases that we observed in the interior areas. On the other hand, the ERS 11-year long data set remains too brief to establish long-term trends.

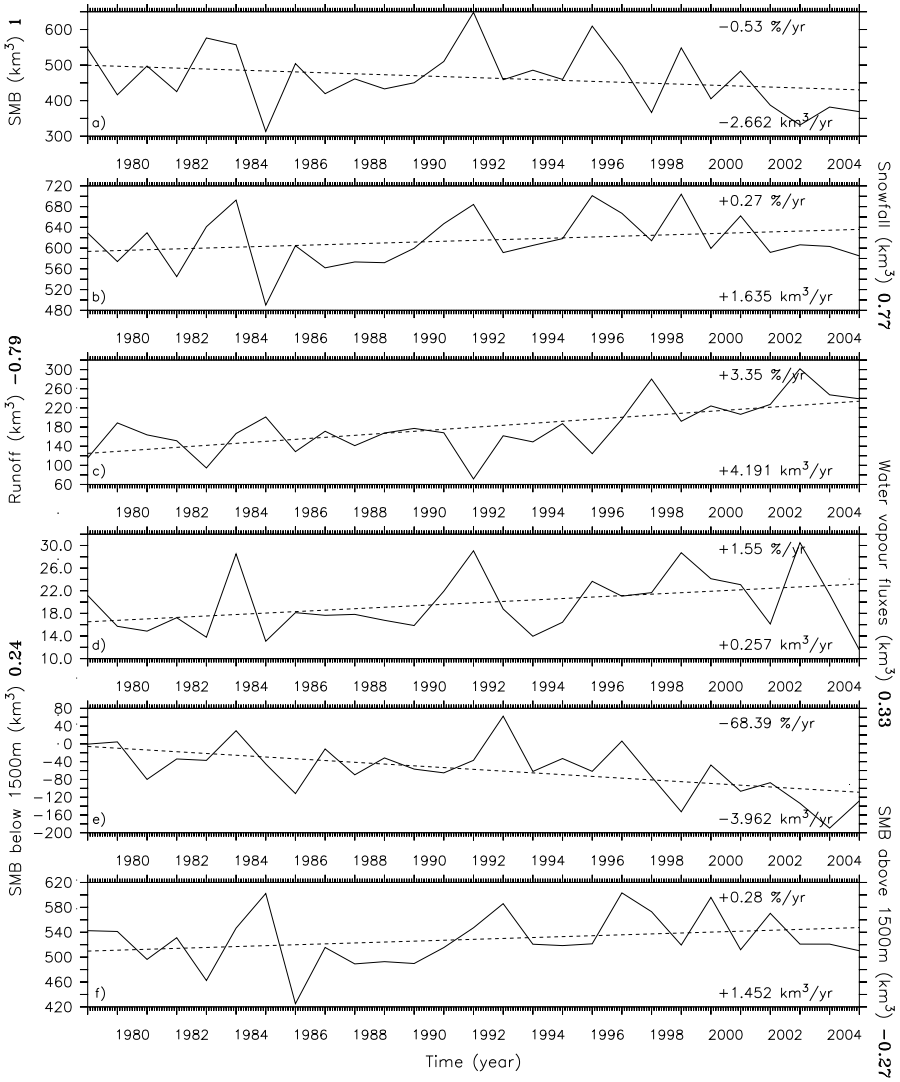

Figure 7.6 : Time series of the annual total ice sheet a) SMB, b) snowfall, c) run-off, d) net water vapour fluxes, e) SMB averaged over the ice sheet area below 1500m and f) above 1500m. Units are km³ yr⁻¹. The correlation with the whole ice sheet SMB is indicated in bold in the titles. The linear trends are also noted in % and in km³ yr⁻¹.

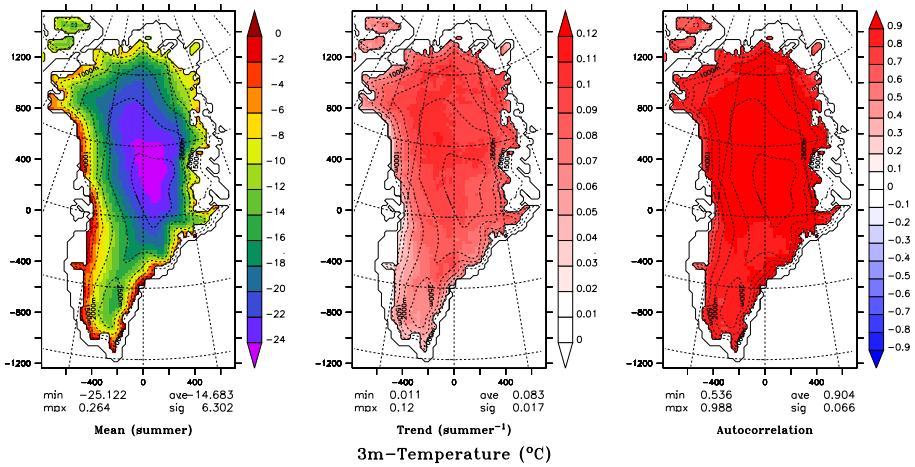

Figure 7.7 : Same as Figure 7.1 but for mean summer[41] temperature.

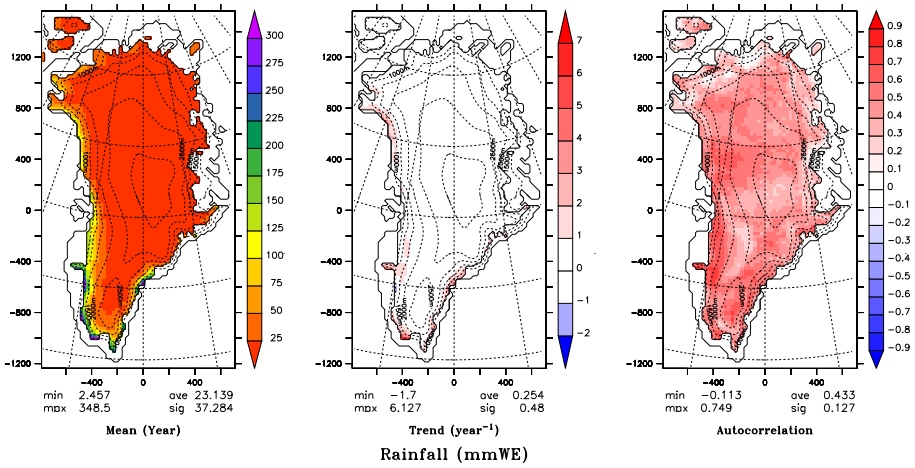

Figure 7.8 : Same as Figure 7.1 but for rainfall.

The melt increase occurs everywhere in the ablation zone (Figure 7.4b) according to the uniform ice sheet warming (Figure 7.7b). The warming is nonetheless larger above the ice sheet than along the ice sheet margin given that the surface temperature of melting snow/ice is limited to 0°C. The higher positive snowfall trend occurs near the south-eastern accumulation

41 Summer = from 1st May to 30th September

maximum (Figure 7.1b) and negative trends are found in the ablation zone in the north of the Greenland as in Box et al. (2006). These negative trends are partly due to the warming, which leads to an increase in the amount of liquid precipitation versus solid precipitation (Figure 7.8). This increases the melt water supply and also has consequences for glacier flow lubrication according to Zwally et al. (2002). Given that the melt increases everywhere, positive trends in the SMB occur only in the regions where snowfall increases and dominates over the ablation (Figure 7.3b). MAR simulates negative 27-year SMB trends almost everywhere in the ablation zone and a significant positive SMB trend in the south-eastern of the Greenland ice sheet.

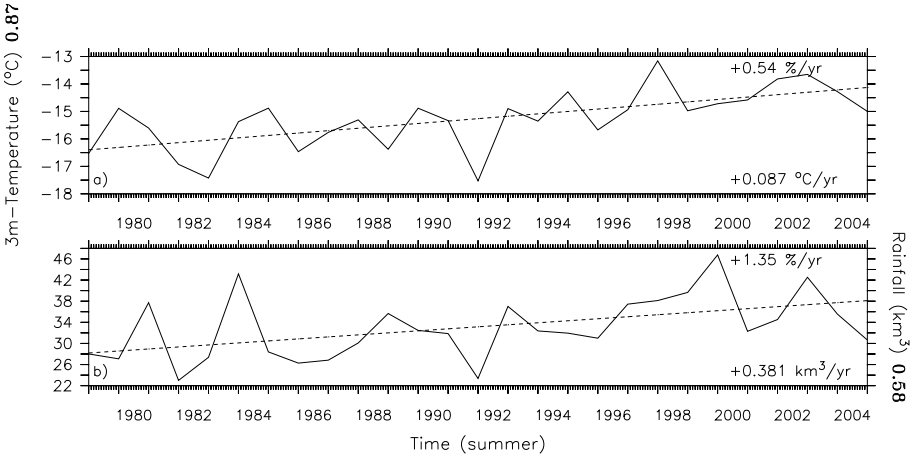

Figure 7.9 : Time series of the summer (from 1st May to 30th September) total ice sheet a) temperature average (in °C su-1) and b) rainfall (in km3 su-1). The correlation with the run-off (Figure 7.6) is indicated in bold in the titles.

The summer temperature exhibits a robust correlation with the melt water supply and therefore with the run-off (0.87) of the ice sheet as a whole (Figure 7.9). That is why the positive degree-day models are entirely based on this assumption. Heavier rainfall increases also the liquid water supply

but a large part of this increasing amount of liquid precipitation is explained by the warming estimated to be ~0.09°C yr^{-1} (with a significance of 99%). Figure 7.1 shows negative snowfall trends in the western ablation zone because of an increasing fraction of liquid precipitation due to higher temperatures. However, the rainfall yearly variability (+0.4 km^3 yr^{-1}) explains no more that 10 % of the run-off positive 27-year trend estimated by MAR to be +4.2 km^3 yr^{-1}.

According to Box et al. (2004), these considerations allow us to estimate the SMB anomaly for the entire ice sheet from the (summer) temperature and the snowfall anomalies as:

$$\Delta SMB = -40.25\ \Delta T_{year} + 1.19\ \Delta SF,\ r = 0.92,\ RMSE = 31.4mm$$

$$\Delta SMB = -45.98\ \Delta T_{summer} + 1.07\ \Delta SF,\ r = 0.95,\ RMSE = 26.4mm$$

where ΔSMB is the annual SMB anomaly in mmWE, ΔT *is* the annual (resp. summer) temperature anomaly in K and ΔSF is the annual snowfall anomaly in mmWE. The correlation (r) and the root mean square error (*RMSE*) are also given. Therefore, more than 95% of the variance in the modelled surface mass balance totals is explained by the summer (from 1st May to 30th September) temperature anomaly and the annual solid precipitation variability despite the fact that these variables are not correlated. This confirms our hypothesis about the acute sensitivity to the SMB to both temperature and snowfall anomalies.

7.2.3 Spatio-temporal variability and autocorrelation of the SMB components

The autocorrelation[42] shows where regional variability best captures the variability over the complete ice sheet. The snowfall at Summit is for example an excellent indicator of the total ice sheet snowfall variability (Figure 7.1, right). This fully justifies the choice of this location for ice-core Greenland climate reconstructions[43]. A low autocorrelation occurs in the north-west and in the south-east of Greenland. This pattern (associated to positive trends) can also be seen in the SMB autocorrelation (see Figure 7.3, right). It also appears that the melt variability in the (western) ablation zone is more important than the solid precipitation variability to influence the SMB. Finally, Figure 7.7 shows a global and uniform warming of the Greenland ice sheet. This suggests that this warming likely comes from external factors (via the ECMWF (re)analysis data).

7.2.4 The equilibrium line altitude

Remember that the Equilibrium Line Altitude (ELA) is defined as the elevation where the SMB equals zero. Therefore, the ELA provides an useful indicator of the combined influence of thermal and precipitation forcing on the SMB.

Our results are in good agreement with Zwally and Giovinetto (2001) parametrisation. The general pattern is obviously an ELA decrease with increasing latitude. Regional variation in the ELA versus latitude pattern results from changes in local topography and precipitation shadow effects due to proximity of dominant cyclonic systems. The relatively weak ELA at

42 The autocorrelation is defined as the correlation between time series of the total ice sheet accumulation with that at each grid location

43 See the project GISP2 (Greenland Ice Sheet Project Two) at http://www.gisp2.sr.unh.edu/

61°N results, for example, from abundant snowfall observed in this region. The trends for these last 27 years is a positive shift of +4.8m yr^{-1} (resp. 9.6m yr^{-1}) in the western (resp. eastern) Greenland ELA. This corroborates the dominance of the thermal factors variability on the SMB.

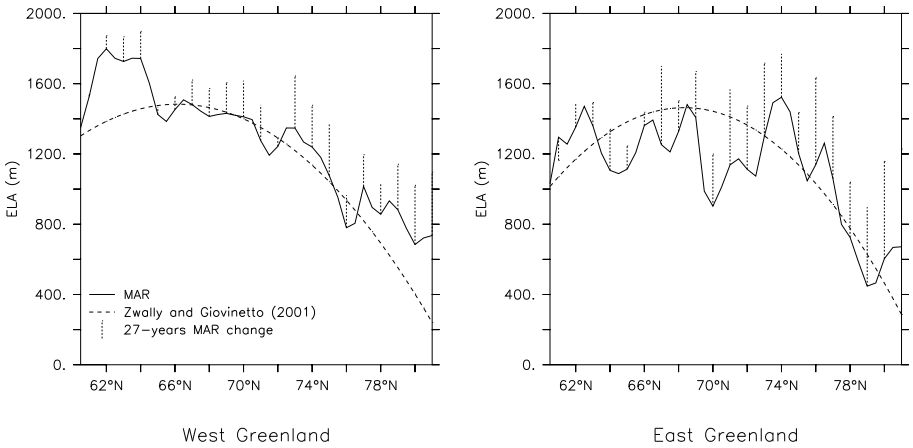

Figure 7.10 : Average equilibrium line altitude variations in MAR simulation (solid) and estimated by Zwally and Giovinetto (2001) parametrization (dashed). The MAR 27-year changes are also shown (dotted).

7.2.5 The albedo-temperature feedback

Mote (2003) suggests that high accumulation years are often associated with low ablation for the entire ice sheet due to the well known albedo-temperature feedback. Low accumulation rates lead to more rapid losses of winter snow mass and to higher degree day factors for bare ice in the ablation zone. The higher the snow pack height at the end of spring, the later the appearance of bare ice (with a lower albedo) (Fettweis et al., 2005).

Figure 7.11 reveals however that the hypothesis of Mote (2003) does not explain the SMB variations of these last 27 years. Indeed, the winter snow accumulation has been increasing on the ice sheet while the SMB variability suggests a negative trend. We have found in previous paragraphs that the

thermal factors dominate presently the SMB sensitivity rather than the precipitation changes. These last results confirm our assumption.

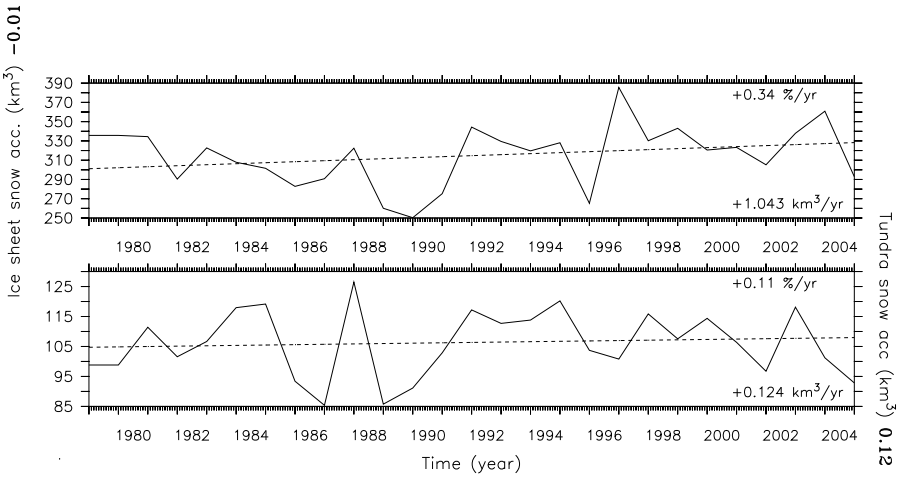

Figure 7.11 : Time series of the winter[44] snowfall before the considered year (in km³ yr⁻¹) over a) the ice sheet and b) the tundra. The correlation with the SMB (Figure 7.6) is indicated in bold in the titles.

7.3 The Greenland ice sheet surface energy balance

Over the Greenland ice sheet, the net solar radiation (SWDn) is relatively weak in the Surface Energy Balance (SEB) compared to other regions of the world given the high latitude position and the high albedo of the ice sheet. The incoming infra-red radiation is the main power supply. The mean 1979-2005 summer (from 1st May to 30th September) values of heat fluxes averaged over the total ice sheet are: LWD = 185.9 ± 4.2 W/m², SWDn = 56.3 ± 1.7 W/m², LHF = 0.6 ± 0.2 W/m², SHF = −12.7 ± 0.7 W/m².

44 Winter = from 1st October YEAR-1 to 30th April YEAR

Since 1979, the SMB has been decreasing due to increasing run-off rates explained by higher temperatures. Only LWD and SWDn changes could explain this warming as shown in Figure 7.12. No change occurs in both sensible and latent heat fluxes since 1979. The trends are respectively + 0.33 ± 0.15 W/m^2 yr^{-1} (with a significance of 99%) and + 0.11 ± 0.06 W/m^2 yr^{-1} (with a significance of 95%). The SWD interannual fluctuations are very weak during the last 27 years except negative anomalies in 1983 and 1992 due to the eruption of the El Chichòn and the Mount Pinatubo, respectively (Hanna et al., 2005). These volcanic eruptions spew large amounts of aerosols in the atmosphere, which reduced the amount of solar energy reaching the surface of the Earth. Therefore, the net solar radiation (SWDn = SWD × [1 – α]) has been increasing not because changes in the solar incoming radiation (SWD) variability but because changes (and more precisely an decrease) in the surface albedo (α) variability.

It is clear that an increasing melt reduces the surface albedo, which of course amplifies in turn the warming-related melt increase. In Section 7.2.4, we have shown that the winter accumulation variability can not explain the albedo decrease. Therefore, it seems reasonable to conclude that SWDn changes are rather driven by the melt increase and consequently, that only the positive LWD tendency leads to the overall warming of the ice sheet surface. This assumption is confirmed in Figures 7.13, 7.14 and 7.15. The net solar radiation increase is restricted to the ablation zone while the infra-red radiation has been increasing everywhere like the temperature (7.7b). The high correlation of the temperature with the infra-red radiation versus the solar radiation variability can be seen in the Figure 7.13.

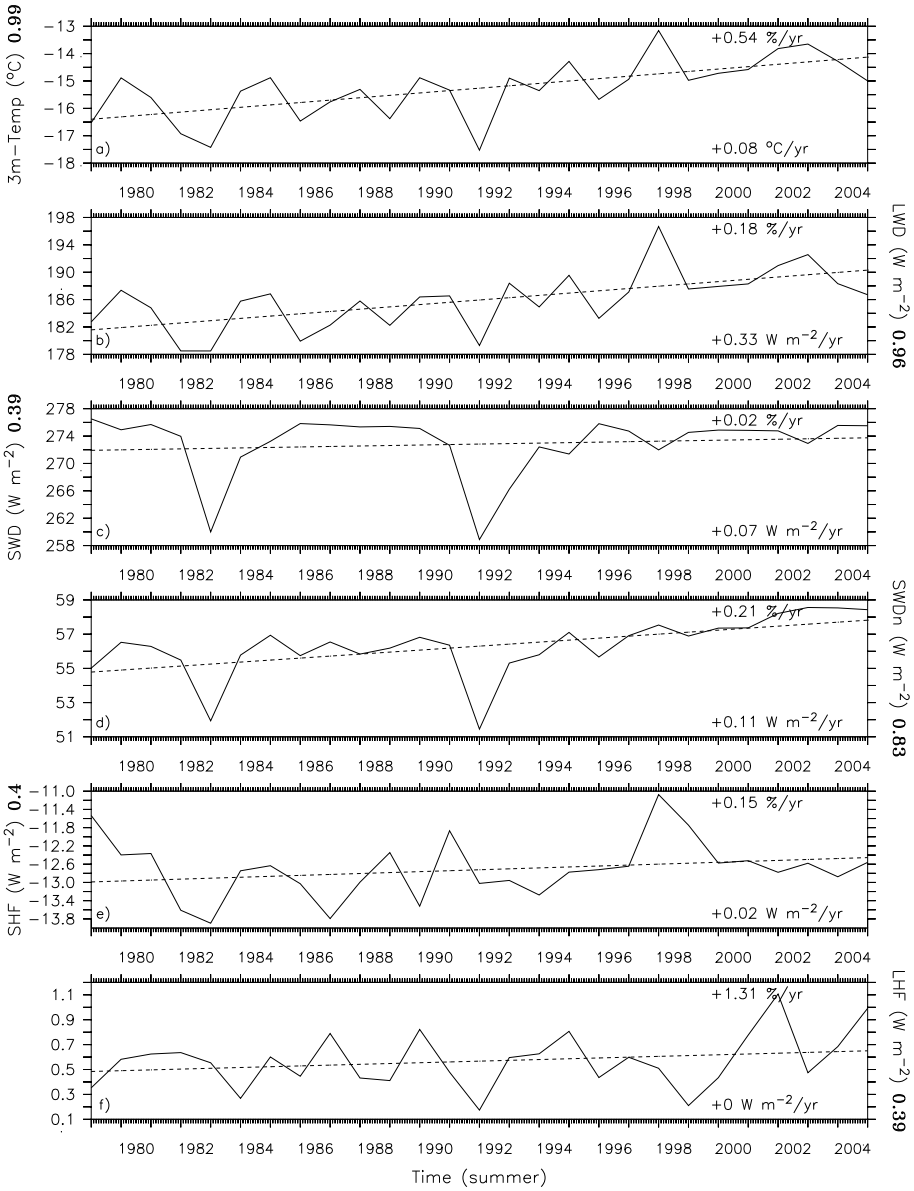

Figure 7.12 : Time series of the mean summer total ice sheet a) 3m-temperature, b) long wave downward flux, c) short wave downward flux, d) net short wave downward flux, e) sensible heat flux and f) latent heat flux. The correlation with the 3m-temperature (Figure 7.9) is indicated in bold in the titles. Units are in W/m².

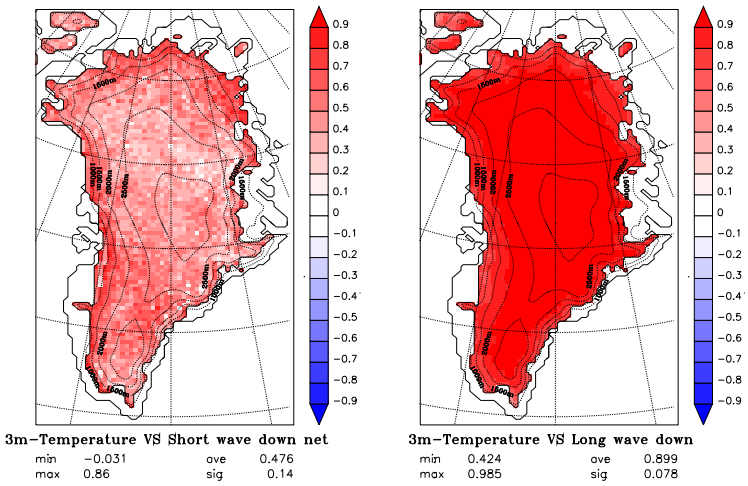

Figure 7.13 : Correlation coefficient between the 3m-temperature and the net solar radiation (left) and the infra-red radiation (right) in summer, respectively.

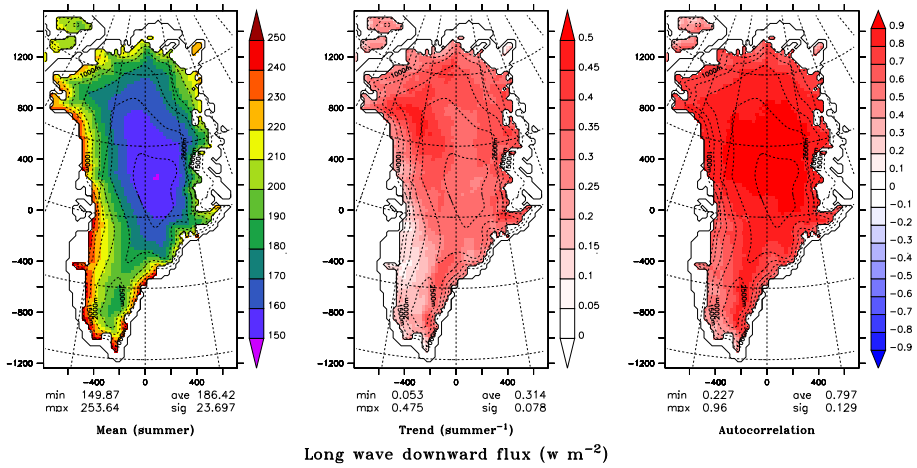

Figure 7.14 : Same as Figure 7.1, but for the summer downward infra-red flux.

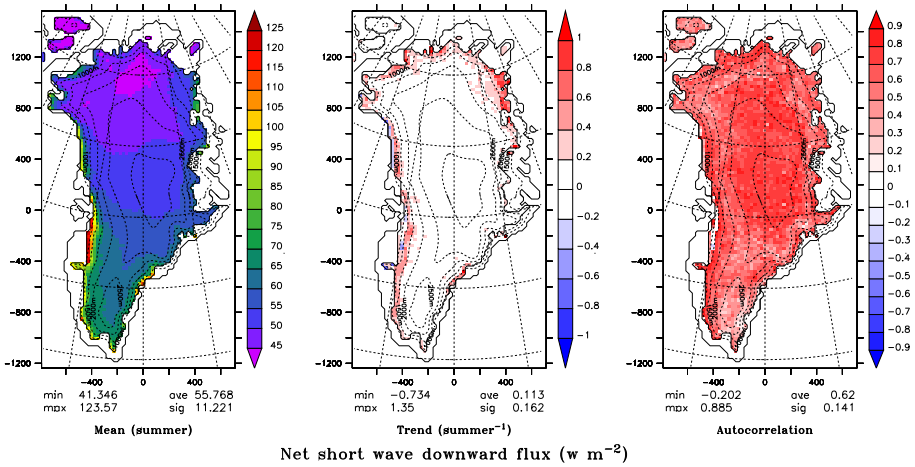

Figure 7.15 : Same as Figure 7.1, but for the summer net solar flux.

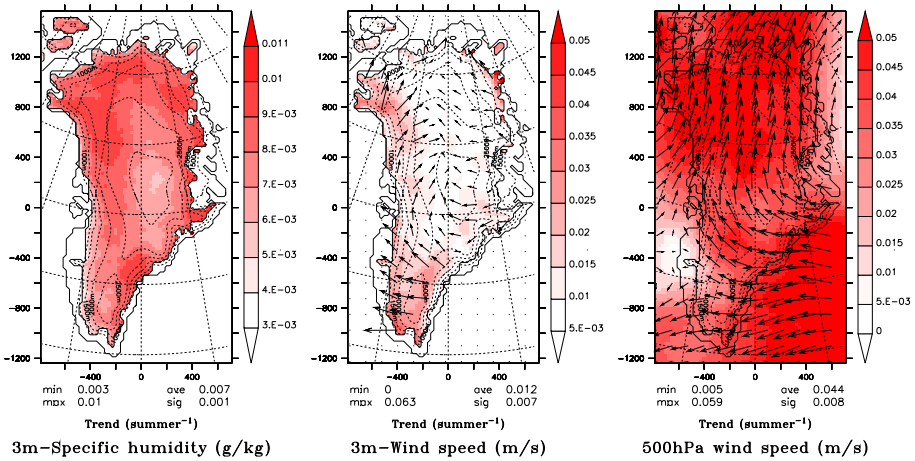

Figure 7.16 : 27-year linear regression change of the summer 3m specific humidity (left) and wind at 3m (centre) and at 500 hPa (right) .

In the south western melt area, the infra-red flux (and therefore the temperature) changes are surprisingly much weaker compared to the uniform increase everywhere else. As suggested by Figure 7.16b, this pattern could probably result from circulation changes. The strengthening of the katabatic winds simulated along the south western ice sheet slope advects cold dry air in this region which counterbalances the overall humidity content increase.

Given that water vapour is the main atmospheric greenhouse gas (GHG), this reduces the incoming infra-red radiation. Other regions rather show a tendency to a katabatic wind weakening. These trends are in agreement with changes occurring in the free atmosphere. Figure 7.16c shows indeed an intensification of the easterly winds in the south of Greenland at 500 hPa and of the southerly winds in the north of the Greenland.

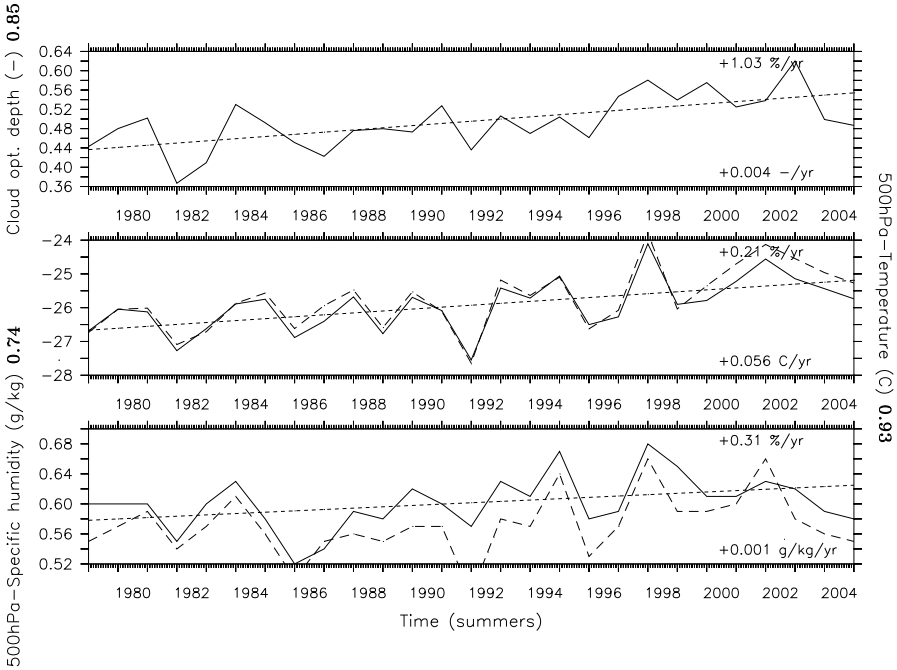

Figure 7.17 : Time series of the mean summer total ice sheet a) cloud optical depth b) temperature and c) specific humidity simulated by MAR (solid) and from ECMWF (re)analysis (dashed). The correlation with the infra-red radiation (Figure 7.13a) is indicated in bold in the titles.

We can see from Figure 7.17 changes in the cloud properties and a warming at 500 hPa in both MAR and ECMWF (re)analysis fields which favours increasing incoming infra-red radiation. Nevertheless, this warming is uniform (not shown here) suggesting that it results from an exterior factor. Indeed, the warmer the free atmosphere, the higher the water content

capacity, the higher the precipitation and the higher the downward infra-red emission. This is totally coherent with the simulated increasing solid precipitation and temperature. These results will be discussed further in the conclusion.

7.4 The North Atlantic Oscillation

The North Atlantic Oscillation (NAO) represents the dominant mode of regional atmospheric variability around Greenland (e.g. Rogers, 1997; Appenzeller et al., 1998; Bromwhich et al., 1999) and is gauged here by the NAO index, which is computed as the normalised pressure difference between Gibraltar minus Reykjavik (Jones et al., 1997; Osborn, 2004). It is closely related to the Arctic Oscillation (AO) (Thompson and Wallace, 1998).

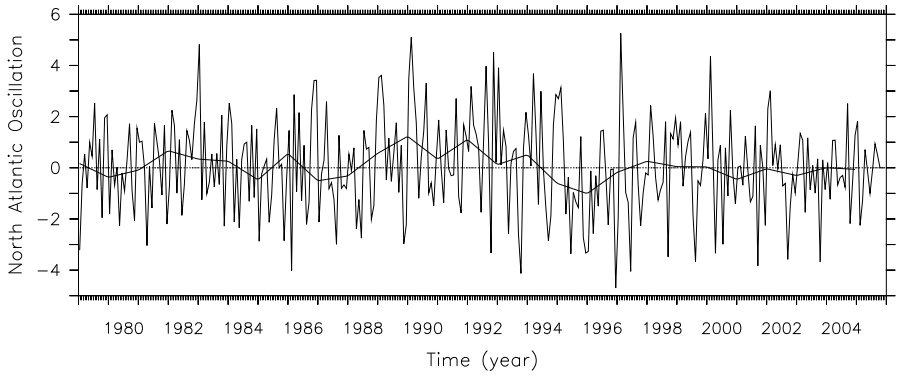

Figure 7.18 : North Atlantic Oscillation index from the Climate Research Unit (CRU) (see http://www.cru.uea.ac.uk/cru/data/nao.htm).

The NAO is characterized by a dipole of surface pressure between mid- and high-latitudes, resulting in changes in the strength of the westerly winds in mid-latitudes and large winter temperature variations. It is one of the major modes of variability of the Northern Hemisphere atmosphere. The

NAO is particularly important in winter when it exhibits its strongest interdecadal variability. A positive NAO phase shows a stronger than usual subtropical high pressure centre and a deeper than normal Icelandic low. The increased pressure difference results in more and stronger winter storms crossing the Atlantic Ocean on a more northerly track. This results in warm and wet winters in Europe and in cold and dry winters in northern Canada and Greenland. Finally, a large fraction of the climate changes observed during the last decades in the Arctic could be related to the positive trend in the NAO/AO index during this period (e.g., Rigor et al., 2002; Moritz et al., 2003; Hanna and Cappelen, 2003; Rogers et al., 2004; Johannessen et al., 2005).

Correlation coefficient with NAO	***Winter (DJF)***	***Spring (MAM)***	***Summer (JJA)***	***Autumn (SON)***	***Year***
Precipitation	-0.41 (96%)	-0.35 (91%)	0.2 (66%)	0.32 (88%)	0.0 (1%)
3m-Temperature	-0.79 (99%)	-0.45 (97%)	-0.2 (67%)	-0.56 (99%)	-0.64 (99%)
infra-red radiation	-0.75	-0.48	-0.14	-0.47	-0.58
Cloud optical depth	-0.59	-0.47	-0.11	-0.38	-0.37

Table 7.2 Mean Greenland ice sheet sensitivity to the NAO for the 1979-2005 period. The significance is added in brackets.

According to recent observations from Johannessen et al. (2005), the maximum of the Greenland ice sheet sensitivity to the NAO variability is found in winter (DJF) (Table 7.2). The temperature (via the IR radiations) are the most sensitive component and are significantly anti-correlated to the NAO as already pointed out by Chylek et al. (2004). During negative NAO, the location of the Icelandic low favours (southerly) warm air advection along the south west coast and over the ice sheet. This configuration is illustrated in Figure 7.19, which shows the mean sea level pressure for the

winters (DJF) 1995 and 1996 characterised respectively by a positive and a negative NAO index phase. This explains why the temperature correlation with the NAO is maximum in the south(west) of Greenland (Figure 7.20). Everywhere and during every season, the temperature is anti-correlated to the NAO although this correlation is not significant in summer (JJA), in particular along the northeastern coast as found by Chylek and Lohmann (2005).

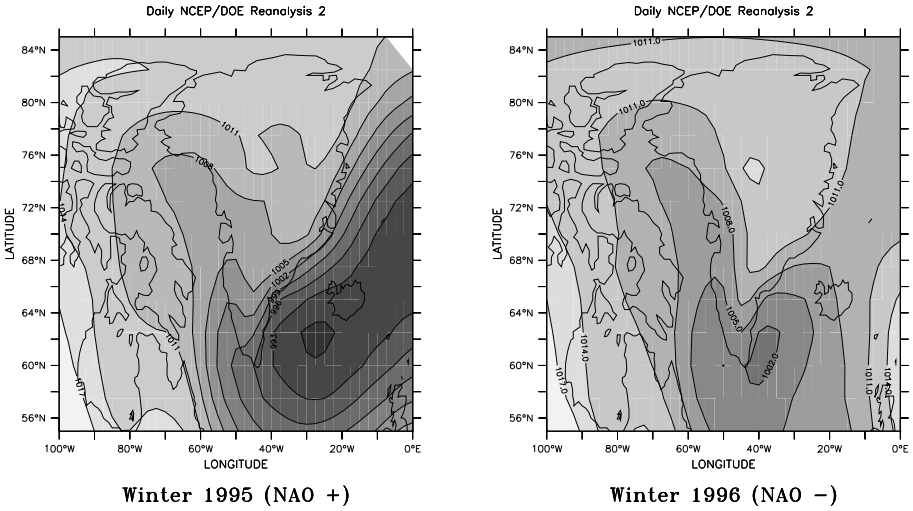

Figure 7.19 : Mean sea level pressure for the winters 1995 and 1996 from NCEP-DOE Reanalysis 2 (Kanamitsu et., 2002).

Modelled precipitation variability also contains significant links with the NAO (Figure 7.21). Consistent with the regional temperature sensitivity, a positive NAO phase (i.e. cold winter) is associated with less precipitation in the south east in winter (DJF) and autumn (SON). Generally, when the NAO is positive, stronger westerlies reduce the south westerly flow that brings moisture to Greenland resulting in an overall average reduction of the accumulation. Conversely, when the NAO is negative, the large-scale atmospheric flow is more frequently from the south west bringing more

moisture to the ice sheet, particularly in the southern region (Mosley-Thompson et al., 2005). Except in summer (JJA), heavier precipitation is well simulated along the ice sheet eastern slope and less precipitation along the western slope during high NAO phases. This pattern has been also identified by Appenzeller et al. (1998). Significant positive correlations with the NAO are obvious in summer (JJA) in the northwest and the east.

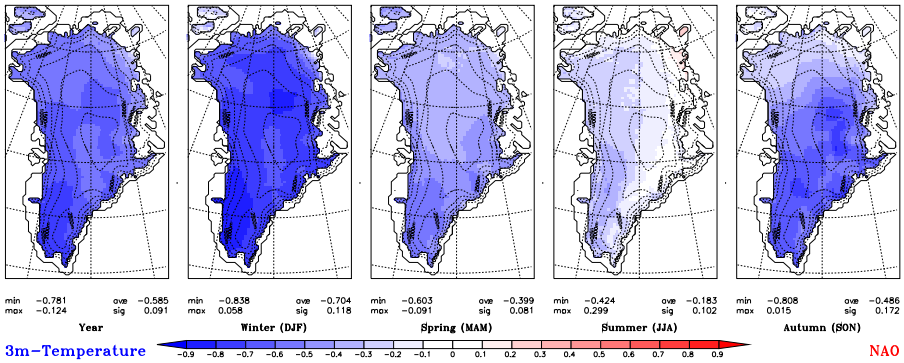

Figure 7.20 : Greenland ice sheet seasonal temperature sensitivity to the NAO. Only correlation coefficients above 0.3 are significant. The maps going from left to right are respectively the annual, winter (DJF), spring (MAM), summer (JJA) and autumn (SON) mean.

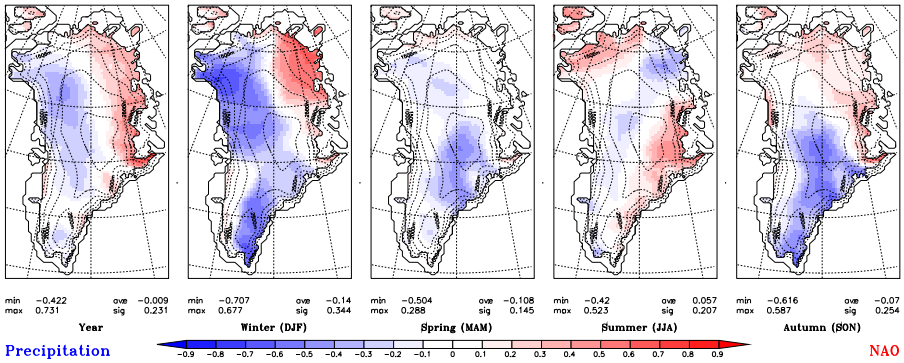

Figure 7.21 : Same as Figure 7.22 but for precipitation (solid and liquid).

The temperature is anti-correlated with the NAO index everywhere and in each season, and up to half of the temperature variability is explained by the

NAO in winter (DJF). In summer (JJA), the sensitivity to the NAO is nonetheless not significant. Some NAO links with precipitation can also be found but they are less homogeneous in time and space. In annual average and averaged over the ice sheet, the precipitation is not correlated with the NAO. Therefore the NAO is a good proxy for the Greenland winter temperature but does not explain the accumulation (winter snow fall) nor the melt (summer temperature) increases over the last 27 years. Beside, the last 40 years are characterized by large positive trends of NAO/AO indexes (Houghton et al., 2001) suggesting rather a cooling in Greenland and a warming in the Arctic region (Hanna and Cappelen, 2003; Goosse and Holland, 2005).

7.5 Discussion and conclusion

A 27-year simulation (1979-2005) of the Greenland ice sheet shows an insignificant increase in solid precipitation (+ 1.6 ± 1.8 km^3 yr^{-1} with a significance of 72%) and a significant melt water production positive perturbation (+ 4.2 ± 1.9 km^3 yr^{-1} with a significance of 98%). The increasing snowfall offsets the runoff increase to give a nearly statistically significant SMB mass loss rate of – 2.7 ± 3.0 km^3 yr^{-1} (with a significance of 87%). The contribution of changes in the net water vapour fluxes to the SMB variability is negligible. However, the 78% increase in the melt water run-off over this period suggests that the overall ice sheet mass balance has been increasingly negative, given the observed melt water-induced flow acceleration according to Zwally et al. (2002) and Rignot and Kanagaratnam (2006). As a result, it seems that increased melting dominates over increased accumulation in a warming scenario and that the Greenland ice sheet will continue to lose mass.

The melt water supply has increased because the Greenland ice sheet surface has been warming up by + 0.09 ± 0.04 °C yr^{-1} since 1979. More than 95% variance in the modelled surface mass balance totals is explained by the summer (from 1st May to 30th September) temperature and the annual precipitation variability. Part of the increasing liquid water supply comes from heavier rainfall. Due to higher temperatures, the fraction of total precipitation that is liquid has been increasing. Snowfall shows negative trends in the western ablation zone where the amount of liquid precipitation has been increasing.

The temperature has increased because of higher net solar and infra-red radiations. No significant changes in the latent and sensible heat fluxes occur. The solar power supply does not show variations during these 27 years except negative anomalies in 1983 and 1992 due to volcanic eruptions (from El Chichòn and the Mount Pinatubo). The net solar flux has increased because the albedo has been decreasing. Lower accumulation rates in winter could explain this. Indeed, low snow pack depth at the end of the winter leads to more rapid losses of winter snow mass and to higher degree day factors for bare ice (with a lower albedo) in the ablation zone. But here, the winter snowfall has been increasing. Therefore, it is rather a result of the increasing melt which humidifies the snow and decreases the albedo. Besides, the net solar flux has increased only in the zone where melting has increased while the warming is occurring throughout the ice sheet. It is clear however that the decreasing albedo amplifies in turn the warming-related melt increase by the well known albedo-temperature positive feedback. Consequently, the Greenland ice sheet warming is mainly explained by higher incoming IR fluxes. The warming is uniform over the ice sheet as the IR radiations increase, suggesting that it comes from an exterior factor. Changes in cloud properties and higher winter snowfall are likely

consequences of this warming. Indeed, the warmer the free atmosphere, the higher the water content capacity, the higher the precipitation and the higher the downward IR emission.

In conclusion, the melt has significantly increased because the Greenland ice sheet has been uniformly warming up at the surface in the last decades due to higher downward IR fluxes. These changes are significant and not explained by the natural variability (e.g. the North Atlantic Oscillation). Therefore, the changes come necessarily from an exterior factor which is obviously the greenhouse gases concentration increase due to the human activities since the beginning of the industrial era and its related recent global warming (Houghton et al., 2001). Higher GHG concentrations increase the incoming IR fluxes and warm up the free atmosphere. Although the MAR radiative scheme includes the interannual fluctuations of gases/aerosols concentrations, the major temporal variability comes from the boundaries via the ECMWF (re)analysis (Figure 7.17b) which take into account the recent GHG concentration increase and the resulting global warming. The correlation between the MAR 3m-temperature averaged on the Greenland ice sheet and the global average temperature from the CRU[45] data set is 0.7.

Since 1979, MAR simulates an increase of 78% of the freshwater flux into the ocean due to the melt of the snow/ice. For example, in the melt record year of 2003, the fresh melt water flux from Greenland into the Atlantic ocean is simulated to be 403 $km^3\ yr^{-1}$ = 1.28 10^{-2} Sv which induces a global sea level rise of 1.1 mm yr^{-1}. Figure 7.22 shows the freshwater fluxes for 2003 into the ocean obtained by a simple routing scheme based on the topography. To this flux, we must add the glacier discharge and the basal melting flux which is normally estimated to be equal to the melt water flux.

45 This data set is available at http://www.cru.uea.ac.uk/cru/data/temperature/

Increases in melt water suggest further an increase in glacier discharge owing to the observed melt water-induced ice sheet flow acceleration (Zwally et al., 2002). Once the ice starts to melt at the surface, it forms lakes that empty down into crevasses to the bottom of the ice. The meltwater lubricates then the motion of the glaciers. A long time is needed to build an ice sheet because it is limited by snowfall. But these considerations suggests that it could be rapid to reduce considerably the Greenland ice sheet (Rignot and Kanagaratnam, 2006). This is important for the understanding of the effect of Greenland melting on the stability of the thermohaline circulation and the global sea level rise.

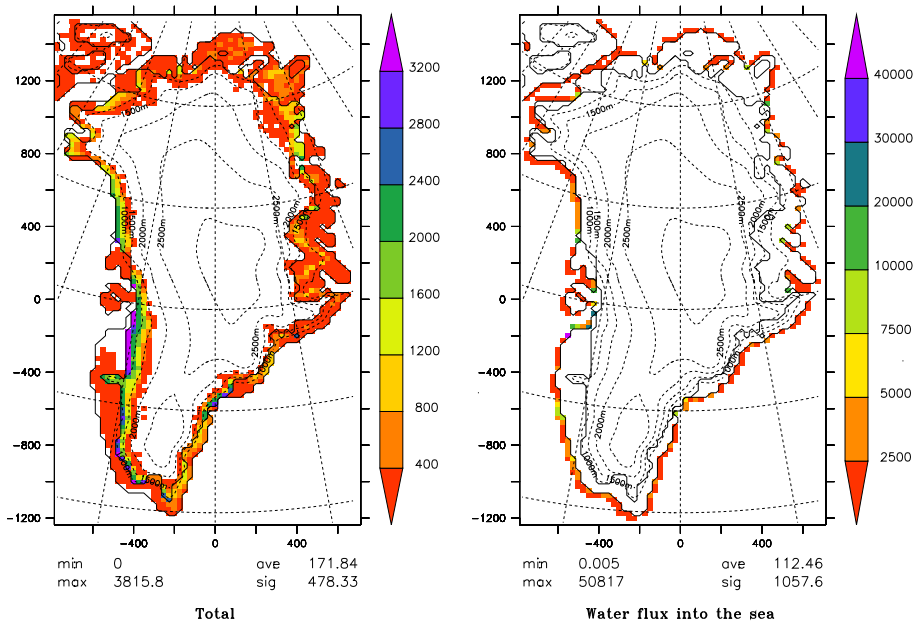

Figure 7.22 : Total run-off of 2003 (left) and freshwater fluxes into the ocean (right). The freshwater fluxes have been obtained by a simple routing scheme based on the topography. Units are in mm/yr.

This study has highlighted biases (overestimation of the deposition, melt water retention and snowfall) in the MAR estimates of the SMB

components. These biases are nonetheless systematic and are repeated each year. Therefore, it is reasonable to assume that they affect only weakly the time variability of the components simulation and that the MAR results can be reliably used to study the SMB components evolution of these last 27 years. However, the accuracy of our model needs to be improved in the future to produce more reliable assessments of surface mass budget terms and their temporal changes.

Chapter 8

Conclusions and Perspectives

8.1 Conclusion

In order to better know and assess the current state and variability of the Greenland ice sheet SMB to improve afterwards predictions of its future behaviour in the climate change context, a 27-year simulation (1979-2005) has been performed with the coupled atmosphere-snow regional model MAR. This simulation reveals an increase[46] of the main factors of the SMB which are, on the one hand, the snowfall (+ 1.6 ± 1.8 km^3 yr^{-1}) and on the other hand, the run-off (+ 4.2 ± 1.9 km^3 yr^{-1}). The net effect of these two competing factors leads to a SMB mass loss rate of – 2.7 ± 3.0 km^3 yr^{-1}, which has a significance of 87%. The 78% increase in the melt water run-off over this period suggests that the overall ice sheet mass balance has been increasingly negative, given the observed melt water-induced flow acceleration according to Rignot and Kanagaratnam (2006). As a result, it seems that increased melting dominates over increased accumulation in a warming scenario and that the Greenland ice sheet will continue to lose mass in the future.

However, a serious validation of the MAR model over the Greenland ice sheet was needed to prove the reliability of these modelled results. That is

46 The error bar in the trend is the division of the standard deviation of the MAR field temporal series by the number of years (i.e. 27). The significance has been tested using a Monte-Carlo method.

why a large part of this thesis has been devoted to the evaluation of MAR with in situ measurements as well as with remote sensing observations.

1) A first evaluation compares the 3m-temperature, humidity, wind, surface pressure, snow height and surface radiation simulated by MAR with measurements from 13 GC-Net Automatic Weather Stations (AWS) in 1998 (similar comparison with an earlier version of MAR has been published in Lefebre et al. (2005)). While the model has been found to skilfully represent the evolution of the observed Surface Boundary Layer (SBL) for all seasons and weather stations, this comparison reveals some biases in the MAR model. On average over the 13 AWSs chosen for the assessment, MAR is too cold and overestimates the solar radiation. This has also been found by Lefebre (2002) and Lefebre et al. (2005) for previous MAR versions. The cold bias implies a reduced capacity of the atmosphere to hold water vapour and leads to a negative bias in the modelled specific humidity. Similarly, colder near-surface air temperatures in the model enhance the drainage flow along the ice sheet slope (i.e. overestimate the katabatic wind). According to Morcrette (2002), Lefebre et al. (2005) and validation of MAR simulations over the Antarctic plateau by Hubert Gallée (personal communication), this cold bias is likely due to an underestimated incoming long wave flux in the radiative scheme used. In summer, this bias is considerably reduced by an overestimation of the downward solar radiation. This overestimation of the solar flux suggests also an underestimation in the simulated cloud cover which explains in turn the underestimated downward infra-red flux. The errors compensation allows MAR to simulate correctly the melt in summer. Therefore, it is reasonable to suppose that the cold bias weakly affects the simulated SMB except by favouring heavier snowfall in winter.

2) Secondly, a comparison of the MAR precipitation with measurements, results from other models and reanalyses on Greenland shows the ability of

MAR to simulate the main positive component of the SMB equation. The overestimation of precipitation found by Fettweis et al. (2005) in MAR above the ice sheet has now been corrected to a large extent. It was due to a problem of water conservation in the previous MAR hydrological scheme. Finally, the good agreement between MAR simulations at spatial resolutions of 25 km, 37.5 km, and 8.3 km via a Rain Disaggregation Model (RDM) shows the coherence in the simulation of the precipitation by the MAR model.

3) Furthermore, a comparison with the satellite AVHRR albedo enabled us to successfully validate over the whole ice sheet the modelled surface albedo but also the snow pack evolution and the snow accumulation simulated by MAR. Indeed, the surface albedo is an excellent indicator of the snow pack properties given that it depends on the nature of the snow, its grain size, its water content and its thickness. In addition, if the simulated snow pack depth is too high at the beginning of summer, this delays the appearance of low albedo zones, such as grass in the tundra or bare ice in the ablation zone, which will have an impact on the SMB. The MAR snow pack evolution agrees relatively well with the AVHRR data but the cloud detection, the corrections, the interpolation of the AVHRR data and the problems of inaccuracy in the remote sensing data when the Sun is low in the sky remain unfortunately a large source of uncertainty in this comparison. This evaluation has been published in Fettweis et al. (2005).

4) As a final validation, we have evaluated the melt area simulated by MAR by comparing it with the melt extent derived from the SMMR and SMM/I microwave brightness temperatures. A first comparison with the MAR fields and measurements from ETH-Camp and JAR-1 AWS has nonetheless highlighted flaws in the cross-polarized gradient ratio (XPGR) technique used to identify melt from the passive microwave satellite data. It

was found that dense clouds (causing notably rainfall) on the ice sheet severely perturb the XPGR melt signal. Consequently, we adapted the original XPGR melt detection algorithm to better incorporate the atmospheric variability over the ice sheet and the agreement with the model has become clearly better. The improved XPGR method shows a significant cumulated melt area increase of 1.7 % yr^{-1} (0.39×10^6 km^2 yr^{-1}) for the period 1979-2004. The simulated extent and the time evolution of the wet snow zone are successfully compared with the improved SMMR-SSM/I-derived data and an equivalent melt increase trend is also simulated by MAR. We also found a robust correlation between the total ice sheet run-off simulated by MAR and the melt extent surface detected by satellites. We published this work in Fettweis et al. (2005, 2006).

5) The last chapter has been dedicated to the analysis of the 27-year simulation (1979-2005) of the Greenland ice sheet. As mentioned above, this simulation shows a SMB mass loss rate increased by 2.7 km^3 yr^{-1} due to an increasing melt which dominates the increasing snow accumulation. This corresponds to 0.7 10^{-2} mm yr^{-1} in mean sea level rise. The contribution of changes in the net water vapour fluxes to the SMB variability is negligible. The melt water supply has increased because the Greenland ice sheet surface has been warming up by + 0.09 ± 0.04 °C yr^{-1} since 1979. Besides, the summer (from 1st May to 30th September) temperature and the annual precipitation variability explain more than 95% of the modelled surface mass balance variance. The temperature has increased owing to higher net solar and infra-red (IR) radiations. No significant changes in the latent and sensible heat fluxes occur. The solar power supply does not show significant variations during these 27 years but the net solar flux has increased due to a decrease of the surface albedo. Lower accumulation rates in winter could explain this. Indeed, low snow pack depth at the end of the winter leads to

more rapid losses of winter snow mass and to higher degree day factors (i.e. higher solar radiation absorbed by the surface) for bare ice (with a lower albedo) in the ablation zone. But, the winter snowfall has been increasing. Therefore, the albedo decrease is rather a result of the increasing melt which humidifies the snow and thereby decreases the albedo. It is however clear that the decreasing albedo amplifies the warming-related melt increase by the well known positive albedo-temperature feedback. Given that the natural climate variability (e.g. the North Atlantic Oscillation) does not explain the uniform warming on the ice sheet due to increased IR radiation, we can assume that the changes come from an exterior factor which is obviously the greenhouse gases concentration increase and its related recent global warming (Houghton et al., 2001). Therefore, the human activities are very likely the main responsible for the significant increasing melt of the Greenland ice sheet observed the last couple of years.

From 1979 to 2005, MAR simulates an increase of 78% of the fresh melt water flux into the ocean. To this flux, we must add the glacier discharge and the basal melting flux which is normally estimated to be equal to the melt water flux. However increases of melt water production suggest also a probable increase in the glacier discharge due to the observed melt water-induced ice sheet flow acceleration (Zwally et al., 2002; Rignot and Kanagaratnam, 2006). The ice sheet growth has taken a long time because it is limited by snowfall. But these considerations suggests us that a considerable reduction in the Greenland ice sheet volume could occur in the future.

To conclude, this thesis shows that the Greenland ice sheet has been significantly losing mass since the beginning of eighties, by an increasing melt water run-off as well as by a probable increasing iceberg discharge into the ocean due to the "Zwally effect" (Zwally et al., 2002). These changes

result very likely from the global warming induced by human activities. This suggests also clearly that the Greenland ice sheet will continue to lose mass in the future. The Greenland ice sheet melting will have an effect on the stability of the thermohaline circulation (THC) and the global sea level rise. On the one hand, increases in the freshwater flux from the Greenland ice sheet (glacier discharge and run-off) could perturb the THC by reducing the density contrast driving it (Driesschaert, 2005). On the other hand, the melting of the whole Greenland ice sheet would account for a global mean sea level rise of 7.4 m.

8.2 Perspectives

Although the comparison of MAR results with in situ and remote observations shows good agreement, this study has highlighted several biases in MAR among which we can mention: the cold bias in winter, the overestimation of solar radiation in summer, the overestimation of the water vapour deposition and the melt water retention in the estimates of the SMB. These biases are systematic and thus repeated each year. Therefore it is reasonable to assume that they affect only weakly the temporal variability of the simulation and that the MAR results can be reliably used to study the SMB temporal evolution. However, the accuracy of our model needs to be improved in the future to produce more reliable assessments of surface mass budget terms and their temporal changes. In addition, it should be interesting to test the blowing snow module in SISVAT over the Greenland ice sheet to study the impact of the snow drift on the total surface mass balance.

We have shown that the Greenland ablation zone is not wider than 100 km and that the whole ice sheet SMB variability is dominated by the signal coming out of this region. It would therefore be advisable to resolve this zone at a finer resolution than 25 km by coupling MAR with the SISVAT

module running at a finer resolution, for instance 5 km. The MAR atmospheric fields would have to be downscaled/disaggregated first towards a finer resolution to force the SISVAT module. The SISVAT module would resolve both surface energy and mass balance equations at this finer resolution and these results would afterwards be averaged on the 25 km x 25 km grid points to force in turn the atmospheric part of the MAR model. This would represent a two-way nesting between a high resolution regional atmospheric model and a finer resolution surface-atmosphere transfer scheme[47]. This would enable us to obtain the SMB at a finer resolution without excessive additional costs of computational time.

Another important model application would be the simulation of the Greenland mass balance in future climate conditions taken from Global Climate Models (GCMs). In a first step, the MAR model would be forced by outputs for the present climate from the GCM and compared with the 27-year simulation forced by the ECMWF reanalysis to evaluate this procedure. In a second step, the MAR model would be used to produce high resolution SMB changes from a climate change scenario simulated by the GCM.

Finally, these present and future simulations could be used to force a Greenland ice sheet model at high resolution to study for example the observed melt water-induced ice sheet flow acceleration from Zwally et al. (2002) never simulated yet by a model. This kind of ice sheet models presently use low resolution climatologies or outputs from GCMs to force their models.

47 A two way nesting has already been made by Christophe Messager (LGGE, France) between MAR and a hydrological model.

References

Abdalati W., and K. Steffen (1995) Passive microwave-derived snow melt regions on the Greenland ice sheet, Geophys. Res. Lett., 22, 787-790.

Abdalati W., and K. Steffen (1997) Snowmelt on the Greenland ice sheet as derived from passive microwave satellite data, J. Clim., 10, 165-175.

Abdalati W., and K. Steffen (2001) Greenland ice sheet melt extent: 1979-1999, J. Geophys. Res., 106, 33983-3389.

Alley, R.B., Clark, P.U., Huybrechts, P. and Joughin, I. (2005) ice sheet and sea-level changes, Science 310: 456-460, 21 October 2005.

Appenzeller, C., Schwander, J., Sommer, S., Stocker, T. F. (1998) The North Atlantic Oscillation and its imprint on precipitation and ice accumulation in Greenland, Geophys. Res. Lett., Vol. 25, No. 11, 1939-1942.

Armstrong, R.L., K.W. Knowles, M.J. Brodzik and M.A. Hardman (1994) DMSP SSM/I Pathfinder daily EASE-Grid brightness temperatures, May to September 1990 & 1991. Boulder, CO: National Snow and Ice Data Center. Digital media and CD-ROM.

Armstrong, R. L., and M. J. Brodzik (1995) Earth-gridded SSM/I data set for cryospheric studies and global change monitoring, in A 1 Symposium of COSPAR Scientific Commission A, Hamburg, Germany, July 11-21, 1994. Proceeding, Satellite monitoring of the earth's surface and atmosphere, Nov. 1995, pp. 115-116.

Bales, R.C., J.R. McConnell, E. Mosley-Thompson and B. Csath (2001) Accumulation over the Greenland ice sheet from historical and recent records, J. Geophys. Res., 106 (D24), 33813-33826.

Bamber, J. L., R.L. Layberry, and S.P. Gogineni (2001) A new ice thickness and bed data set for the Greenland ice sheet: part I, Measurement, data reduction, and errors, J. Geophys. Res., 106, 33773-33780.

Bechtold, P., E. Bazile, F. Guichard, P. Mascart and E. Richard (2001) A mass flux convection scheme for regional and global models, Q. J. R. Meteorol. Soc., 127, 869-886.

Benson, C.S., 1962, Stratigraphic studies in the snow and firn of the Greenland ice sheet: CRREL Research Report 70.

Box, J. E., and K. Steffen (2001) Sublimation estimates for the Greenland ice sheet using automated weather station observations, J. Geophys. Res., 106(D24), 33965-33982.

Box, J. E. (2002) Survey of Greenland instrumental temperature records: 1873-2001, Int. J. of Climato., 22, 1829-1847.

Box, J. E., and A. Rinke (2003) Evaluation of Greenland ice sheet surface climate in the HIRHAM regional climate model, J. Clim., 16, 1302 -1319.

Box, J.E., D. H. Bromwich, L-S Bai, (2004) Greenland ice sheet surface mass balance for 1991-2000: application of Polar MM5 mesoscale model and in-situ data, J. Geophys. Res., Vol. 109, No. D16, D16105, 10.1029/2003JD004451.

Box, J.E., D.H. Bromwich, B.A. Veenhuis, L-S Bai, J.C. Stroeve, J.C. Rogers, K. Steffen, T. Haran, S-H Wang, (2006) Greenland ice sheet surface mass balance variability (1988-2004) from calibrated Polar MM5 output, J. Clim., Vol. 19, No. 12, pp. 2783–2800

Braithwaite, R. J. (1995) Positive degree-day factors for ablation on the Greenland ice sheet studied by energy balance modelling, J. Glaciol., 41(137), 153-160.

Braithwaite, R. and Z. Yu (2000) Sensitivity of mass balance of five Swiss glavier to temperature changes assessed by tuning a deree-day model, J. Glaciol., 46, 7-14.

Brasseur, O. (2001) Development and application of a physical approach to estimating wind gusts, Mon. Weather Rev. 129, 5-25.

Brasseur O., H. Gallée, J.-D. Creutin, T. Lebel, and P. Marbaix (2001) High resolution simulations of precipitation over the Alps with the perspective of coupling with a hydrological model, Advances in Global Change Research, 10 (M. Beniston, Ed.), 75-100.

Bromwich, D.H., Q.S.Chen, Y.F.Li and R.I. Cullather, 1999: Precipitation over Greenland and its relation to the North Atlantic Oscillation, J. Geophys. Res., Vol. 104, No. D18, 22103-22115.

Bromwich, D. H., Q. Chen, L. Bai, E. N. Cassano, and Y. Li (2001) modelled precipitation variability over the Greenland ice sheet, J. Geophys. Res., 106, 33891-33908.

Brun, E., P. David, M. Sudul, and G. Brunot (1992) A numerical model to simulate snowcover stratigraphy for operational avalanche forecasting, J. Glaciol., 38, 13-22.

Bugnion, V. and P.H. Stone (2002) Snowpack model estimates of the mass balance of the Greenland ice sheet and its changes over the twenty first century, Climate Dynamics, 20, 87-106.

Businger, J. (1973) Turbulent transfert in the atmospheric surface layer, workshop on micrometeorology, Amer. Meteorol. Soc., 67-100.

Cappelen, J., B. V. Jorgensen, E. V. Laursen, L. S. Stannius, and R. S. Thomsen (2000) The observed climate of Greenland, 1958-99, with climatological standard normals, 1961-1990. DMI Tech. rep. 00-18, DMI, Copenhage, Danemark, 149pp.

Cappelen, J. (2004) Yearly Mean Temperature for Selected Meteorological Stations in Denmark, the Faroe Islands and Greenland: 1873-2003, Tech. Report 04-07, Danish Meteorological Institute, 9 pp.

Cassano, J. J., J. E. Box, D. H. Bromwich., L. Li, and K. Steffen (2001) Evaluation of Polar MM5 simulations of Greenland's atmospheric circulation, J. Geophys. Res., 106, 33891-33908.

Chen, Q.-S., D. H. Bromwich, L. Bai (1997) Precipitation over Greenland retrieved by a dynamic method and its relation to cyclonic activity, J. Clim., 10, 839-870.

Chevallier, F. and P. Bauer (2003) Model rain and clouds over oceans: comparison with SSM/I observations, Mon. Wea. Rev., 131, 1240-1255.

Christensen, O. B., J. H. Christensen, B. Machenhauer, and M. Botzet (1998) Very high-resolution regional climate simulations over Scandinavia-Present Climate, J. Clim., 11, 3204-3229.

Church, J. A., J. M. Gregory, P. Huybrechts, M. Kuhn, C. Lambeck, M. T. Nhuan, D. Qin, and P. L. Woodworth (2001), Changes in sea level, in Climate Change 2001: The Scientific Basis, edited by J. T. Houghton et al., pp. 639- 694, Cambridge Univ. Press, New York.

Chylek, P., J.E. Box, and G. Lesins (2004) Global Warming and the Greenland Ice Sheet, Climatic Change, 63, 201-221.

Chylek, P., and U. Lohmann (2005) Ratio of the Greenland to global temperature change: Comparison of observations and climate modeling results, Geophys. Res. Lett., 32, L14705, doi:10.1029/2005GL023552.

Chylek, P., M. K. Dubey, and G. Lesins (2006) Greenland warming of 1920–1930 and 1995–2005, Geophys. Res. Lett., 33, L11707, doi:10.1029/2006GL026510.

Cogley, J. G., (2004) Greenland accumulation: An error model, J. Geophys. Res., 109, D18101, doi:10.1029/2003JD004449.

Colbeck, S. C. (1974) The capillary effects on water percolation in homogeneous snow, J. Glaciol., 13(67), 85-97.

Cuffey, K. M., and S. J. Marshall (2000) Substantial contribution to sea level rise during the last interglacial from the Greenland ice sheet, Nature, 404, 591-594.

Davies, H. (1983) Limitations of some common lateral boundary schemes used in regional NWP models. Mon. Wea. rev., 111, 1002-1012.

De Ridder, K. and G. Schayes (1997) The IAGL land surface model, J. Appl. Meteorol., 36, 167-182.

De Ridder, K., and H. Gallée (1998) Land surface-induced regional climate change in Southern Israel, J. Appl. Meteorol., 37, 1470-1485.

Deardorff J. W. (1978) Efficient prediction of ground surface temperature and moisture with inclusion of a layer of vegetation, J. Geophys. Res., 83, 1889-1903.

Dethloff, K., M. Schwager, J. H. Christensen, S. Kiilsholm, A. Rinke, W. Dorn, F. Jung-Rothenhäusler, H. Fischer, S. Kipfstuhl, and H. Miller (2002) Recent Greenland accumulation estimated from regional model simulations and ice core ananlysis, J. Clim., 15, 2821-2832.

Dethloff, K., W. Dorn, A. Rinke, K. Fraedrich, M. Junge, E. Roeckner, V. Gayler, U. Cubasch, and J. H. Christensen (2004) The impact of Greenland's deglaciation on the Arctic circulation, Geophys. Res. Lett., 31, L19201, doi:10.1029/2004GL020714.

Driesschaert, E. (2005) Climate change over the next millennia using LOVECLIM, a new earth system model including the polar ice sheets, Ph.D. thesis, Université catholique de Louvain.

di Sarra, A., M. Cacciani, G. Fiocco, and D. Fua (2002) Lidar observation of polar stratospheric clouds over northern Greenland in the period 1990-1997, J. Geophys. Res., 107, D12, 10.1029/2001JD001074.

Duynkerke, P. G. (1988) Application of the E-ε turbulence closure model to the neutral and stable atmospheric boundary layer, J. Atmos. Sci., 45, 865-880.

Duynkerke, P. G. (1991) Radiation fog: a comparison of model simulation with detailed observations, Mon. Wea. rev., 119, 324-341.

Duynkerke, P. G. and M. R. van den Broeke (1994) Surface energy balance and katabatic flow over glacier and tundra during GIMEX-91, Global Planet. Change, 9, 17-28.

Eppler, D., L. Farmer, A. Lohanick, M. Anderson, D. Cavalieri, J. Comiso, P. Gloersen, C. Garrity, T. Grenfell, M. Hallikainen, J. Maslanik, C. M¨atzler, R. Melloh, I. Rubinstein, and C. Swift (1992) Passive microwave signatures of sea ice, in Microwave Remote Sensing of sea ice, edited by F. Carsey, Geophysical Monograph 68, chap. 4, American Geophysical Union.

Fettweis, X., Gallée, H., Lefebre, L., van Ypersele, J.-P. (2005) Greenland surface mass balance simulated by a regional climate model and comparison with satellite derived data in 1990-1991, Climate Dynamics, Volume 24, Issue 6, May 2005, 623-640, DOI 10.1007/s00382-005-0010-y.

Fettweis, X., Gallée, H., Lefebre, L., van Ypersele, J.-P. (2006) The 1988-2003 Greenland ice sheet melt extent by passive microwave satellite data and a regional climate model, Climate Dynamics, DOI:10.1007/s00382-006-0150-8.

Fichefet, T., Poncin, C., Goosse, H., Huybrechts, P., Janssens, I., and Le Treut, H. (2003) Implications of changes in freshwater flux from the Greenland ice sheet for the climate of the 21st century, Geophys. Res. Lett., 30(17):1913.

Fouquart, Y. and. B. Bonnel (1980) Computation of the solar heating of the Earth's atmosphere: A new parameterization. Beitr. Phys. Atmos., 53, 35-62.

Fowler, C., J. Maslanik, T. Haran, T. Scambos, J. Key, and W. Emery (2000) AVHRR Polar Pathfinder Twice-Daily 5 km EASE-Grid Composites. Boulder, CO, USA: National Snow and Ice Data Center. Digital media. See also http://nsidc.org/data/docs/daac/nsidc0066_avhrr_5km.gd.html.

Funk, C., J. Michaelsen (2004) A Simplified Diagnostic Model of Orographic Rainfall for Enhancing Satellite-Based Rainfall Estimates in Data-Poor Regions, Journal of Applied Meteorology, Vol. 43, No. 10, pp. 1366-1378.

Gallée, H. and G. Schayes (1994) Development of a three-dimensional meso-γ primitive equations model, Mon. Wea. rev., 122, 671-685.

Gallée, H. (1995) Simulation of the mesocyclonic activity in the Ross Sea, Antarctica, Mon. Wea. rev., 123, 2051-2069.

Gallée, H. and P. G. Duynkerke (1997) Air-snow interaction and the surface energy and mass balance over the melting zone of West Greenland during the Greenland Ice Margin Experiment, J. Geophys. Res., 102, 13813-13824.

Gallée, H., G. Guyomarc'h and E. Brun (2001) Impact of the snow drift on the Antarctic ice sheet surface mass balance: possible sensitivity to snow-surface properties, Boundary-Layer Meteorol., 99, 1-19.

Gallée, H., W. Moufouma-Okia, P. Bechtold, O. Brasseur, I. Dupays, P. Marbaix, C. Messager, R. Ramel, and T. Lebel (2004) A high-resolution simulation of a West African rainy season using a regional climate model, J. Geophys. Res., 109, D05108, doi:10.1029/2003JD004020.

Giorgi, F., and L. O. Mearns (1999) Regional climate modeling revisited, J. Geophys. Res., 104, 6335-6352.

Goosse H and M. Holland (2005) Mechanisms of decadal Arctic variability in the Community Climate System Model CCSM2. Journal of Climate 18 (17) 3552-3570.

Greenland Ice-core Project (GRIP) Members (1993) Climate instability during the last interglacial period recorded in the GRIP ice core, Nature 364, 203-207.
Gregory, J. M., P. Huybrechts, and S. Raper (2004) Threatened loss of the Greenland ice sheet, Nature, 428, 616, doi:10.1038/428616a.
Gregory, J., Dixon, K., R.J., S., Weaver, A., Driesschaert, E., Eby, M., Fichefet, T., Hasumi, H., Hu, A., Jungclaus, J., Kamenkovich, I., Levermann, A., Montoya, M., Murakami, S., Nawrath, S., Oka, A., Solokov, A., and Thorpe, R. (2005) A model intercomparison of changes in the Atlantic thermohaline circulation in response to increasing atmospheric concentration, Geophys. Res. Lett., 32:L12703.
Greve, R (2000) On the response of the Greenland ice sheet to greenhouse climate change, Climatic Change, 46 (3), 289-303.
Greuell W, Konzelmann T (1994) Numerical modelling of the energy balance and the englacial temperature of the Greenland ice sheet. Calculations for the ETH-Camp location (West Greenland, 1155 m a.s.l.), Global Planet Change, 9:91-114.
Greuell W., B. Denby, R.S.W. van de Wal, and J. Oerlemans (2001) Ten years of massbalance measurements along a transect near Kangerlussuaq, Greenland, J. Glaciol., 47, 157-158.
Hanna, E. and P. Valdes (2001) Validation of ECMWF (re)analysis surface climate data, 1979-98, for Greenland and implications for mass balance modelling of the Ice Sheet, Int. J. of Climatology 21, 171-195.
Hanna, E., P. Huybrechts, and T. Mote (2002) Surface mass balance of the Greenland ice sheet from climate analysis data and accumulation/run-off models, Ann. Glaciol., 35, 67-72.
Hanna, E. and Cappelen, J. (2003) Recent cooling in coastal southern Greenland and relation with the North Atlantic Oscillation, Geophys. Res. Lett., 30: 1132.
Hanna, E., P. Huybrechts, I. Janssens, J. Cappelen, K. Steffen, and A. Stephens, (2005) Runoff and mass balance of the Greenland ice sheet: 1958-2003, J. Geophys. Res.,110, D13108, doi:10.1029/2004JD005641.
Houghton, J., Y. Ding, D. Griggs, M. Noguer, P. van der Linden, X. Dai, K. Maskell, and C. Johnson (2001) IPCC: Climate Change 2001: The Scientific Basis. Contribution of Workings Group I to the Third Assessment Report of the Intergovernmental Panel on Climate Change, Cambridge University Press, Cambridge, United Kingdom and New York, NY, USE, 881pp.
Howat, I. M., I. Joughin, S. Tulaczyk, and S. Gogineni (2005) Rapid retreat and acceleration of Helheim Glacier, east Greenland, Geophys. Res. Lett., 32, L22502, doi:10.1029/2005GL024737.
Huybrechts, P., I. Janssens, C. Poncin, and T. Fichefet (2002) The response of the Greenland ice sheet to climate changes in the 21st century by interactive coupling of an AOGCM with a thermomechanical ice sheet model, Ann. Glaciol., 35, 409-415.
Huybrechts, P., J. Gregory, I. Janssens, and M. Wild (2004). Modelling Antarctic and Greenland volume changes during the 20th and 21st centuries forced by GCM time slice integrations, Global and Planetary Change, 42, 83-105.
Janssens, I., and P. Huybrechts (2000) The treatment of meltwater retention in mass-balance parameterizations of the Greenland ice sheet, Ann. Glaciol., 31, 133-140.

Johannessen, O.M., Khvorostovsky, K., Miles, M.W. and Bobylev, L.P. (2005) Recent ice sheet growth in the interior of Greenland. Sciencexpress, http://www.sciencexpress.org, 20 October 2005, DOI: 10.1126/science.1115356.

Jones PD, Jonsson T and Wheeler D (1997) Extension to the North Atlantic Oscillation using early instrumental pressure observations from Gibraltar and South-West Iceland. Int. J. Climatol. 17, 1433-1450.

Joughin, I. (2006) Greenland Rumbles Louder as Glaciers Accelerate, Science 24 March 2006: 1719-1720.

Kanamitsu, M., W. Ebisuzaki, J. Woollen, S-K Yang, J.J. Hnilo, M. Fiorino, and G. L. Potter (2002). NCEP-DEO AMIP-II Reanalysis (R-2), Bul. of the Atmos. Met. Soc., 1631-1643, Nov 2002. (see also http://www.cdc.noaa.gov/cdc/data.ncep.reanalysis2.html)

Kessler, E. (1969) On the distribution and continuity of water substance in atmospheric circulation, Meteor. Monogr., 84 pp.

Key, J. (1999) The cloud and surface parameter retrieval (CASPR) system for polar AVHRR, 59 pp., Coop. Inst. For Meteorol. Satell. Stud., Univ. of Wisc., Madison.

Key, J., X. Wang, J. Stoeve and C. Fowler (2001) Estimating the cloudy-sky albedo of sea ice and snow from space, J. Geophys. Res., 106, 12489-12497.

Kiilsholm, S., Christensen, J. H., Dethloff, K., Rinke, A. (2003) Net accumulation of the Greenland ice sheet: High resolution climate modelling of regional climate change in the Arctic, Geophys. Res. Lett. 30, 1485, doi:10.1029/2002GL015742.

Krabill, W., E. Frederick, S. Manizade, C. Martin, J. Sonntag, R. Swift, R. Thomas, W. Wright and J. Yngel (1999) Rapid thinning of parts of the southern Greenland ice sheet, Science, 283, 1522-1524.

Krabill, W., Abdalati, W., Frederick, E., Manizade, S., Martin, C., Sonntag, J., Swift, R., Thomas, R., Wright, W. and J. Yungel (2000) Greenland Ice Sheet: High-Elevation Balance and Peripheral Thinning, Science, 289: 428-430.

Krabill W., E. Hanna, P. Huybrechts, W. Abdalati, J. Cappelen, B. Csatho, E. Frederick, S. Manizade, C. Martin, J. Sonntag, R. Swift, R. Thomas, and J. Yungel (2004) Greenland Ice Sheet: Increased coastal thinning. Geophys. Res. Lett., 31, L24402, doi:10.1029/2004GL021533.

Lefebre, F., Gallee, H., Ypersele, J.-P. van, Huybrechts, P. (2002) Modelling of large-scale melt parameters with a regional climate model in South-Greenland during the 1991 melt season, Ann. Glaciol., 35, 391-397.

Lefebre, F. (2002) Modelling the Greenland climate and its surface mass balance with a coupled atmosphere-snow model, Ph.D. thesis, Université catholique de Louvain.

Lefebre, F., H. Gallée, J. van Ypersele, and W. Greuell (2003) Modeling of snow and ice melt at ETH-camp (west Greenland): a study of surface albedo, J. Geophys. Res., Vol. 108 No. D8, 10.1029/2001JD001160.

Lefebre, F., X. Fettweis, H. Gallée, J. van Ypersele, P. Marbaix, W. Greuell, and P. Calanca (2005) Evaluation of a high-resolution regional climate simulation over Greenland, Climate Dynamics, Volume 25, Issue 1, Jul 2005, Page 99, DOI 10.1007/s00382-005-0005-8.

Lin, Y.-L., R. D. Farley, and H. D. Orville (1983) Bulk parameterization of the snow field in a cloud model, J. Appl. Meteorol., 22, 1065-1092.

Luckman, A., and T. Murray (2005) Seasonal variation in velocity before retreat of Jakobshavn Isbræ, Greenland, Geophys. Res. Lett., 32, L08501, doi:10.1029/2005GL022519.

Luckman, A., T. Murray, R. de Lange, and E. Hanna (2006) Rapid and synchronous ice-dynamic changes in East Greenland, Geophys. Res. Lett., 33, L03503, doi:10.1029/2005GL025428.

Manabe, S. and Stouffer, R. (1994) Multiple-century response of a coupled ocean-atmosphere model to an increase of atmospheric carbon dioxide, J. of Clim., 7:523.

Marbaix, P. (2000) A regional atmospheric model over Europe: Adaptation for climate studies and validation, Ph.D. thesis, Université catholique de Louvain.

Marbaix, P., H. Gallée, O. Brasseur, and J. van Ypersele (2003) Lateral boundary conditions in regional climate models: a detailed study of relaxation procedure, Mon. Wea. rev., 131, 461-479.

Messager C, H. Gallée and O. Brasseur (2004) Precipitation sensitivity to regional SST in a regional climate simulation during the West African monsoon for two dry years, Climate Dynamics., 22, 249-266.

Mlawer, E. J., Taubman, S. J., Brown, P. D., Iacono, M. J., Clough, S. A. (1997) Radiative transfer for inhomogeneous atmospheres: RRTM, a validated correlated-k model for the long-wave, J. Geophys. Res. Vol. 102, No. D14, p. 16,663-16,682 (97JD00237).

Morcrette, J. (1984) Sur la paramétrisation du rayonnement dans les modèles de circulation générale atmosphérique, Ph. D. Thesis, univ. des Sci. et Tech. de Lille, Lille, France.

Morcrette, J. (2002) The surface downward long-wave radiation in the ECMWF forecast system, J. of Climate, 15, 1875-1892.

Moritz, R.E., C.M. Bitz, and E.J. Steig (2003) Dynamics of recent climate change in the Arctic, Sciences, 297,1497-1502.

Mosley-Thompson, E., C. R. Readinger, P. Craigmile, L. G. Thompson, and C. A. Calder (2005) Regional sensitivity of Greenland precipitation to NAO variability, Geophys. Res. Lett., 32, L24707, doi:10.1029/2005GL024776.

Mote, T. L. (2003) Estimation of run-off rates, mass balance, and elevation changes on the Greenland ice sheet from passive microwave observations, J. Geophys. Res., 108(D2), 4056, doi :10.1029/2001JD002032.

Mote, T. L., and M. R. Anderson (1995) Variations in snowpack melt on the Greenland ice sheet based on passive microwave-measurements, J. Glaciol., 41, 51-60.

Mote, T. L., M. R. Anderson, K.C. Kuivinen, and C. M. Rowe (1993) Passive microwave-derived spatial and temporal variations of summer melt on the Greenland ice sheet, Ann. Glaciol., 17, 233-238.

Murphy, B. F., I Marsiat, and P. Valdes (2002) Atmospheric contributions to the surface mass balance model of Greenland in the HadCM3 atmospheric model, J. Geophys. Res., 107(D21), 4556, doi:10.1029/2001JD000389.

New M., M. Hulme, P. Jones (2000) Representing twentieth-century space-time climate variability. Part II: Development of 1901-96 monthly grids of terrestrial surface climate, J. of Climate, 13, 2217-2238.

Oerlemans J. and H. Vugts (1993) A meteorological experiment in the melting zone of the Greenland Ice Sheet, Bull Amer Meteor Soc 74: 355-365.

Ohmura, A., K. Steffen, H. Blatter, W. Greuell, M. Rotach, M. Stober, T. Konzelmann, J. Forrer, A. Abe-Ouchi, D. Steiger, and G. Niederbaumer (1992) Energy and mass balance during the melt season at the equilibrium line altitude, Paakitsoq, Greenland ice sheet: Progress report 2, Dep. of Geography, Swiss Federal Institute of Technology, Zurich.

Ohmura, A., P. Calanca, M. Wild, and M. Anklin, (1999) Precipitation, accumulation, and mass balance of the Greenland ice sheet, Zeit. Gletsch. Glazialgeol, 35, 1-20.

Ohmura, A. (2001) Physical Basis for the Temperature-Based Melt-Index Method, J. of Applied Meteorolgy, Vol. 40, No. 4, pp. 753-761.

Osborn TJ (2004) Simulating the winter North Atlantic Oscillation: the roles of internal variability and greenhouse gas forcing, Clim. Dyn., 22, 605-623.

Paterson, W. (1994) The physics of glaciers, 3rd ed., Pergamon/Elsevier Science Ltd.

Pfeffer, W., M. Meier, and T. Illangasekare (1991) Retention of Greenland run-off by refreezing: implication for projected future sea level change, J. Geophys. Res., 96, 22117-22124.

Rahmstorf, S. (1995) Bifurcations of the Atlantic thermohaline circulation in response to changes in the hydrological cycle, Nature, 378:145-149.

Rahmstorf, S. and Ganopolski, A. (1999) Long-term global warming scenarios computed with an ecient coupled climate model, Climatic Change, 43:353-367.

Rahmstorf, Stefan; Crucifix, Michel; Ganopolski, Andrey; Goosse, Hugues; Kamenkovich, Igor; Knutti, Reto; Lohmann, Gerrit; Marsh, Robert; Mysak, Lawrence A.; Wang, Zhaomin; Weaver, Andrew J. (2005) Thermohaline circulation hysteresis: A model intercomparison, Geophys. Res. Lett., Vol. 32, No. 23, L23605, 10.1029/2005GL023655.

Reynolds, R. W. and T. M. Smith (1994) Improved global sea surface temperature analyses using optimum interpolation, J. of Climate, 7, 929-948.

Ridley, J., Huybrechts, P., Gregory, J., and Lowe, J. (2005) Future changes in the greenland ice sheet: A 3000 year simulation with a high resolution ice sheet model interactively coupled to an AOGCM, J. of Climate, 18, 3409-3427.

Rignot., E. and R. Thomas (2002) Mass Balance of Polar Ice Sheets, Science, 297, 1502-1506.

Rignot, E., D. Braaten, S. P. Gogineni, W. B. Krabill, and J. R. McConnell (2004) Rapid ice discharge from southeast Greenland glaciers, Geophys. Res. Lett., 31, L10401, doi:10.1029/2004GL019474.

Rignot, E. and P. Kanagaratnam (2006) Changes in the Velocity Structure of the Greenland Ice Sheet, Science 17 February 2006, 311: 986-990 [DOI: 10.1126/science.112138].

Rigor, I.G., J. M. Wallace, and R. L. Colony (2000) Response of sea ice to the Arctic Oscillation, J. of Climate, 15, 2648-2663.

Ritz, C., Fabre, A. and A. Letréguilly (1997) Sensitivity of a Greenland ice sheet model to ice flow and ablation parameters: Consequences on the evolution through the last climatic cycle, Climate Dynamics, 13, 11-24.

Rogers, .J C. (1997) North Atlantic storm track variability and its association to the North Atlantic Oscillation and climate variability of Northern Europe, J. of Climate, 10(7), 1635-1647.

Rogers, J.C., S.H. Wang, D. H. Bromwicg (2004) On the role of the NAO in recent northeastern Atlantic Artic warming, Geophys. Res. Lett., 31, L02201, doi:10,1029/2003GL018728.

Schiermeier Q. (2004) Greenland's climate: A rising tide. Nature, 428, 114-115, doi:10.1038/428114a.

Segal, M., J. R. Garratt., R. A. Pielke and Z. Ye (1991) Scaling and Numerical Model Evaluation of Snow-Cover Effects on the Generation and Modification of Daytime Mesoscale Circulations, J. of the Atmos. Sci., 48: 1024-1042.

Simmons, A. J., and J. K. Gibson (2000) The ERA-40 project plan, ERA-40 Proj. Rep. 1, Eur. Cent. for Med.-Range Weather Forecasts, Reading, U. K.

Sinclair, M. R. (1994) A diagnostic model for estimating orographic precipitation, J. Appl. Meteorol., 33, 1163-1175.

Steffen, K., and J. E. Box (2001) Surface climatology of the Greenland ice sheet: Greenland Climate Network 1995-1999, J. Geophys. Res., 106(D24), 33951-33964.

Steffen, K. (2002) Greenland maximum melt extent available on http://cires.colorado.edu/steffen/melt/.

Steffen, K., S. V. Nghiem, R. Huff, and G. Neumann (2004) The melt anomaly of 2002 on the Greenland Ice Sheet from active and passive microwave satellite observations, Geophys. Res. Lett., 31, L20402, doi:10.1029/2004GL020444.

Steffen, K. (2005) Greenland Melt Extent, 2005 available on http://cires.colorado.edu/science/groups/steffen/greenland/melt2005/

Stroeve, J. (2001) Assessment of Greenland albedo variability from advanced very high resolution radiometer Polar Pathfinder data set, J. Geophys. Res., 106, 33989-34006.

Stroeve, J., J. Box, C. Fowler, T. Haran, and J. Key (2000) Intercomparison between in situ and AVHRR Polar Pathfinder-derived surface albedo over Greenland, Remote Sens. Environ., 75, 360-374.

Stroeve, J., A. Nolin, and K. Steffen (1997) Comparison of AVHRR-derived and in situ surface albedo over Greenland ice sheet. Remote Sens. Environ., 62, 262-276.

Swingedouw, D., P. Braconnot, and O. Marti (2006) Sensitivity of the Atlantic Meridional Overturning Circulation to the melting from northern glaciers in climate change experiments, Geophys. Res. Lett., 33, L07711, doi:10.1029/2006GL025765.

Thomas, R., Csatho, B., Davis, C., Kim, C., Krabill, W., Manizade, S., McConnell, J., Sonntag, J. (2001) Mass balance of higher-elevation parts of the Greenland ice sheet, J. Geophys. Res. Vol. 106, No. D24, p. 33707 (2001JD900033).

Thomas, R. H., and PARCA Investigators (2001) PARCA 2001, Program for Arctic Regional Climate Assessment (PARCA): Goals, key findings, and future directions, J. Geophys. Res., 106 (D24), 33691-33706.

Thompson, D. W. J. and Wallace, J. M. (1998) The Arctic Oscillation signature in the wintertime geopotential height and temperature fields, Geophys. Res. Lett. Vol. 25, No. 9, 1297-1300.

Toniazzo, T., Gregory, J. M. and P. Huybrechts (2004) Climatic Impact of a Greenland Deglaciation and Its Possible Irreversibility, J. of Clim., 17: 21-33.
Torinesi, O., M. Fily and C. Genthon (2003) Variability and trends of the summer melt period of Antarctic ice margin since 1980 from microwave sensors, J. Climate, 16, 1047-1060.
Ulaby, F. and W. Stiles (1980) The active and passive microwave response to snow parameters. 2: water equivalent of dry snow, J. Geophys. Res., 85: 1045-1049.
van den Broeke, M.R., P.G. Duynkerke and J. Oerlemans (1994) The observed katabatic flow at the edge of Greenland ice sheet during GIMEX-91, Global Planet. Change, 9, 3-15.
van den Broeke, M.R. and H. Gallée (1996) Observation and simulation of barrier winds at the western margin of the Greenland ice sheet, Q. J.R. Meteorol. Soc., 122, 1365-1383.
van der Veen, C. J. (2002) Polar ice sheets and global sea level: how well can we predict the future?, Glob. Plan. Chng., 32, 165-194.
van de Wal, R.S.W. and J. Oerlemans (1994) An energy balance model for the Greenland ice sheet, Global Planet, Change, 9, 115-131.
van de Wal, R. S. W., M. Wild, and J. R. de Wolde (2001) Short-term volume changes of the Greenland ice sheet in response to doubled CO2 conditions, Tellus, Ser. B, 53, 94-102.
Velicogna, I., and J. Wahr (2005) Greenland mass balance from GRACE, Geophys. Res. Lett., 32, L18505, doi:10.1029/2005GL023955.
Voss, R. and Mikolajewicz, U. (2001) Long-term climate changes due to increased CO_2 concentration in the coupled atmosphere-ocean general circulation model Echam3/LSG, Climate Dynamics, 17, 4560.
Wendler, G.,N. Ishikawa and Y. Kodama (1988) The Heat Balance of the Icy Slope of Adelie Land, Eastern Antarctica, J. of Applied Meteorology, 27: 52-65.
Wild, M., P. Calanca, S. C. Scherrer, and A. Ohmura (2003) Effects of polar ice sheets on global sea level in high-resolution greenhouse scenarios, J. Geophys. Res., 108(D5), 4165, doi:10.1029/2002JD002451.
Wiscombe, W. J. and S. G. Warren (1980) A Model for the spectral albedo of snow. I: Pure snow, J. Atm. Sc., 37(12), 2712-2733.
Xie, P. and P. Arkin (1997) Global precipitation: a 17-year monthly analysis based on gauge observations, satellite estimates and numerical model outputs, BAMS, 78, 2539-2558.
Xue, Y., S. Sun, D. S. Kahan, and Y. Jiao (2003) Impact of parameterizations in snow physics and interface processes on the simulation of snow cover and run-off at several cold region sites, J. Geophys. Res., 108(D22), 8859, doi:10.1029/2002JD003174.
Zuo, Z., and J. Oerlemans (1996) Modelling albedo and specific balance of the Greenland ice sheet: calculations for the Sondre Stromfjord transect, J. Glaciol., 42(141), 305-317.
Zwally, J. H. and M. B. Giovinetto (2001) Balance mass flux and ice velocity across the equilibrium line in drainage systems of Greenland, J. Geophys. Res., 106, 33717-33728.

Zwally, J.H., W. Abdalati, T. Herring, K. Larson, J. Saba, and K. Steffen (2002) Surface Melt-Induced Acceleration of Greenland ice sheet Flow. Science 12 July 2002; 297: 218-222; published online 6 June 2002 [DOI: 10.1126/science.1072708].

Zwally, H. Jay; Giovinetto, Mario B.; Li, Jun; Cornejo, Helen G.; Beckley, Matthew A.; Brenner, Anita C.; Saba, Jack L.; Yi, Donghui (2005) Mass changes of the Greenland and Antarctic ice sheets and shelves and contributions to sea-level rise: 1992-2002, J. Glaciol., Volume 51, Number 175, December 2005, pp. 509-527(19).

Zweck, C., and P. Huybrechts (2005) Northern hemisphere ice sheet modeling of the last glacial cycle and glaciological sensitivity, J. Geophys. Res., 110, D07103, doi:10.1029/2004JD005489.